

**The interplay of faulting, magmatism and
hydrothermal fluid flow at oceanic ridges
– new insights from numerical modeling**

Dissertation zur Erlangung des Doktorgrades
der Mathematisch-Naturwissenschaftlichen Fakultät
der Christian-Albrechts-Universität zu Kiel

vorgelegt von

Christine Andersen

Kiel, 2015

Hiermit versichere ich, dass ich die vorliegende Doktorarbeit selbstständig verfasst habe und keine anderen als die angegebenen Quellen und Hilfsmittel benutzt habe. Ferner habe ich diese Arbeit weder ganz noch in Teilen an anderer Stelle im Rahmen eines Prüfungsverfahrens vorgelegt, veröffentlicht oder zur Veröffentlichung vorgelegt. Diese Arbeit ist unter Einhaltung der Regeln guter wissenschaftlicher Praxis der Deutschen Forschungsgemeinschaft entstanden.

Kiel, den 20. Juni 2015

Christine Andersen

Referent:

Professor Dr. Lars Rüpke

Korreferent:

Professor Dr. Mark Hannington

Tag der mündlichen Prüfung:

21. Juli 2015

Zum Druck genehmigt:

21. Juli 2015

Acknowledgments

Most and primary thanks I direct to my supervisor Lars Rüpke, who was giving me the kick-start into the exciting world of Mid-ocean ridges and hydrothermal systems and who never seemed tired to search for answers and provide me with advise. I am grateful for the years of cooperation including countless hours spent together in front of computer screens hunting numerical bugs and traps. Moreover many thanks go to Sven Petersen, who supported my work during the last years and was providing valuable scientific input. I also thank Ingo Grevemeyer who contributed data and ideas on the Logatchev field, which is an essential part of this thesis. Moreover my working group at the Geomar I thank for the good atmosphere during all the time and many interesting scientific discussions: special thanks to Jörg Hasenclever for important input to the Logatchev study and for numerical support. Ewa Burwicz was a great desk-buddy, always open for a chat on scientific or all other sorts of topics and sensitive for quietness when needed. Sonja Theissen-Krah I thank for her company and much appreciated exchange of scientific thoughts. I further thank Javier Escartin and Charlie Langmuir to offer me the great opportunity to participate on the Mid-Atlantic Ridge cruise on the now retired R/V Knorr. I thank my family and friends, who always believed in me. My father was supporting my early curiosity and passion for rocks, math and scientific questions in general since I can think, I am very thankful for that. I am grateful that Andrea was feeding me with delicious food and simply that he is with me. The friendship of Sarah and Kathrin is irreplaceable and gave more color to many situations and made others much more light. Last but not least (!) I thank 175g of flying plastic for endless hours of joy and my ultimate team for distracting me and not asking too much about my thesis.

Contents

Kurzfassung	13
Abstract	15
1 Introduction	17
1.1 Background of this work	18
1.2 Research aim & thesis outline	21
1.3 General numerical modeling approaches	23
1.3.1 Conservation principles	24
1.3.2 Finite Differences	25
1.3.3 The Finite Element Method	27
I. Submarine hydrothermal systems	35
2 Background on submarine hydrothermal circulation	37
2.1 Definition of a hydrothermal system & basic process	37
2.2 Hydrothermal activity at oceanic spreading centers	39
2.2.1 Discovery of submarine hot springs	41
2.2.1.1 Early evidence for fluid convection in the oceanic crust	41
2.2.1.2 Discovery of the first hydrothermal vent fields on the seafloor	42
2.2.2 Classification and characteristics of submarine hydrothermal systems	43
3 Numerical simulation of hydrothermal circulation	49
3.1 Development of hydrothermal convection models	49
3.2 2D hydrothermal flow model applied in this work	51
3.2.1 Governing equations	51
3.2.1.1 Darcy's Law of fluid flow	51
3.2.1.2 Conservation of mass and energy	52

3.2.2	Numerical formulation and solution techniques	54
3.2.3	Boundary conditions	56
4	Fault geometry and permeability contrast control vent temperatures at the Logatchev 1 hydrothermal field	59
	Abstract	59
4.1	Introduction	60
4.2	The Logatchev 1 hydrothermal field	61
4.3	Modeling framework and setup	61
4.4	Simulation results	63
4.5	Discussion	67
4.6	Summary & Conclusions	69
5	Energetics of hydrothermal circulation in heterogeneous ocean crust	73
	Abstract	73
5.1	Introduction	73
5.2	Theoretical framework	75
5.3	Simulation results	77
5.3.1	Homogeneous and simple layered systems	77
5.3.2	Heterogeneous systems including a vertical slot	78
5.3.3	Heterogeneous, faulted systems	83
5.4	Discussion	85
5.5	Summary & Conclusions	87
II.	Seafloor spreading	89
6	Background on oceanic ridges	91
6.1	Characteristics of ridges at different spreading rates	91
6.2	Background for mechanical modeling	94

6.2.1	Stress and strain analysis	94
6.2.1.1	The stress tensor	94
6.2.1.2	Deformation and strain	96
6.2.2	Rheology and deformation mechanisms in rocks	99
6.2.2.1	Viscous flow	100
6.2.2.2	Elastic deformation	100
6.2.2.3	Visco-elastic rheology	101
6.2.2.4	Plasticity	104
7	Seafloor spreading under varying tectono-magmatic conditions	107
	Abstract	107
7.1	Background	108
7.2	Mechanical model	109
7.2.1	Governing equations	110
7.2.2	Numerical formulation	112
7.2.2.1	Numerical scheme	115
7.2.3	Model set up	116
7.3	Simulation results	118
7.4	Discussion & Conclusions	122
8	Discussion & Implications	125
9	Conclusions & Outlook	131
	Complete Reference List	134
	Appendix – Glossary, mathematical symbols and abbreviations used	144

Kurzfassung

Segmente des langsam-spreizenden Mittelatlantischen Rückens durchlaufen abwechselnd Perioden tektonischer und magmatischer Krustenbildung. Ein Hauptziel dieser Arbeit ist es die Hypothese, dass das tektonisch-magmatische Stadium langsam-spreizender Rückensegmente die Position hydrothermaler Quellen kontrolliert, zu beweisen. Hydrothermale Aktivität würde während magmatischer Phasen nahe der Rückenachse auftreten und wäre in tektonischen Phasen von Störungszonen kontrolliert und würde in einer Entfernung zur Rückenachse auftreten. Weiterhin tragen die Ergebnisse, die hier präsentiert werden, dazu bei neue Einsichten über das Zwischenspiel von Permeabilität assoziiert mit z.B. Rissen und Störungszonen, Magmatismus und hydrothermaler Zirkulation in der ozeanischen Lithosphäre zu gewinnen.

Numerische Simulationen wurden mit zwei verschiedenen 2D Finite Elemente Codes durchgeführt. Ein mechanisches Model wurde entwickelt, welches für voll visko-elastisch-plastische Deformation der Lithosphäre an ozeanischen Rücken löst. Modellierung der Meeresbodenspreizung unter variierenden tektono-magmatischen Konditionen zeigt wie Krustenausdünnung und spröde Deformation entlang von Brüchen mit der Dominanz tektonischer Prozesse, wenn der Rückenachse weniger Magma zugeführt wird, zunimmt. Die Zirkulation hydrothermaler Fluide in der ozeanischen Kruste wird mit einem Model für poröses Fließen simuliert, welches für die Konvektion von inkompressiblem Wasser löst. Es wird dargestellt wie Permeabilitätskontraste in der Lithosphäre die Temperatur, den Massenfluss und die Energiebilanz submariner Hydrothermalfluide während des Aufstiegs zum Meeresboden kontrollieren. Die Kontrolle permeabler Störungszonen über Temperaturen und Fließmuster hydrothermaler Fluide wird am Logatchev 1 Hydrothermalfeld am Mittelatlantischen Rücken als Typbeispiel untersucht. Das Logatchevfeld ist mit einer aktiven tektonischen Störungzone assoziiert. Gemessenen Mikroseismizität und Meeresbodenbathymetrie sind im Model inkludiert. Hochtemperatur-hydrothermalfluide können nur effizient durch permeable Störungszonen fließen, welche nicht zu breit oder zu durchlässig sind. Ansonsten tritt ein deutlicher Temperaturabfall als Konsequenz von

Durchmischung mit eindringendem kaltem Meerwasser auf. Die Ergebnisse weisen darauf hin, dass eine signifikante Menge hydrothermaler Zirkulation an langsam-spreizenden Rücken, welche häufig mit permeablen Störungszonen assoziiert sind, mit niedrigeren Temperaturen als an schnell-spreizenden Rücken auftritt. Dies ist potenziell wichtig für die Abschätzung der globalen Ausbreitung von SMS Vorkommen an ozeanischen Rücken, welche sich am effizientesten bilden wenn die Temperaturen von Hydrothermalfluiden höher als $\sim 300^{\circ}\text{C}$ sind.

Die kombinierten Ergebnisse der Modellierung von hydrothermalen Fließprozessen und des mechanischen Modells für die Deformation ozeanische Rücken zeigen wie die Position hydrothermaler Quellen von unterschiedlichen Stilen der Meeresbodenspreizung kontrolliert wird. Dies bestätigt die anfängliche Hypothese dieser Arbeit: die Lage der Wärmequelle kontrolliert die Position von hydrothermalen Quellen am Meeresboden in der Achsenregion unter magmatischen Konditionen, während die Position der Quellen in tektonischen Phasen von permeablen Störungszonen kontrolliert werden, welche in einer Entfernung zur Rückenachse am Meeresboden enden.

Abstract

Segments of the slow-spreading Mid-Atlantic Ridge (MAR) undergo shifting periods of tectonic and magmatic crustal accretion. A key goal of this work was to prove the hypothesis stating that the tectono-magmatic state of slow-spreading ridge segment control the position of hydrothermal vent sites: hydrothermal venting would occur in the axial region during magmatic phases and would be fault-controlled and occur in a distance to the ridge axis during periods dominated by tectonic activity. Further the results presented here provide new insights about the interplay of permeability associated with e.g. fractures and faults, magmatism and hydrothermal circulation in oceanic lithosphere.

Numerical simulations were conducted using two different Finite Element based 2D codes. A mechanical model has been developed that solves for the fully visco-elasto-plastic deformation of the lithosphere at oceanic ridges. Modeling of seafloor spreading under varying tectono-magmatic conditions show how crustal thinning and brittle faulting is increasing with dominance of tectonic processes, where less magma is supplied to the ridge axis. The circulation of hydrothermal fluids in the oceanic crust is simulated by applying a porous flow model, which solves for the convection of incompressible pure water. How permeability contrasts in the lithosphere control temperature, mass flux and the energy balance of submarine hydrothermal fluids during their ascent to the seafloor is illustrated. The control of permeable fault zones on hydrothermal vent temperatures and flow pattern is investigated at the Logatchev 1 hydrothermal field on the MAR as type example. The Logatchev field is associated with an active tectonic fault zone. Measured microseismicity and seafloor bathymetry is included in the model. High-temperature hydrothermal fluids can only efficiently flow along permeable fault zones that are not too permeable or wide, otherwise a distinct temperature drop as the result of mixing with entraining cold seawater occurs. The results imply that a significant amount of the hydrothermal circulation at slow-spreading ridges, which are frequently associated with permeable fault zones, is occurring at lower temperatures than at fast-spreading ridges. This implication is potentially important for the global estimate of SMS deposits at oceanic ridges, which most efficiently

form if hydrothermal fluid temperatures are higher than $\sim 300^{\circ}\text{C}$.

The combined results from hydrothermal flow modelling and lithosphere-scale mechanical model of oceanic ridges demonstrate how vent site location is controlled by different styles of seafloor spreading, which confirms the initial hypothesis of this work: the position of the heat source controls the location of on-axis hydrothermal vents at the seafloor under magmatic conditions while the location is controlled by permeable fault zones that are outcropping in a distance to the ridge axis under tectonic conditions.

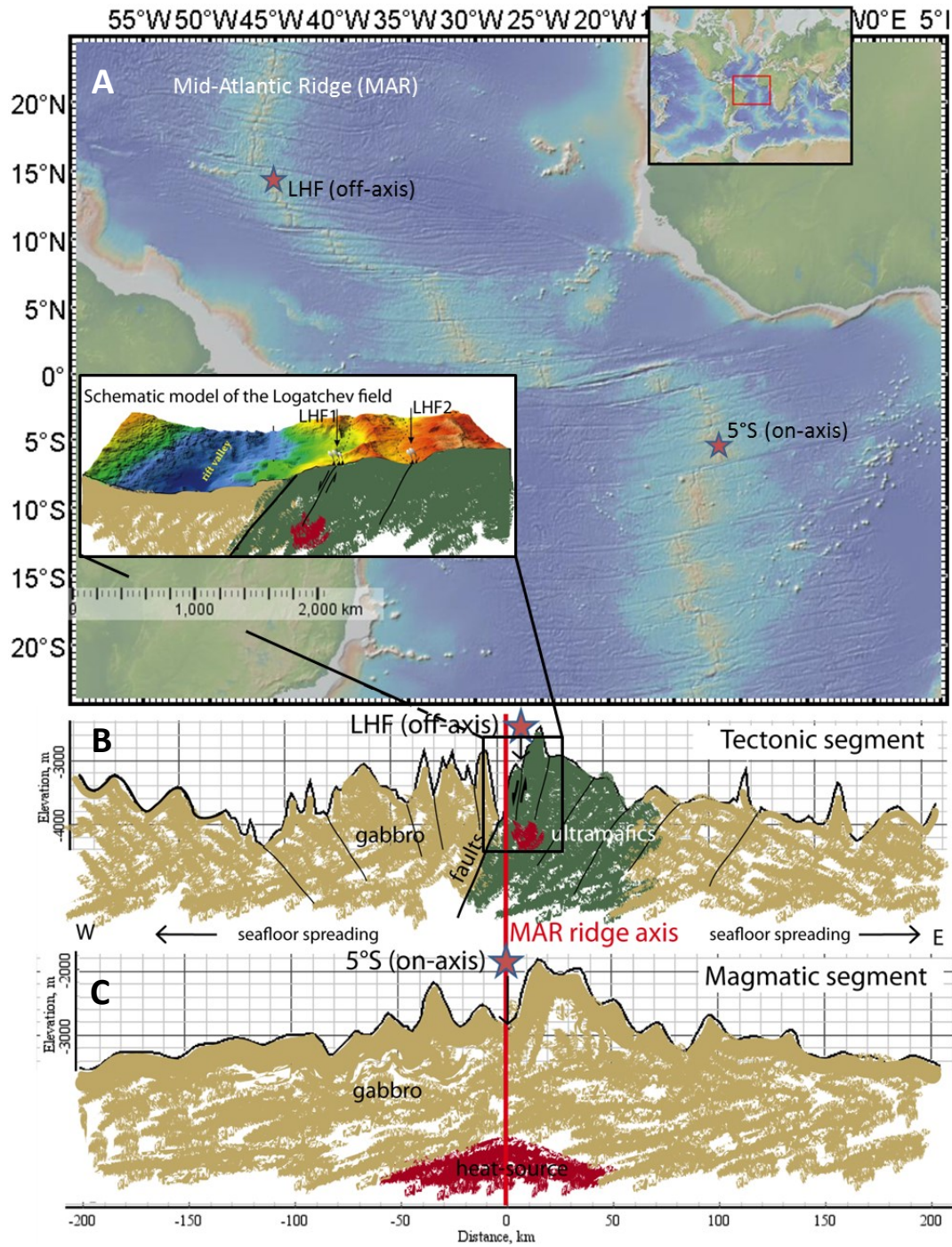
1 Introduction

Just about one and a half decade after the discovery of seafloor spreading centers in the mid 1960's (see Chapter 6), oceanic ridges were directly investigated and another highly exciting discovery was made: the first hydrothermal springs, expelling hot fluids from chimney like structures at the seafloor, were sighted with manned submersibles along the East Pacific Rise (see section 2.2.1, Corliss et al., 1979; Spiess et al., 1980). Several scientific fields have significantly benefited from this discovery. Submarine hydrothermal systems efficiently cool the young oceanic crust helping to better understand the Earth's global heat budget. It was possible to make more accurate global heat flux estimates taking into account the large quantity of heat advected into the oceans at hydrothermal vent sites (Macdonald et al., 1980; Hamza et al., 2008; Hutnak et al., 2008; Pollack and Chapman, 2008). Hydrothermal circulation efficiently transports energy and mass through the interface between oceanic crust and the ocean. Roughly a third of the heat transported globally through the ocean floor is estimated to occur by convection via submarine hydrothermal discharge (Lowell et al., 1995; Hutnak et al., 2008). Furthermore it is calculated to be responsible for a quarter of the total heat loss from the interior of the Earth in contrast to continental systems, which only transport ~1% of the total heat (Lowell et al., 1995; Coumou et al., 2008). Hydrothermal vent sites host extraordinary ecosystems in extreme environmental conditions in the deep oceans far away from any source of light and at high pressure (Spiess et al., 1980; Grassle, 1985; Martin et al., 2008). Moreover, potential ore deposits form as a byproduct of hydrothermal circulation in the oceanic crust (Hannington et al., 1995; Rona, 2008; Schardt and Large, 2009; Hannington, 2014). Until the discovery of submarine hydrothermal systems, Volcanogenic Massive Sulphide deposits were only known and mined on land. After the discovery of submarine hot springs it became clear, that Submarine Massive Sulphide (SMS) deposits form around active black smoker sites at the seafloor, where the contact of

hot hydrothermal fluids with cold seawater causes dissolved metals in hydrothermal fluids to precipitate sulfide minerals at the vent chimneys (German and Seyfried Jr, 2014). The detection of SMS deposits on the seafloor at hydrothermal vent sites along oceanic ridges was also a major step for the assessment of the economic potential of marine ore deposits (Rona, 2008; Hannington et al., 2011). Nevertheless, many fundamental questions about submarine hydrothermal systems remain open. Hydrothermal vent sites are being directly investigated with deep diving instruments, which are powerful tools for data collection and have become increasingly precise. Numerical modelling provides another effective method to study hydrothermal processes in the oceanic crust. From fluid flow modeling we can learn about fundamental thermodynamic processes of hydrothermal convection in the crust (Geiger et al., 2005; Coumou et al., 2006; Lewis and Lowell, 2009; Driesner, 2010; Weis et al., 2014). Parameters that control mineral and metal deposition around vent sites at the seafloor like flow pattern, heat and mass flux as well as crustal permeability structure can be simulated (Schardt and Large, 2009; Weis and Driesner, 2013; Hasenclever et al., 2014; Weis, 2015).

1.1 Background of this work

New oceanic crust is continuously formed by tectonic and magmatic processes at submarine oceanic ridges (see also part II). Tectonic plates are separating at these seafloor-spreading centers (Fig. 1.1a) with varying velocity. In theory active tectonic processes decrease with spreading rate while magmatic activity increases (Baker and German, 2004). When tectonic processes are dominating like at slow-spreading ridges, crustal structure and dynamics are more complex than at fast-spreading ones. Slow-spreading ridge segments, however, like at the Mid-Atlantic Ridge (MAR), undergo shifting periods of magmatic and tectonic phases (Escartin et al., 2008). During tectonically dominated periods, seafloor spreading occurs asymmetric to the ridge axis via large scale faults (Escartin et al., 2008). In this mode the extensional



deformation of the crust is not fully balanced by magmatic accretion. Detachment faults which expose Oceanic Core Complexes (ridge perpendicular bodies of ultramafic rocks from the lower crust or upper mantle with typical corrugated surfaces) onto the flanks of the axial rift valley are common (e.g. Tucholke et al., 2008; MacLeod et al., 2009). Tectonic faulting also controls the circulation of hydrothermal fluids in such settings, like at the MAR vent fields Logatchev (e.g. Schmidt et al., 2007; Petersen et al., 2009), Rainbow (e.g. Douville et al., 2002) and TAG (e.g. Canales et al., 2007; deMartin et al., 2007; Humphris et al., 2015), which all appear distal to the ridge axis. Other hydrothermal sites along the MAR are associated with ridge segments that show recent magmatic activity and are located on-axis. The Lucky Strike (Langmuir et al., 1997; Dusanur et al., 2009; Ondréas et al., 2009) and 5°S (e.g. Haase et al., 2007; Koschinsky et al., 2008) vent systems as well Snakepit (Karson and Brown, 1988), Broken Spur (James et al., 1995) and Menez Gwen (Charlou et al., 2000) are examples of this. At intermediate to fast-spreading ridges practically all hydrothermal venting occurs on-axis, close to the typically narrow basaltic neovolcanic zone (Baker and German, 2004).

The above described characteristics of hydrothermal activity at slow-spreading ridges let me hypothesize about *a relationship between the position of hydrothermal vent fields and the tectonic state of slow-spreading ridge segments.*

During magmatic phases slow spreading ridges might behave more similar to fast spreading ones with hydrothermal venting occurring in the basaltic hosted axial

Figure 1.1 previous page: Illustration of key hypothesis of this work: off-axis hydrothermal activity as a consequence of tectonic dominance (**B**) at segments of slow-spreading ridges like the MAR (**A**); the ultramafic hosted LHF1 hydrothermal field is an example for such a scenario (**B**). The schematic model of the Logatchev field (**B-close up**, modified from Petersen et al., (2009)) includes ship based seafloor bathymetry of the area and illustrates the off-axis location of the LHF vent fields associated with an outcropping, ultramafic detachment fault surface. When magmatic accretion is dominating during seafloor spreading hydrothermal activity occurs vertically above the axial driving heat source (**C**). The topographic basemap of the MAR (**A**) has been created with the GMRT data (Ryan et al., (2009)) in GeoMapApp (<http://www.geomapapp.org>). Also the two bathymetric profiles (**B** and **C**) have been extracted from GeoMapApp, they have vertical exaggeration of 30.

valley, with an on-axis magmatic heat source (e.g. Lucky Strike, 5°S). During asymmetric, tectonic spreading phases, parameters which are secondary at fast-spreading conditions such as auxiliary heat sources, detachment faulting and crustal permeability, might well become the major controlling factors of hydrothermal activity (see also Baker and German, 2004). Auxiliary heat sources could be gabbroic intrusions and/or serpentinization processes in ultramafic rocks (e.g. Baker and German, 2004; Schmidt et al., 2011). During asymmetric tectonic spreading, magma is injected into the footwall of a detachment fault rather than into its hanging wall (Escartin et al., 2008; MacLeod et al., 2009). This could serve as driving off-axis heat source for hydrothermal circulation in a distance to the ridge axis.

Since both the research of oceanic ridge systems as well as of the associated hydrothermal processes is rather young (see sections 2.2.1 and Chapter 6), many fundamental questions still remain unanswered. Direct investigations of the seafloor with deep diving instruments are powerful tools for data collection which now become increasingly precise. An additional efficient way of studying seafloor spreading and hydrothermal processes is by numerical modelling. From mechanical models we can learn about central processes during the creation of new oceanic crust such as tectonic faulting (Buck and Poliakov, 1998; Buck et al., 2005; Behn and Ito, 2008). Porous flow models can teach us about key thermodynamic parameters of hydrothermal fluid circulation beneath the seafloor like heat, energy and mass fluxes as well as flow patterns (Coumou et al., 2008; Ingebritsen et al., 2010).

1.2 Research aim & thesis outline

The key goal of this work is to test the above hypothesis stating that the tectonic state of slow-spreading ridge segments controls the position of hydrothermal vent fields. During magmatic dominated phases venting would occur in the neovolcanic zone at the ridge axis while venting would be fault controlled and shift to off-axis

regions during tectonic phases. Moreover this work seeks to gain new insights on the interplay of permeability e.g. associated with fractures and fault zones and hydrothermal circulation in oceanic lithosphere at varying tectono-magmatic conditions.

The above objectives are approached by numerical simulations using different 2D codes. A fluid flow model of porous convection of hydrothermal fluids in the oceanic crust is combined with a lithosphere-scale, mechanical model that solves for the fully visco-elasto-plastic deformation of the lithosphere during seafloor spreading under varying tectono-magmatic conditions. Using such combined modelling approach will help to find explanations for different styles of venting observed at oceanic ridges and mark a key step forward in our quantitative understanding about the interplay of faulting, magma supply and hydrothermal processes at varying ridge spreading rates.

The following two chapters (Chapters 2 and 3) give a scientific geological and numerical modeling background on submarine hydrothermal systems respectively. In chapter 4 the control of a permeable fault zone on hydrothermal vent temperatures and flow pattern is investigated using the Logatchev 1 hydrothermal field on the Mid-Atlantic ridge as a type example, which is known to be associated to active tectonic faulting. How permeability contrasts in the lithosphere affect the energy balance during hydrothermal fluid flow is studied in further detail in chapter 5. Chapter 6 provides a background on relevant processes related to seafloor spreading at oceanic ridges. Results from mechanical modeling of seafloor spreading under varying tectono-magmatic conditions are presented in chapter 7, representing ridge segments under different conditions at varying spreading rates. Implications from the scientific findings of this work and remaining open questions are discussed in chapter 8. Concluding remarks are made in the last chapter 9 also with respect to how the results from this work relate to the above hypothesis.

1.3 General numerical modeling approaches

The simulation of natural processes with numerical models naturally has its limitations. Complex processes must be simplified in a way that they can be reproduced by computational power. Assumptions and simplifications must be made about processes that often are not fully understood. Assumptions about submarine hydrothermal circulation or seafloor spreading are difficult to validate as the processes take place within the oceanic lithosphere, where direct observations are challenging. During each numerical modeling activity, the question naturally arises, of how precisely the model can simulate the real system. However no numerical model will ever or shall aim to simulate a natural system. Numerical modeling can help to better understand basic physical processes that are active in any natural system. If the basic processes for a model set-up, which aims to investigate specific problems, are well understood, a model can be elevated to higher complexity by e.g. including more variable parameters or by conducting simulations in more dimensions. Furthermore modeling results strongly depend on assumptions made, model set up chosen and parameter input. Numerical models can certainly benefit if field data is used as input and/or simulation results are compared to measured field data, as has been done in this work for the numerical study of the Logatchev hydrothermal field (Chapter 4).

Geodynamic processes like the mechanical deformation of the oceanic crust during seafloor spreading (viscous flow) as well as the flow of fluids in hydrothermal systems (porous flow) can be mathematically described by systems of nonlinear partial differential equations which mostly contain more than one independent variable (PDEs). Together with elementary assumptions, the definition of a model domain, conditions for the boundaries and initial conditions they are the basis of any numerical modelling activity. It is not possible for most complex systems to derive analytical solutions. Luckily equations can be solved computationally by numerical techniques. In the following section the Finite Difference (FD) (e.g.

Ismail-Zadeh and Tackley, 2010) and Finite Element (FE) method (e.g. Hughes, 2000; Zienkiewicz and Taylor, 2000) are introduced, which are widely used in geodynamic modeling. The FE approach is applied as central solution strategy in both numerical models presented in this work.

1.3.1 Conservation principles

The governing equations describing geodynamic processes follow the basic physical laws of conservation of *mass*, *momentum* and *energy* (e.g. Bear, 1988; Turcotte and Schubert, 2002; Ismail-Zadeh and Tackley, 2010). Major rock units, like the Earth's crust and mantle, are considered to be continuous on a macroscopic scale. A continuous medium has no mass-free voids, i.e. any pores or fractures are assumed to be filled with a continuous substance. This further implies that any movement of points inside this medium must not create gaps and new material has to come in place of the displaced part (e.g. Gerya, 2010). The continuity equation thus describes the *conservation of mass* during the displacement of a continuous medium. Fluid dynamics studies the motion of fluids, which are also assumed to be a continuous medium, in response to applied forces. This deformation process has already been described by Newton's 2nd law of motion:

$$f=ma,$$

that relates changes in velocity of an object, its acceleration a with mass m to the force f acting on it. The momentum equation (see also Stokes equation, section 7.2.1) describes the *conservation of momentum*, which can be velocity, acceleration or displacement (Ranalli, 1995), for a continuous medium in the gravity field and is the differential equivalent to Newton's Law of motion.

The heat equation (section 1.3.4 and 3.2.1.2) describes the *conservation of* (thermal) *energy* and expresses changes in temperature of a continuous medium due to conductive or advective heat transport or due to other sources that generate internal heat by e.g. viscous dissipation, the heat generated by internal friction of the fluid or in a geological context, e.g. the decay of unstable radiogenic isotopes or

exothermic reactions such as the serpentinization of ultramafic rocks.

In systems which are locally not in thermodynamic equilibrium, physical processes take place in order to reach stable conditions. During a numerical simulation a system is balanced when the entire system has reached *steady-state* conditions, where the energy entering the system is equal to the energy leaving it and modelled variables remain constant in time.

1.3.2 Finite Differences

Mathematical derivatives can be approximated applying numerical differentiation. The Finite Difference (FD) method is a basic numerical concept which uses forward, backward or central finite difference expressions in order to approximate differential equations that describe physical processes. Such a differential equation (e.g. Equ. 1.3) is reduced to a discrete equation (Equ. 1.6), which can be solved numerically. For this a continuous domain has to be divided into a grid of discrete points (Fig. 1.2), at which approximate solutions are calculated. Values in between these points have to be interpolated.

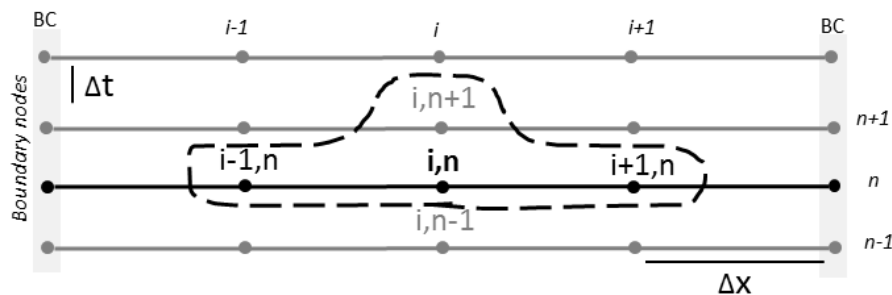


Figure 1.2: 1D Finite Difference grid with a discrete number (5) of nodes. Spatial dimension is displayed in horizontal direction (x) and time (t) vertically. The current timestep is denoted by n , ($n-1$) is the previous and ($n+1$) the following timestep. The nodes which are included in the explicit forward FD scheme (Equ. 1.7) are marked by the dashed line. Unknown temperature at time ($n+1$) and current node position i are expressed in terms of the three known temperatures values of the current timestep n including the two neighboring nodes ($i-1$) and ($i+1$). Boundary conditions (BC) have to be specified at the two edge nodes, marked by the grey shaded areas.

From Fourier's Law of thermal conduction, describing conductive heat flow q_{heat} in dependence of gradients in temperature T and thermal conductivity κ :

$$q_{heat} = -k\nabla T \quad (1.1)$$

the time dependent 1D heat diffusion equation can be derived, which describes the change in thermal energy ($J=\rho*cp*T$) of an incompressible fluid over one time interval as the change in conductive heat flux at a specific coordinate x in space:

$$\rho cp \frac{\partial T}{\partial t} = \frac{\partial}{\partial x} \left(\kappa \frac{\partial T}{\partial x} \right) \quad (1.2)$$

where ρ is density, cp heat capacity, T denotes temperature, x the spatial coordinate and t time. This equation can be solved numerically by an explicit FD scheme, where unknown future temperatures are calculated using known values from the previous timestep (Fig. 1.1), as follows. If ρ , cp and κ are assumed constant they can be taken out of the derivative, and we obtain:

$$\frac{\partial T}{\partial t} = \frac{\kappa}{\rho cp} \frac{\partial^2 T}{\partial x^2} \quad (1.3)$$

The partial derivative can be replaced by its forward (in time) finite difference approximation:

$$\frac{\partial T}{\partial t} \approx \frac{T_i^{n+1} - T_i^n}{t^{n+1} - t^n} = \frac{T_i^{n+1} - T_i^n}{\Delta t} \quad (1.4)$$

Letter n denotes indices in time and i space indices, as visualized in the schematic numerical grid (Fig. 1). The second spatial derivative is written as a central finite difference approximation:

$$\frac{\partial^2 T}{\partial x^2} = \frac{\partial}{\partial x} \left(\frac{\partial T}{\partial x} \right) \approx \frac{\frac{T_{i+1}^n - T_i^n}{\Delta x} - \frac{T_i^n - T_{i-1}^n}{\Delta x}}{\Delta x} = \frac{T_{i+1}^n - 2T_i^n + T_{i-1}^n}{\Delta x^2} \quad (1.5)$$

When equations 1.4 and 1.5 are substituted into equation 1.3 we obtain:

$$\frac{T_i^{n+1} - T_i^n}{\Delta t} = K_{diff} \left(\frac{T_{i+1}^n - 2T_i^n + T_{i-1}^n}{\Delta x^2} \right) \quad (1.6)$$

where $K_{diff} = \frac{\kappa}{\rho c p}$ is the rock's thermal diffusivity. If equation 1.6 is rearranged such that all known temperatures are on one side:

$$T_i^{n+1} = T_i^n + K_{diff} \Delta t \left(\frac{T_{i+1}^n - 2T_i^n + T_{i-1}^n}{\Delta x^2} \right) \quad (1.7)$$

it can be solved for the unknown temperature T_i^{n+1} at time $n+1$. In this discretized form differential equations can be solved numerically, depending on the size of the problem this can be done by hand or by computation.

1.3.3 The Finite Element Method

Similar to the FD method, the basic principle of the FE method is the discretization of a continuous problem into discrete subdomains (elements) for which approximate partial solutions of differential equations describing physical processes can be found (e.g. Bear, 1988; Hughes, 2000; Zienkiewicz and Taylor, 2000). These subdomains are called *finite elements* and are formed by a grid with a defined number of nodes (Fig. 1.3). Differently however to the FD method, the FE method approximates solutions throughout the whole model domain and not just at the discrete nodal points. Functions are solved per element but are added together to contribute to the global solution over the whole model domain. The advantage of the FE method is that elements do not need to be uniform, so that complex shapes and structures can be represented by unstructured meshes (Fig. 1.3). The mathematical principle of the FE method is the replacement of the governing equations by integral formulations. Approximated solutions are computed at each

numerical grid point with reference to neighboring nodes and interpolated into associated elements. Nodal values are interpolate \tilde{T} onto points inside elements by *shape functions* N , such that the approximate solution at coordinate (x,y) inside

the element is:
$$\tilde{T} = NT.$$

The basic FE approach is demonstrated on the example of the 2D heat diffusion equation (Equ. 1.8). For simplicity the steady diffusion equation is considered, where the heat flux is constant in time such that the time derivative on the left hand side (lhs) (see equation 1.3 above) equals zero and constant thermal diffusivity K_{diff} can be neglected. We obtain following simple expression for a constant 2D heat flux:

$$\frac{\partial^2 T}{\partial x^2} + \frac{\partial^2 T}{\partial y^2} = 0 \quad (1.8)$$

that we want to solve numerically using the FE technique. Since numerically we are only able to obtain approximate solutions for temperature, equation 1.8 is not strictly fulfilled. Equation 1.8 is turned into an integral expression over model domain Ω , where the integral is forced to zero instead:

$$\int_{\Omega} \delta \left(\frac{\partial^2 T}{\partial x^2} + \frac{\partial^2 T}{\partial y^2} \right) d\Omega = 0 \quad (1.9)$$

Since equation 1.9 is only an approximation of equation 1.8 , it is called *weak*. The residual error between approximation and exact solution is denoted by δ . In the weighted residuals method it is weighted over the whole domain in order to be minimized. The FE approximation of the governing equation 1.8 is given by:

$$\frac{\partial^2 T}{\partial x^2} + \frac{\partial^2 T}{\partial y^2} \approx \int_{\Omega} N^i \left(\frac{\partial^2 NT}{\partial x^2} + \frac{\partial^2 NT}{\partial y^2} \right) d\Omega = 0 \quad (1.10)$$

In this FE approximation the transposed of the shape functions are also used as

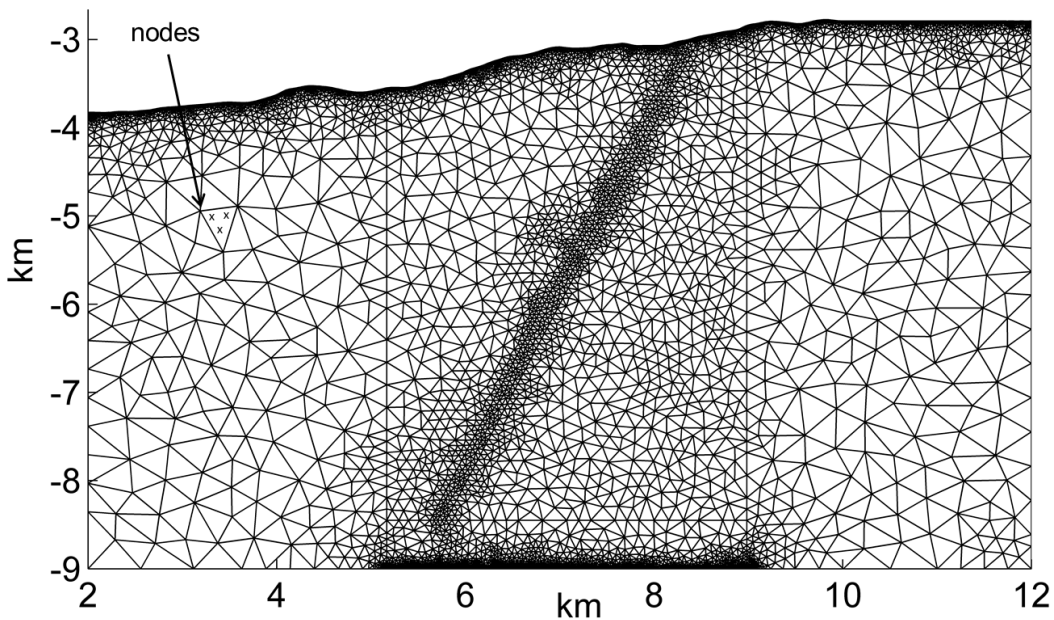


Figure 1.3: FE mesh consisting of 5654 nodes, which form 10.457 triangular 3-node elements of varying size. Integration points are marked by the three crosses inside one element. Complex geometries can well be resolved by unstructured FE-meshes, like the seafloor bathymetry at the top of the model domain. The displayed mesh is a low resolution version of the LHF1 model domain in chapter 4.

weighting functions for the residual error, which is called Galerkin method. The number of shape functions equals the number of nodes per element and can be written in coordinates referring to the global grid or in local coordinates referring to the element. If written in local coordinates the advantage is that they can handle any element shape. Each shape function has value 1 at one node and zero at all others (Fig. 1.4) such that the sum of all shape functions equals 1 at any point inside each element.

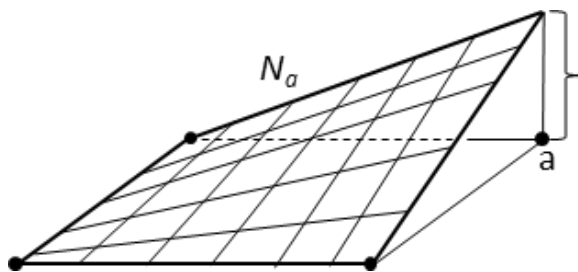


Figure 1.4: Example shape function N_a for node **a** of a quadratic element. N_a has value 1 at node **a** and zero at all three other nodes. The sum of all four shape functions thus equal 1 at any point inside the element.

Each finite element is assigned an identifying integer number, each nodal point is assigned a global identifying integer, plus *local coordinates* that directly refer to the grid. A *Jacobian matrix* is used to switch between global and local coordinates. Which nodes belong to which element is defined by a *connectivity matrix*.

The second derivatives are removed from equation 1.10 applying the partial integration rule for an integral over a product of two functions:

$$\int_{\Omega} uv'd\Omega = -\int_{\Omega} u'vd\Omega + \oint_{\Gamma} uvd\Gamma \quad (1.11)$$

We define that function $u = N'$ and $v = \left(\frac{\partial^2 N}{\partial x^2} + \frac{\partial^2 N}{\partial y^2}\right)$ and obtain:

$$\int_{\Omega} N' \left(\frac{\partial^2 N}{\partial x^2} + \frac{\partial^2 N}{\partial y^2}\right) T d\Omega = -\int_{\Omega} \left(\frac{\partial N'}{\partial x} \frac{\partial N}{\partial x} + \frac{\partial N'}{\partial y} \frac{\partial N}{\partial y}\right) T d\Omega + \oint_{\Gamma} \left(\frac{\partial N}{\partial x} + \frac{\partial N}{\partial y}\right) T d\Gamma \quad (1.12)$$

The boundary integral will turn into a heat flux boundary term, which will equal zero, assuming that no heat is entering or leaving our model domain. We now have the final FE form of the steady 2D heat diffusion equation that we can solve numerically:

$$-\int_{\Omega} \left(\frac{\partial N'}{\partial x} \frac{\partial N}{\partial x} + \frac{\partial N'}{\partial y} \frac{\partial N}{\partial y}\right) T d\Omega = 0 \quad (1.13)$$

Applying numerical integration the integral over the model domain is approximated by the sum of approximated solutions at *integration points* inside each element (see Fig. 1.3):

$$-\int_{\Omega} \left(\frac{\partial N'}{\partial x} \frac{\partial N}{\partial x} + \frac{\partial N'}{\partial y} \frac{\partial N}{\partial y}\right) T d\Omega \approx -\sum_{i=1}^{nip} \left(\frac{\partial N'}{\partial x} \frac{\partial N}{\partial x} + \frac{\partial N'}{\partial y} \frac{\partial N}{\partial y}\right) T \frac{\Omega}{nip} = 0 \quad (1.14)$$

Each element contributes to the global matrix equation system $\{A\}[x]=[b]$, where $\{A\}$ is a coefficient matrix that in our example contains the derivatives of the shape functions, $[x]$ is a vector of unknown parameters, in our case temperatures T and

[b] a vector of known values, in our case it contains zeros. System of equations like above can be solved for the vector of unknown variables [x] using various algorithms depending on the size of the matrix system and characteristics of the coefficient matrix (e.g. sparsity, symmetry). Direct methods like e.g. Gauss elimination, LU- or Cholesky factorization can be used if the problem is linear and not too large such that it does not require too much computational time and also if the matrix is not sparse. For large, sparse systems iterative methods like e.g. the Jacobi –, Gauss-Seidel – or Conjugate gradient method can be used, where the residual error is minimized in each iterative step (e.g. Ismail-Zadeh and Tackley, 2010).

References Cited

- Baker, E. T., and German, C. R., 2004, On the global distribution of hydrothermal vent fields, *in* German, C. R., Lin, J., and Parson, M., eds., *Mid-Ocean Ridges: Hydrothermal Interactions Between the Lithosphere and Oceans*, Volume Geophysical Monograph Series: Washington, DC, American Geophysical Union, p. 245 - 266.
- Bear, J., 1988, *Dynamics of Fluids in Porous Media*, Courier Corporation, 764 p.:
- Behn, M. D., and Ito, G., 2008, Magmatic and tectonic extension at mid-ocean ridges: 1. Controls on fault characteristics: *Geochemistry Geophysics Geosystems*, v. 9.
- Buck, W. R., Lavier, L. L., and Poliakov, A. N. B., 2005, Modes of faulting at mid-ocean ridges: *Nature*, v. 434, no. 7034, p. 719-723.
- Buck, W. R., and Poliakov, A. N. B., 1998, Abyssal hills formed by stretching oceanic lithosphere: *Nature*, v. 392, no. 6673, p. 272-275.
- Canales, J. P., Sohn, R. A., and Demartin, B. J., 2007, Crustal structure of the Trans-Atlantic Geotraverse (TAG) segment (Mid-Atlantic Ridge, 26 degrees 10-Minutes-N): Implications for the nature of hydrothermal circulation and detachment faulting at slow spreading ridges: *Geochemistry Geophysics Geosystems*, v. 8, p. 18.
- Charlou, J. L., Donval, J. P., Douville, E., Jean-Baptiste, P., Radford-Knoery, J., Fouquet, Y., Dapigny, A., and Stievenard, M., 2000, Compared geochemical signatures and the evolution of Menez Gwen (37°50'N) and Lucky Strike (37°17'N) hydrothermal fluids, south of the Azores Triple Junction on the Mid-Atlantic Ridge: *Chemical Geology*, v. 171, no. 1-2, p. 49-75.
- Corliss, J. B., Dymond, J., Gordon, L. I., Edmond, J. M., Herzen, R. P. V., Ballard, R. D., Green, K., Williams, D., Bainbridge, A., Crane, K., and Vanandel, T. H., 1979, Submarine thermal springs on the Galapagos Rift: *Science*, v. 203, no. 4385, p. 1073-1083.
- Coumou, D., Driesner, T., Geiger, S., Heinrich, C. A., and Matthai, S., 2006, The dynamics of mid-ocean ridge hydrothermal systems: Splitting plumes and fluctuating vent temperatures: *Earth and Planetary Science Letters*, v. 245, no. 1-2, p. 218-231.

- Coumou, D., Driesner, T., and Heinrich, C. A., 2008, The structure and dynamics of mid-ocean ridge hydrothermal systems: *Science*, v. 321, no. 5897, p. 1825-1828.
- deMartin, B. J., Canales, R. A. R., Canales, J. P., and Humphris, S. E., 2007, Kinematics and geometry of active detachment faulting beneath the Trans-Atlantic Geotraverse (TAG) hydrothermal field on the Mid-Atlantic Ridge: *Geology*, v. 35, no. 8, p. 711-714.
- Douville, E., Charlou, J. L., Oelkers, E. H., Bienvenu, P., Jove Colon, C. F., Donval, J. P., Fouquet, Y., Prieur, D., and Appriou, P., 2002, The rainbow vent fluids (36°14'N, MAR): the influence of ultramafic rocks and phase separation on trace metal content in Mid-Atlantic Ridge hydrothermal fluids: *Chemical Geology*, v. 184, no. 1-2, p. 37-48.
- Driesner, T., 2010, The interplay of permeability and fluid properties as a first order control of heat transport, venting temperatures and venting salinities at mid-ocean ridge hydrothermal systems: *Geofluids*, v. 10, no. 1-2, p. 132-141.
- Dusunur, D., Escartin, J., Combier, V., Seher, T., Crawford, W., Cannat, M., Singh, S. C., Matias, L. M., and Miranda, J. M., 2009, Seismological constraints on the thermal structure along the Lucky Strike segment (Mid-Atlantic Ridge) and interaction of tectonic and magmatic processes around the magma chamber: *Marine Geophysical Researches*, v. 30, no. 2, p. 105-120.
- Escartin, J., Smith, D. K., Cann, J., Schouten, H., Langmuir, C. H., and Escrig, S., 2008, Central role of detachment faults in accretion of slow-spreading oceanic lithosphere: *Nature*, v. 455, no. 7214, p. 790-U795.
- Geiger, S., Driesner, T., Heinrich, C. A., and Matthai, S. K., 2005, On the dynamics of NaCl-H₂O fluid convection in the Earth's crust: *Journal of Geophysical Research-Solid Earth*, v. 110, no. B7.
- German, C. R., and Seyfried Jr, W. E., 2014, Hydrothermal Processes, *in* Turekian, H. D. H. K., ed., *Treatise on Geochemistry (Second Edition), Volume 8*: Oxford, Elsevier, p. 191-233.
- Gerya, T., 2010, *Introduction to Numerical Geodynamic Modelling*, New York, Cambridge University Press.
- Grassle, J. F., 1985, Hydrothermal Vent Animals: Distribution and Biology: *Science*, v. 229, no. 4715, p. 713-717.
- Haase, K. M., Petersen, S., Koschinsky, A., Seifert, R., Devey, C. W., Keir, R., Lackschewitz, K. S., Melchert, B., Perner, M., Schmale, O., Süling, J., Dubilier, N., Zielinski, F., Fretzdorff, S., Garbe-Schönberg, D., Westernströer, U., German, C. R., Shank, T. M., Yoerger, D., Giere, O., Kuever, J., Marbler, H., Mawick, J., Mertens, C., Stöber, U., Walter, M., Ostertag-Henning, C., Paulick, H., Peters, M., Strauss, H., Sander, S., Stecher, J., Warmuth, M., and Weber, S., 2007, Young volcanism and related hydrothermal activity at 5°S on the slow-spreading southern Mid-Atlantic Ridge: *Geochemistry Geophysics Geosystems*, v. 8, no. 11, p. Q11002.
- Hamza, V. M., Cardoso, R. R., and Neto, C. F. P., 2008, Spherical harmonic analysis of earth's conductive heat flow: *International Journal of Earth Sciences*, v. 97, no. 2, p. 205-226.
- Hannington, M., Jamieson, J., Monecke, T., Petersen, S., and Beaulieu, S., 2011, The abundance of seafloor massive sulfide deposits: *Geology*, v. 39, no. 12, p. 1155-1158.
- Hannington, M. D., 2014, Volcanogenic Massive Sulfide Deposits, *in* Turekian, H. D. H. K., ed., *Treatise on Geochemistry (Second Edition), Volume 13*: Oxford, Elsevier, p. 463-488.
- Hannington, M. D., Jonasson, I. R., Herzig, P. M., and Petersen, S., 1995, Physical and Chemical Processes of Seafloor Mineralization at Mid-Ocean Ridges, *in* Humphris, S. E., Zierenberg, R. A., Mullineaux, L. S., and Thomson, R. E., eds., *Seafloor Hydrothermal Systems -*

- Physical, chemical, biological and geological interactions, Volume 91: Washington DC, American Geophysical Union, p. 1-466.
- Hasenclever, J., Theissen-Krah, S., Rupke, L. H., Morgan, J. P., Iyer, K., Petersen, S., and Devey, C. W., 2014, Hybrid shallow on-axis and deep off-axis hydrothermal circulation at fast-spreading ridges: *Nature*, v. 508, no. 7497, p. 508-512.
- Hughes, T. J. R., 2000, *The Finite Element Method: Linear Static and Dynamic Finite Element Analysis*, Dover Publications, Dover Civil and Mechanical Engineering.
- Humphris, S. E., Tivey, M. K., and Tivey, M. A., 2015, The Trans-Atlantic Geotraverse hydrothermal field: A hydrothermal system on an active detachment fault: *Deep Sea Research Part II: Topical Studies in Oceanography*, no. Topical Studies in Oceanography.
- Hutnak, M., Fisher, A. T., Harris, R., Stein, C., Wang, K., Spinelli, G., Schindler, M., Villinger, H., and Silver, E., 2008, Large heat and fluid fluxes driven through mid-plate outcrops on ocean crust: *Nature Geoscience*, v. 1, no. 9, p. 611-614.
- Ingebritsen, S. E., Geiger, S., Hurwitz, S., and Driesner, T., 2010, Numerical simulation of magmatic hydrothermal systems: *Reviews of Geophysics*, v. 47.
- Ismail-Zadeh, A., and Tackley, P. J., 2010, *Computational Methods for Geodynamics*, Cambridge, Cambridge University Press.
- James, R. H., Elderfield, H., and Palmer, M. R., 1995, The chemistry of hydrothermal fluids from the Broken Spur site, 29°N Mid-Atlantic ridge: *Geochimica et Cosmochimica Acta*, v. 59, no. 4, p. 651-659.
- Karson, J. A., and Brown, J. R., 1988, Geologic setting of the Snake Pit hydrothermal site: An active vent field on the Mid-Atlantic Ridge: *Marine Geophysical Researches*, v. 10, no. 1-2, p. 91-107.
- Koschinsky, A., Garbe-Schonberg, D., Sander, S., Schmidt, K., Gennerich, H. H., and Strauss, H., 2008, Hydrothermal venting at pressure-temperature conditions above the critical point of seawater, 5 degrees S on the Mid-Atlantic Ridge: *Geology*, v. 36, no. 8, p. 615-618.
- Langmuir, C., Humphris, S., Fornari, D., Van Dover, C., Von Damm, K., Tivey, M. K., Colodner, D., Charlou, J. L., Desonie, D., Wilson, C., Fouquet, Y., Klinkhammer, G., and Bougault, H., 1997, Hydrothermal vents near a mantle hot spot: the Lucky Strike vent field at 37°N on the Mid-Atlantic Ridge: *Earth and Planetary Science Letters*, v. 148, no. 1-2, p. 69-91.
- Lewis, K. C., and Lowell, R. P., 2009, Numerical modeling of two-phase flow in the NaCl-H₂O system: 2. Examples: *Journal of Geophysical Research-Solid Earth*, v. 114, p. 16.
- Lowell, R. P., Rona, P. A., and Vonherzen, R. P., 1995, Sea-floor hydrothermal systems: *Journal of Geophysical Research-Solid Earth*, v. 100, no. B1, p. 327-352.
- Macdonald, K. C., Becker, K., Spiess, F. N., and Ballard, R. D., 1980, Hydrothermal heat flux of the "black smoker" vents on the East Pacific Rise: *Earth and Planetary Science Letters*, v. 48, no. 1, p. 1-7.
- MacLeod, C. J., Searle, R. C., Murton, B. J., Casey, J. F., Mallows, C., Unsworth, S. C., Achenbach, K. L., and Harris, M., 2009, Life cycle of oceanic core complexes: *Earth and Planetary Science Letters*, v. 287, no. 3-4, p. 333-344.
- Martin, W., Baross, J., Kelley, D., and Russell, M., 2008, Hydrothermal vents and the origin of life: *Nat Rev Micro*, v. 6, no. 11, p. 805-814.
- Ondréas, H., Cannat, M., Fouquet, Y., Normand, A., Sarradin, P. M., and Sarrazin, J., 2009, Recent volcanic events and the distribution of hydrothermal venting at the Lucky Strike hydrothermal field, Mid-Atlantic Ridge: *Geochemistry, Geophysics, Geosystems*, v. 10, no. 2, p.

- Petersen, S., Kuhn, K., Kuhn, T., Augustin, N., Hekinian, R., Franz, L., and Borowski, C., 2009, The geological setting of the ultramafic-hosted Logatchev hydrothermal field (14 degrees 45 ' N, Mid-Atlantic Ridge) and its influence on massive sulfide formation: *Lithos*, v. 112, no. 1-2, p. 40-56.
- Pollack, H. N., and Chapman, D. S., 2008, Comment on "Spherical harmonic analysis of earth's conductive heat flow" by V. M. Hamza, R. R. Cardoso and C. F. Ponte Neto: *International Journal of Earth Sciences*, v. 97, no. 2, p. 227-231.
- Ranalli, G., 1995, *Rheology of the earth*, Chapman & Hall, 413 p.
- Rona, P. A., 2008, The changing vision of marine minerals: *Ore Geology Reviews*, v. 33, no. 3-4, p. 618-666.
- Ryan, W. B. F., Carbotte, S. M., Coplan, J. O., O'Hara, S., Melkonian, A., Arko, R., Weissel, R. A., Ferrini, V., Goodwillie, A., Nitsche, F., Bonczkowski, J., and Zemsky, R., 2009, Global Multi-Resolution Topography synthesis: *Geochemistry, Geophysics, Geosystems*, v. 10, no. 3, p.
- Schardt, C., and Large, R. R., 2009, New insights into the genesis of volcanic-hosted massive sulfide deposits on the seafloor from numerical modeling studies: *Ore Geology Reviews*, v. 35, no. 3-4, p. 333-351.
- Schmidt, K., Garbe-Schönberg, D., Koschinsky, A., Strauss, H., Jost, C. L., Klevenz, V., and Königer, P., 2011, Fluid elemental and stable isotope composition of the Nibelungen hydrothermal field (8°18'S, Mid-Atlantic Ridge): Constraints on fluid-rock interaction in heterogeneous lithosphere: *Chemical Geology*, v. 280, no. 1-2, p. 1-18.
- Schmidt, K., Koschinsky, A., Garbe-Schonberg, D., de Carvalho, L. M., and Seifert, R., 2007, Geochemistry of hydrothermal fluids from the ultramafic-hosted Logatchev hydrothermal field, 15 degrees N on the Mid-Atlantic Ridge: Temporal and spatial investigation: *Chemical Geology*, v. 242, no. 1-2, p. 1-21.
- Spiess, F. N., Macdonald, K. C., Atwater, T., Ballard, R., Carranza, A., Cordoba, D., Cox, C., Diazgarcia, V. M., Francheteau, J., Guerrero, J., Hawkins, J., Haymon, R., Hessler, R., Juteau, T., Kastner, M., Larson, R., Luyendyk, B., Macdougall, J. D., Miller, S., Normark, W., Orcutt, J., and Rangin, C., 1980, East Pacific Rise - Hot springs and geophysical experiments: *Science*, v. 207, no. 4438, p. 1421-1433.
- Tucholke, B. E., Behn, M. D., Buck, W. R., and Lin, J., 2008, Role of melt supply in oceanic detachment faulting and formation of megamullions: *Geology*, v. 36, no. 6, p. 455-458.
- Turcotte, D. L., and Schubert, G., 2002, *Geodynamics* New York, Cambridge University Press, 456 p.
- Weis, P., 2015, The dynamic interplay between saline fluid flow and rock permeability in magmatic-hydrothermal systems: *Geofluids*, v. 15, no. 1-2, p. 350-371.
- Weis, P., and Driesner, T., 2013, The Interplay of Non-static Permeability and Fluid Flow as a Possible Pre-requisite for Supercritical Geothermal Resources: *Energy Procedia*, v. 40, no. 0, p. 102-106.
- Weis, P., Driesner, T., Coumou, D., and Geiger, S., 2014, Hydrothermal, Multi-phase Convection of H₂O-NaCl Fluids from Ambient to Magmatic Temperatures: A new Numerical Scheme and Benchmarks for Code Comparison: *Geofluids*, p. n/a-n/a.
- Zienkiewicz, O. C., and Taylor, R. L., 2000, *The Finite Element Method - The Basis*, Elsevier Science, Finite Element Method Series.

I Submarine hydrothermal systems

2 Background on submarine hydrothermal circulation

Land-based geothermal systems have been known and utilized since historic times as a heat resource for e.g. bathing and cooking from the indigenous Maori population in New Zealand and for heating on Iceland (Faust and Mercer, 1979c; Lowell, 1991). Hydrothermal hot springs on the seafloor have only been discovered about 35 years ago (see section 2.1.2) and many fundamental questions still remain to be studied.

2.1 Definition of a hydrothermal system & basic process

An active hydrothermal system requires two fundamental components: 1.) a constant supply of water and 2.) a heat source at the base of the system driving the convection of hydrothermal fluids (Lowell, 1991). Heat is typically supplied by a magmatic source but also the regional geothermal gradient or exothermic chemical reactions in the crust, such as the serpentinization of ultramafic rocks might contribute (Lowell and Yao, 2002; Allen and Seyfried Jr, 2004). Permeable pathways like faults and fractures in the host rock are essential in order for water to circulate through the hydrothermal system (Alt, 1995; Wilcock and McNabb, 1996; Becker and Fisher, 2000). The convection of hydrothermal fluids is buoyancy driven. Cold, dense fluids migrate downwards and get progressively warmer as they approach the heat source at depth. Then they become more buoyant and naturally rise back towards the surface (Fig. 2.1).

Hydrothermal activity is closely related to plate tectonics. The majority of active hydrothermal vent fields are found along volcanically active plate boundaries (Hannington et al., 2005; Beaulieu et al., 2013 and Fig. 2.2). They have first been discovered in the late 1970's (see section 2.2.1) and since then intensively been studied at divergent plate boundaries, at the axis of oceanic ridges. At convergent

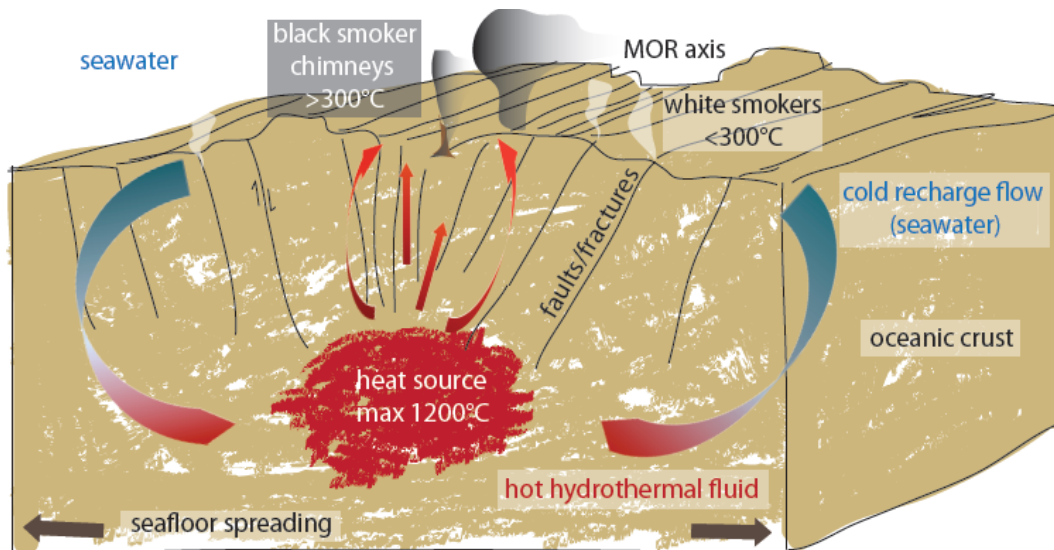


Figure 2.1: Schematic model of a hydrothermal system at an oceanic spreading center. Cold seawater, which is a constant source of fluid required to maintain a hydrothermal circulation cell, migrates down through permeable pathways like faults and fractures in the oceanic crust. While it approaches the driving heat source at depth, the fluid becomes increasingly warmer. A hot fluid is less dense and rises back towards the surface by buoyancy driven flow. During the transport the gradually heated fluid phase becomes increasingly effective in solving minerals and metals out of the crustal rocks. Hydrothermal fluids of varying temperature are enriched in different chemical elements. Hydrothermal fluids hotter than 300°C typically discharge at chimney like structures at the seafloor and have a rich black color (black smokers, see also Fig. 2.4). Colder hydrothermal fluids can be white or even clear (diffuse flow).

plate boundaries hydrothermal activity is found along volcanic arcs or back-arc spreading centers associated with subduction zones as e.g. along the Okinawa Trough in the East China Sea, the Mariana Arc and Back-arc in the western Pacific or along the submarine volcanic arcs and back arc basins related to the subduction zone north of New Zealand (Fig. 2.2). Hydrothermal fields on the seafloor however are also found in intraplate settings that are influenced by hot-spot activity, like e.g. around Hawaii or the Azores. In the following section nature and fundamental characteristics of submarine hydrothermal circulation, with a focus on systems associated with oceanic ridges, will be addressed.

2.2 Hydrothermal activity at oceanic spreading centers

At oceanic ridges, new oceanic lithosphere is produced by the interplay of extensional tectonic as well as extrusive and intrusive igneous processes (Chapter 6). These magmatic processes are considered to provide a major part of the energy required to drive the convection of hydrothermal fluids through the oceanic crust (Alt, 1995; Fornari and Embley, 1995; German and Seyfried Jr, 2014). In marine settings the fluid phase is dominantly derived from seawater, which migrates downwards along fractures and faults below the seafloor (Fig. 2.1). Fluid discharge is typically focused on vertical, chimney-like structures on the seafloor in the axial region of the ridge (Fig. 2.1 and 2.4). Oceanic ridges show very different characteristics depending on spreading velocity (section 6.1), which also influences the circulation of hydrothermal fluids in the crust. Due to the shallow magma lens (section 6.1), which drives hydrothermal convection at fast-spreading ridges, the hydrothermal convection cell only reaches down to a depth of ~2km (Alt, 1995; Hannington et al., 2005). At slow-spreading ridges, where magmatic activity is lower, such a magma lens seems to be absent (section 6.1) and hydrothermal fluids migrate deeper down into the crust (Alt, 1995), which is overall colder and more faulted. Hydrothermal convection cells, consisting of separate recharge and discharge zones (Fig. 2.1) show a lateral extend of several km (Kuehn, 2004). It has been estimated that hydrothermal fluids only need a few years between entering a hydrothermal circulation cell and being discharged from a hydrothermal vent site at the seafloor (Pirajno, 1992).

Baker et al. (1996) already suggested that the relation between spreading rate and magma supply controls the abundance of hydrothermal vent sites along oceanic ridges. Baker and German (2004) confirmed a linear correlation between hydrothermal vents or plume frequency and magmatic budget estimated from the thickness of the crust. Supporting their results they name the high number of known active vent sites along fast-spreading ridges in contrast to slow-spreading

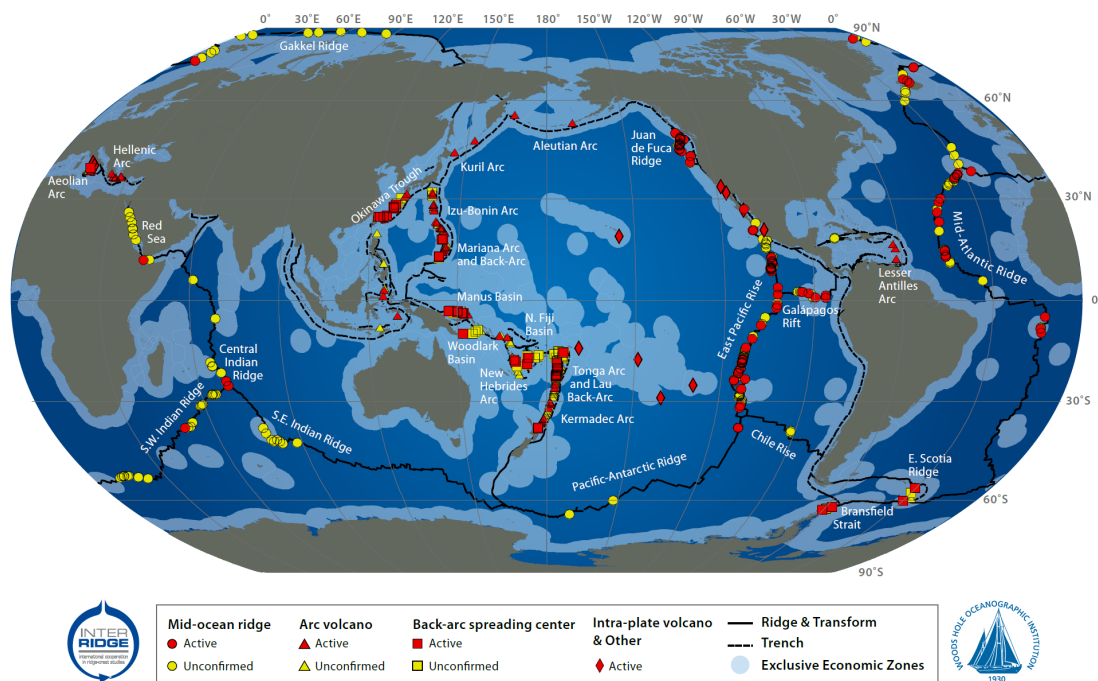


Figure 2.2: Tectonic plate boundaries in marine environments: oceanic ridges at divergent boundaries and trenches related to subduction zones in convergent settings. Also global distribution of hydrothermal vent fields. Source: InterRidge Vents Database Version 2.1. Credits: S. Beaulieu, K. Joyce, J. Cook, and S.A. Soule, Woods Hole Oceanographic Institution, 2015.

settings. If their findings apply to all spreading rates they predict a total number ~1000 active vent sites (~600 are known by now (Beaulieu et al., 2013 and section 2.2.1.2).

Preservation of fossil hydrothermal systems is rare because oceanic crust is constantly consumed at convergent plate boundaries (Hannington et al., 2005 and Fig. 2.2). Nevertheless, remnants of oceanic crust, emplaced on land can be found in form of ophiolites e.g. in Oman, Cyprus or Northwest Spain (Gomez Barreiro et al., 2010). The term *ophiolite* refers to a more or less complete assemblage of mafic to ultramafic rocks from the oceanic crust and upper mantle. Ophiolites are assumed to have originated from extensional back-arc basins and not from Mid-ocean ridges (Hannington et al., 2005).

2.2.1 Discovery of submarine hot springs

The scientific evolution that led to the discovery of submarine hot springs on the seafloor at oceanic ridge crests in the late 1970's has in detail been reviewed by Lowell et al. (1995). The final discovery was made based on a complex interplay of insights reached in various fields of geosciences. The first indication for circulating fluids in the oceanic crust was indirectly coming from calculations of global conductive heat flux through the seafloor in the mid-to end 1960's. The first active submarine hydrothermal vent sites were directly sighted with geophysical methods and deep-diving instruments about a decade later.

2.2.1.1 Early evidence for fluid convection in the oceanic crust

The discovery of submarine hydrothermal activity at the ocean floor might have been delayed by about twenty years due to a peculiar incident: already in 1948 anomalous temperatures and salinities originating from hydrothermal springs in the Red Sea had been monitored during the “Swedish Deep-Sea Expedition” (Pettersson, 1948). Unluckily, at that time this was overlooked because, it is said that geologist G. Arrhenius, was off board to his marriage in Stockholm.

How heat flow studies of the seafloor coupled with models of an aging and cooling oceanic plate created at oceanic ridges (Sclater et al., 1971), led to first speculations about fluids circulating through the oceanic crust is portrayed by Lowell et al. (1995). It became clear that predictions made by conductive heat flow calculations did not fit the data acquired at the seafloor: the heat flow measured close to the ridge axis was always lower than the one expected from the theoretical calculations.

Talwani et al. (1971) were one of the first to suggest that this discrepancy might be caused by circulating seawater in the oceanic crust, which efficiently removes heat by advection. In the following year a detailed study on the thermal

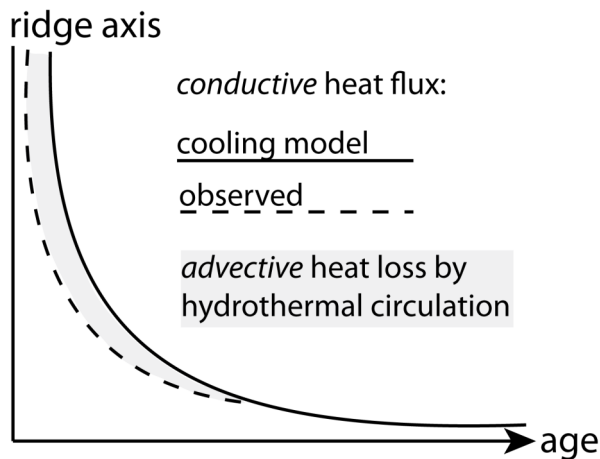


Figure 2.3: Schematic illustration of advective heat flux caused by discharging hydrothermal fluids at the seafloor, derived from anomaly in conductive heat flux data (modified after Stein and Stein, (1994)). Close to the axis of oceanic ridges a negative anomaly occurs in measured conductive heat flux data compared to the flux expected from the lithospheric cooling model for an aging plate. Convecting hydrothermal fluids remove heat from the oceanic crust by advective processes, which is most efficiently in the axial region.

balance of the Juan de Fuca Ridge was published by Lister (1972). It was stated that circulating hydrothermal fluids have much greater influence on the thermal balance of oceanic ridges than conductive cooling processes and that hydrothermal springs were expected to be found at ridge crests.

2.2.1.2 Discovery of the first hydrothermal vent fields on the seafloor

The Red Sea hydrographical anomalies, that randomly had been monitored in 1948 (see section 2.2.1.1 above), were noticed and reinvestigated only much later, in the 1960's, on transit during the International Indian Ocean Expedition (Deacon, 1960, 1964). At that time it was believed that hydrothermal activity was an exceptional feature at that specific locality, linked to an early stage of ocean basin opening (Lowell et al., 1995). Also by chance the TAG hydrothermal field had been discovered in the early 1970's through dredging of low temperature hydrothermal minerals from the seafloor at 26°N on the Mid Atlantic Ridge during the Trans Atlantic Geotraverse project (Rona et al., 1975). Active hydrothermal venting had been confirmed by monitored water temperature anomalies at the same locality (Rona, 1978). Hydrothermal activity was discovered in the same period at the Galapagos Spreading Centre (Weiss et al., 1977) and the East Pacific Rise (EPR) (Larson and Spiess, 1968) by deep-tow sonar technique. Weiss et al. (1977) were able to proof the existence of buoyant hydrothermal plumes at the Galapagos Rift,

hydrothermal vent sites were still not localized. Moreover at the Galapagos Rift a strong helium anomaly, characteristic for hydrothermal brines, was detected during the investigation of hydrothermal plumes (Lupton et al., 1977). The high $^3\text{He}/^4\text{He}$ ratio was explained by circulating hydrothermal fluids which transport ^3He from the mantle to deep ocean water. Based on the combined findings at the Galapagos Rift a research project with a manned deep-diving submersible (*Alvin*) was conducted in February to March 1977 (Corliss et al., 1979). During that cruise low-temperature hydrothermal vent sites (10-17°C) have directly been investigated. A year later Spiess et al. (1980) detected signals from black smokers, high-temperature (~380°C) hydrothermal discharge at the EPR through various geophysical investigations. They also reported zoned sulfide minerals around the black smoker chimneys.

Until today ~600 active hydrothermal vent sites in different tectonic settings have been reported from global systematic explorations (Beaulieu et al., 2013 and Fig. 2.2). Usually such exploration activities start from regional scales and move towards more local investigations. At slow-spreading ridges hydrothermal activity is more difficult to detect than at fast-spreading ones since there is no clearly defined neovolcanic zone and hydrothermal activity is frequently associated with tectonic fault zones in off-axis regions (Baker and German, 2004).

2.2.2 Classification and characteristics of submarine hydrothermal systems

The temperature of hydrothermal fluids discharging on the seafloor is highly varying between 5-407°C (Beaulieu et al., 2013). It is a characteristic parameter for the classification of hydrothermal systems: low-T hydrothermal systems show vent temperatures of <200°C and high-T systems of 200-400°C (Fornari and Embley, 1995). An exceptionally high fluid temperature of 464 °C has been reported from a hydrothermal vent along the southern MAR (Koschinsky et al., 2008). However globally already vent temperatures >400°C are not very common (Beaulieu et al.,

2013).

Low-T systems often show a diffuse style of venting, where clear hydrothermal fluids are exiting at the seafloor with flow rates much lower than at high-T systems (Kelley et al., 2001; Johnson et al., 2010). Circulating hydrothermal fluids with temperatures higher than 50°C are reacting with minerals in the oceanic crust. Between about 100°C and 300°C white „smoke“ discharges at chimneys at the seafloor enriched in ions of white silica, anhydrite and barite (Hannington et al., 1995 and Fig. 2.1). Flow rates are commonly on the order of cm per second (Pirajno, 1992). Moderate temperatures at hydrothermal vent fields provide favorable conditions for diverse biological communities (Grassle, 1985; Martin et al., 2008). At temperatures >300°C hydrothermal fluids give the visual impression of black smoke due to their high strong enrichment in minerals and metals from the crust (Fig. 2.1 and 2.4). Flow rates are usually high, on the order of m per second (Pirajno, 1992). High-T, black smoker hydrothermal activity is frequently associated with sulphide mineral deposits around the discharge site on the seafloor



Figure 2.4: Photomosaic of the black smoker *Barad Dur* from the Logatchev 1 hydrothermal field at the MAR (see also chapter 4). The chimney structure is approximately 5m high. Photographs were taken with the Jason II ROV (WHOI) on the MSM 04/3 cruise on the Maria S. Merian (IOW) in 02/2007. Image by courtesy of Nico Augustin (GEOMAR).

(Herzig, 1999; Cathles, 2011; Hannington et al., 2011). In contact with cold seawater the physio-chemical conditions are changed and the ability of the hydrothermal fluid to carry dissolved metals, its solubility for different elements, changes (Hannington et al., 2005). As a consequence sulfide phases precipitate at the inner chimney wall from high-T hydrothermal fluids (Hannington et al., 1995). Different minerals are precipitated dependent on temperature and chemistry of the fluid. A mineral zonation is often observed at the chimney walls, representing temperatures which decrease from the inside to the outside (Tivey, 1995).

A hydrothermal field on the seafloor commonly consists of several vent sites, which show varying characteristics. The area of hydrothermal vent fields can range from $<100\text{m}^2$ up to 150^3m^2 (Lowell et al., 1995; Hannington et al., 2011). Hydrothermal vent sites often consist of several chimneys that are roughly tens of meters in diameter. A single submarine hydrothermal vent often undergoes phases of varying styles of venting (Pirajno, 1992; Hannington et al., 1995). Diffuse venting and white smoker activity might be the result of mixing with cold seawater (Hannington et al., 1995). The chimneys from which hydrothermal fluids are discharging have growth rates of up to several cm per day. Their heights vary between a few cm to tenths of meters, venting is focused to narrow openings of a few cm in the middle (Lowell et al., 1995). During the average lifetime of a single chimney of 10 years it vents $\sim 3 \times 10^{10}$ kg of fluids (Pirajno, 1992). Chimneys commonly grow on hydrothermal mounds, which consist of chimneys that have collapsed after the phase of active hydrothermal venting. Large sulfide deposits, which can be found on the seafloor, are often composed of several hydrothermal mounds (Hannington et al., 1995).

Hydrothermal systems are reported from a wide range of depths: depth of 2-3 km is common, but systems are also found at shallow depths of only a few meters e.g. in the Mediterranean Sea or close to the coast of volcanic islands. The deepest active vent has been discovered in 2010 at almost 5km deep from the Mid-Cayman Rise in the Caribbean Sea (Connelly et al., 2012).

References Cited

- Allen, D. E., and Seyfried Jr, W. E., 2004, Serpentinization and heat generation: constraints from Lost City and Rainbow hydrothermal systems: *Geochimica et Cosmochimica Acta*, v. 68, no. 6, p. 1347-1354.
- Alt, J. C., 1995, Subseafloor Processes in Mid-Ocean Ridge Hydrothermal Systems, *in* Humphris, S. E., Zierenberg, R. A., Mullineaux, L. S., and Thomson, R. E., eds., *Seafloor Hydrothermal systems - physical, chemical, biological and geological interactions*, Volume 91: Washington DC, American Geophysical Union, p. 1-466.
- Baker, E. T., Chen, Y. J., and Morgan, J. P., 1996, The relationship between near-axis hydrothermal cooling and the spreading rate of mid-ocean ridges: *Earth and Planetary Science Letters*, v. 142, no. 1-2, p. 137-145.
- Baker, E. T., and German, C. R., 2004, On the global distribution of hydrothermal vent fields, *in* German, C. R., Lin, J., and Parson, M., eds., *Mid-Ocean Ridges: Hydrothermal Interactions Between the Lithosphere and Oceans*, Volume Geophysical Monograph Series: Washington, DC, American Geophysical Union, p. 245 - 266.
- Beaulieu, S. E., Baker, E. T., German, C. R., and Maffei, A., 2013, An authoritative global database for active submarine hydrothermal vent fields: *Geochemistry, Geophysics, Geosystems*, v. 14, no. 11, p. 4892-4905.
- Becker, K., and Fisher, A. T., 2000, Permeability of upper oceanic basement on the eastern flank of the Juan de Fuca Ridge determined with drill-string packer experiments: *J. Geophys. Res.*, v. 105, no. B1, p. 897-912.
- Cathles, L., 2011, What processes at mid-ocean ridges tell us about volcanogenic massive sulfide deposits: *Mineralium Deposita*, v. 46, no. 5, p. 639-657.
- Connelly, D. P., Copley, J. T., Murton, B. J., Stansfield, K., Tyler, P. A., German, C. R., Van Dover, C. L., Amon, D., Furlong, M., Grindlay, N., Hayman, N., Huhnerbach, V., Judge, M., Le Bas, T., McPhail, S., Meier, A., Nakamura, K.-i., Nye, V., Pebody, M., Pedersen, R. B., Plouviez, S., Sands, C., Searle, R. C., Stevenson, P., Taws, S., and Wilcox, S., 2012, Hydrothermal vent fields and chemosynthetic biota on the world's deepest seafloor spreading centre: *Nat Commun*, v. 3, p. 620.
- Corliss, J. B., Dymond, J., Gordon, L. I., Edmond, J. M., Herzen, R. P. V., Ballard, R. D., Green, K., Williams, D., Bainbridge, A., Crane, K., and Vanandel, T. H., 1979, Submarine thermal springs on the Galapagos Rift: *Science*, v. 203, no. 4385, p. 1073-1083.
- Deacon, G. E. R., 1960, The Indian Ocean Expedition: *Nature*, v. 187, p. 561-562.
- , 1964, International Indian Ocean Expedition: *Nature*, v. 201, p. 561-562.
- Faust, C. R., and Mercer, J. W., 1979c, A review of numerical simulation of hydrothermal systems: *Hydrological Sciences-Bulletin-des Sciences Hydrologiques*, v. 24, no. 3, p. 335-343.
- Fornari, D. J., and Embley, R. W., 1995, Tectonic and Volcanic Controls on Hydrothermal Processes at the Mid-Ocean Ridge: an overview based on near-bottom and submersible studies, *in* Humphris, S. E., Zierenberg, R. A., Mullineaux, L. S., and Thomson, R. E., eds., *Seafloor Hydrothermal Systems - Physical, chemical, biological and geological interactions*, Volume 91: Washington DC, American Geophysical Union, p. 1-466.
- German, C. R., and Seyfried Jr, W. E., 2014, Hydrothermal Processes, *in* Turekian, H. D. H. K., ed., *Treatise on Geochemistry (Second Edition)*, Volume 8: Oxford, Elsevier, p. 191-233.
- Gomez Barreiro, J., Martinez Catalan, J. R., Prior, D., Wenk, H.-R., Vogel, S., Diaz Garcia, F., Arenas, R., Sanchez Martinez, S., and Lonardelli, I., 2010, Fabric Development in a Middle Devonian Intraoceanic Subduction Regime: The Careo´ n Ophiolite (Northwest Spain): *The Journal of Geology*, v. 118, no. 163-186.

- Grassle, J. F., 1985, Hydrothermal Vent Animals: Distribution and Biology: *Science*, v. 229, no. 4715, p. 713-717.
- Hannington, M., Jamieson, J., Monecke, T., Petersen, S., and Beaulieu, S., 2011, The abundance of seafloor massive sulfide deposits: *Geology*, v. 39, no. 12, p. 1155-1158.
- Hannington, M. D., De Ronde, C. E. J., and Petersen, S., 2005, Sea-Floor Tectonics and Submarine Hydrothermal Systems, *in* Hedenquist, J. W., Thompson, J. F. H., Goldfarb, R. J., and Richards, J. P., eds., *Economic Geology: One Hundredth Anniversary Volume, Volume 1*: Littleton, Colorado, Economic Geology, p. 111-141.
- Hannington, M. D., Jonasson, I. R., Herzig, P. M., and Petersen, S., 1995, Physical and Chemical Processes of Seafloor Mineralization at Mid-Ocean Ridges, *in* Humphris, S. E., Zierenberg, R. A., Mullineaux, L. S., and Thomson, R. E., eds., *Seafloor Hydrothermal Systems - Physical, chemical, biological and geological interactions, Volume 91*: Washington DC, American Geophysical Union, p. 1-466.
- Herzig, P. M., 1999, Economic potential of sea-floor massive sulphide deposits: ancient and modern: *Philosophical Transactions of the Royal Society a-Mathematical Physical and Engineering Sciences*, v. 357, no. 1753, p. 861-873.
- Johnson, H. P., Tivey, M. A., Bjorklund, T. A., and Salmi, M. S., 2010, Hydrothermal circulation within the Endeavour Segment, Juan de Fuca Ridge: *Geochemistry Geophysics Geosystems*, v. 11, no. 5, p. Q05002.
- Kelley, D. S., Delaney, J. R., and Yoerger, D. R., 2001, Geology and venting characteristics of the Mothra hydrothermal field, Endeavour segment, Juan de Fuca Ridge: *Geology*, v. 29, no. 10, p. 959-962.
- Koschinsky, A., Garbe-Schonberg, D., Sander, S., Schmidt, K., Gennerich, H. H., and Strauss, H., 2008, Hydrothermal venting at pressure-temperature conditions above the critical point of seawater, 5 degrees S on the Mid-Atlantic Ridge: *Geology*, v. 36, no. 8, p. 615-618.
- Kuehn, M., 2004, *Reactive Flow Modeling of Hydrothermal Systems*, Berlin Heidelberg, Springer-Verlag, 261 p.:
- Larson, R. L., and Spiess, F. N., 1968, East Pacific Rise Crest: A Near-Bottom Geophysical Profile: *Science*, v. 163, no. 68-71.
- Lister, C. R. B., 1972, On the thermal balance of a Mid-ocean ridge: *Geophysical Journal of the Royal Astronomical Society*, v. 26, no. 5, p. 515-8.
- Lowell, R. P., 1991, Modeling continental and submarine hydrothermal systems: *Reviews of Geophysics*, v. 29, no. 3, p. 457-476.
- Lowell, R. P., Rona, P. A., and Vonherzen, R. P., 1995, Sea-floor hydrothermal systems: *Journal of Geophysical Research-Solid Earth*, v. 100, no. B1, p. 327-352.
- Lowell, R. P., and Yao, Y., 2002, Anhydrite precipitation and the extent of hydrothermal recharge zones at ocean ridge crests: *Journal of Geophysical Research: Solid Earth*, v. 107, no. B9, p. 2183.
- Lupton, J. E., Weiss, R. F., and Craig, H., 1977, Mantle Helium in hydrothermal plumes in Galapagos Rift: *Nature*, v. 267, no. 5612, p. 603-604.
- Martin, W., Baross, J., Kelley, D., and Russell, M., 2008, Hydrothermal vents and the origin of life: *Nat Rev Micro*, v. 6, no. 11, p. 805-814.
- Pettersson, H., 1948, The Swedish Deep-Sea Expedition: *Pacific Science*, v. 2, p. 231-238.
- Pirajno, F., 1992, *Hydrothermal Mineral Deposits - Principles and fundamental concepts for the exploration geologist*, Berlin Heidelberg, Springer-Verlag.
- Rona, P. A., 1978, Near bottom water temperature anomalies: Mid-Atlantic Ridge crest at latitude 26°N: *Geophysical Research Letters*, v. 5, no. 12, p. 993-996.

- Rona, P. A., McGregor, B. A., Betzer, P. R., Bolger, G. W., and Krause, D. C., 1975, Anomalous water temperatures over Mid-Atlantic Ridge crest at 26° North latitude: *Deep Sea Research and Oceanographic Abstracts*, v. 22, no. 9, p. 611-618.
- Slater, J. G., Anderson, R. N., and Lee Bell, M., 1971, Elavation of Ridges and Evolution of the Central Eastern Pacific: *Journal of Geophysical Research*, v. 76, no. 32, p. 7888-7915.
- Spiess, F. N., Macdonald, K. C., Atwater, T., Ballard, R., Carranza, A., Cordoba, D., Cox, C., Diazgarcia, V. M., Francheteau, J., Guerrero, J., Hawkins, J., Haymon, R., Hessler, R., Juteau, T., Kastner, M., Larson, R., Luyendyk, B., Macdougall, J. D., Miller, S., Normark, W., Orcutt, J., and Rangin, C., 1980, East Pacific Rise - Hot springs and geophysical experiments: *Science*, v. 207, no. 4438, p. 1421-1433.
- Stein, C. A., and Stein, S., 1994, Constraints on hydrothermal heat-flux through the oceanic lithosphere from global heat-flow: *Journal of Geophysical Research-Solid Earth*, v. 99, no. B2, p. 3081-3095.
- Talwani, M., Windisch, C. C., and Langseth Jr., M. G., 1971, Reykjanes ridge crest a detailed geophysical study: *Journal of Geophysical Research*, v. 76, no. 2, p. 473-517.
- Tivey, M. A., 1995, Modeling Chimney Growth and Associated Fluid Flow at Seafloor Hydrothermal Vent Sites, *Seafloor Hydrothermal Systems: Physical, Chemical, Biological, and Geological Interactions*, American Geophysical Union, p. 158-177.
- Weiss, R. F., Lonsdale, P., Lupton, J. E., Bainbridge, A. E., and Craig, H., 1977, Hydrothermal plumes in Galapagos Rift: *Nature*, v. 267, no. 5612, p. 600-603.
- Wilcock, W. S. D., and McNabb, A., 1996, Estimates of crustal permeability on the endeavour segment of the Juan de Fuca mid-ocean ridge: *Earth and Planetary Science Letters*, v. 138, no. 1-4, p. 83-91.

3 Numerical simulation of hydrothermal circulation

One of the first approaches to numerically simulate hydrothermal flow in a geothermal system on land was around 1960 (see section 3.1 below). Until today our knowledge of key parameters of hydrothermal processes, as e.g. fluids properties have become more detailed and precise. Computational efficiency has increased significantly and numerical methods have been improved, such that more complex, less simplified hydrothermal convection models can be designed.

3.1 Development of hydrothermal convection models

Reviews by Lowell (1991) and Ingebritsen et al. (2010) give a detailed overview on the evolution of numerical simulations of hydrothermal systems since the middle of the last century. Two basic types of models simulating fluid flow in hydrothermal systems were described by Lowell (1991): „pipe models” and „porous flow models“. In pipe models a hydrothermal convection cell is divided into simplified recharge, discharge and heating zones. The heterogeneous permeability distribution forces fluid flow to these distinct zones. In early, simple pipe models temperature and velocity fields were not solved in detail but they could effectively describe e.g. warm springs on Iceland (Einarrson, 1942 and Bodvarsson, 1950 in Lowell, 1991). Porous flow models simulate the circulation of hydrothermal fluids driven by convective instabilities in a fluid-saturated porous layer which is heated from below. In an early porous flow models for hydrothermal circulation, finite differences were applied to solve for heat transport and fluid flow e.g. in order to investigate the onset of thermal convection in the Wairakei geothermal field in the Taupo Volcanic Zone in New Zealand (Wooding, 1957; Donaldson, 1962; Ingebritsen et al., 2010). Further numerical models were developed during exploitation of the Wairakei geothermal reservoir. So called „lumped parameter models“ did not

consider a heterogeneous distribution of mass and energy in the convection cell, but were restricted to total values crossing the boundaries of the modeled system (Whiting and Ramey, 1969). They offered a simple way of describing the behavior of a geothermal reservoir during exploitation (Faust and Mercer, 1979c). In 1975 different research groups presented the first more advanced porous convection models for both liquid and vapour-dominated hydrothermal reservoirs in which the properties of the rock and the fluid were allowed to vary in space (Faust and Mercer, 1979c). In 1979 Faust and Mercer published mathematical models and numerical solution techniques for 3D multiphase hydrothermal flow in porous media using a pressure-enthalpy formulation. They compared finite difference and finite element approaches and also applied their modelling approach to the Wairakei geothermal reservoir (Faust and Mercer, 1979b, a, c).

Until today porous convection models for the circulation of fluids in hydrothermal systems have developed into high complexity and diversity. See also porous flow model applied in this work to study the convection of fluids in the oceanic crust (see Chapter 4 and 5). Combinations of finite volumes (FV) and finite elements appear to be good implementation techniques (Geiger et al., 2004; Weis et al., 2014). FV schemes are strictly mass conserving and thus good for resolving mass and energy transport while FE methods are well suited for resolving the fluid pressure field (Huber and Helmig, 1999; Driesner and Geiger, 2007a). Simulation of submarine hydrothermal convection in three dimensions has been optimized (Coumou et al., 2009a; Hasenclever et al., 2014). Today the physics of sub- and supercritical phase separation of saline fluids are well understood e.g. (Bischoff and Rosenbauer, 1984). The physical processes have been studied for hydrothermal systems in the field (Cowan and Cann, 1988; Von Damm et al., 2003) and by multiphase numerical modeling approaches (Driesner and Geiger, 2007a; Coumou et al., 2009b; Weis et al., 2014). The thermodynamic properties of pure water and saltwater (H₂O-NaCl) differ (e.g. Cowan and Cann, 1988; Driesner, 2007; Driesner and Heinrich, 2007; Coumou et al., 2009b). The NaCl component in

saltwater adds complexity to the thermodynamic system. The critical point of saltwater (407°C and 298 bar) is not a critical endpoint for phase separation as it is in the case of pure water. Saline fluids rather move between two supercritical endmembers of a liquid-like and a vapor-like phase (e.g. Bischoff and Rosenbauer, 1984; Cowan and Cann, 1988; Driesner and Heinrich, 2007).

3.2 2D hydrothermal flow model applied in this work

Hydrothermal fluid flow in the oceanic crust is simulated by applying a coupled set of non-linear equations for pressure and temperature (equations. 3.8 and 3.9). Parts of this section (3.2), describing the hydrothermal flow model have been published as supplement* to the Geology paper (Chapter 4, Andersen et al., 2015).

3.2.1 Governing equations

3.2.1.1 Darcy's Law of fluid flow

The convecting fluid is assumed to be pure water flowing through a rigid porous material. Subscript-indices f and r are used to refer to fluid and rock properties, respectively. Fluid flow through a porous medium is described by Darcy's law:

$$\bar{v} = -\frac{k}{\mu_f}(\nabla P - \rho_f \bar{g}) \quad (3.1)$$

which links fluid flow expressed as Darcy velocity \bar{v} to the forces causing it on the right hand side (rhs), where k is the permeability of the rock, μ_f the fluid's dynamic viscosity, ρ_f fluid density, pressure ∇P divergence and g the gravitational acceleration vector. The minus sign of the rhs term is due to the fact that fluids naturally flow from high to low pressure. Only pressure gradients in excess of the hydrostatic pressure (= pressure on a fluid at rest caused by the weight of fluid or

*GSA Data Repository item 2015032; doi:10.1130/G36113.1, available online at www.geosociety.org/pubs/ft2015.htm

other material above it) cause fluids to flow. The pressure gradient is influenced by gravity, which is non-zero for the vertical direction. Fluid flow is focused to pores in the rock and darcy velocity v can be scaled down to pore scale fluid velocity u_f by dividing it by porosity φ :

$$u_f = v/\varphi.$$

3.2.1.2 Conservation of mass and energy

Fluid mass transport in a porous medium is mathematically defined by the product of Darcy velocity and fluid density. We assume a control volume (Fig. 3.1) with porosity φ , permeability k and a fluid with density ρ_f . The amount of fluid mass inside the volume can be expressed as the difference between the mass flux entering and leaving it:

$$q_{in} - q_{out} = \text{amount of mass inside the volume}, \quad (3.2)$$

providing a simple mass balance. If the incoming mass flux is higher than the outgoing one the amount of fluid mass inside the volume increases and vice versa. Pores are assumed to have a constant size and to always be filled. An increase in total fluid mass inside the control volume thus has to be compensated by an increase in fluid density, such that the fluids are compressed. Mass flux q through a side of the rectangular control volume (Fig. 3.1) is expressed as:

$$q = (\rho_f v \varphi) \Delta y \Delta z \quad (3.3)$$

Fluid mass flux q_{out} leaving the volume can be described as the flux that enters the volume plus the change of that flux over the length Δx of the volume:

$$q_{out} = q_{in} + \frac{\partial q_{in}}{\partial x} \Delta x \quad (3.4)$$

If the expression for outgoing mass flux described by equation 3.4 is substituted into the simple mass balance equation 3.2, in combination with equation 3.3 we obtain:

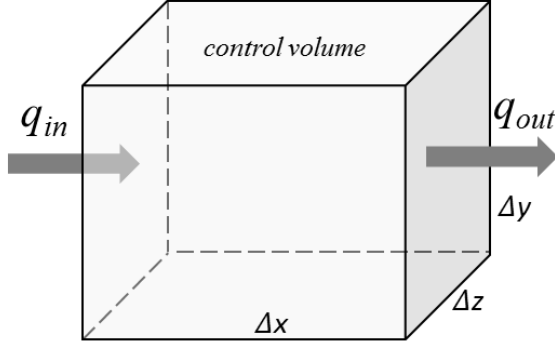


Figure 3.1: Schematic illustration of control volume for which mass conservation is derived. A hydrothermal fluid with density ρ_f and viscosity μ_f is assumed to enter the volume - a porous medium with porosity ϕ and permeability k - through the left side and exit at the opposite. q denotes fluid mass fluxes as in Equ. 3.3.

$$\frac{\partial(\rho_f v \phi)}{\partial t} \Delta x \Delta y \Delta z = (\rho_f v \phi) \Delta y \Delta z - \left((\rho_f v \phi) \Delta y \Delta z + \frac{\partial(\rho_f v \phi) \Delta y \Delta z}{\partial x} \right) \quad (3.5)$$

The above equation describes the change in the amount of fluid mass inside the control volume in time. It can be simplified to:

$$\phi \frac{\partial \rho_f}{\partial t} = -\nabla \cdot (\bar{v} \rho_f) \quad (3.6)$$

which is the final mass conservation equation for fluid flow in porous media. Substituting equation 3.1 for darcy velocity v into equation 3.6 and noting that the fluid's density is a function of temperature and pressure P , yields the pressure equation:

$$\phi \rho_f \left(\beta_f \frac{\partial P}{\partial t} - \alpha_f \frac{\partial T}{\partial t} \right) = \nabla \cdot \left(\rho_f \frac{k}{\mu_f} (\nabla P - \rho_f \bar{g}) \right) \quad (3.7)$$

where α_f and β_f are the fluid's thermal expansivity and compressibility respectively. Hydrostatic pressure in all our model applications, e.g. at the Logatchev 1 hydrothermal field (-30 MPa) (Chapter 4), is above the critical endpoint of pure water (22.1 MPa) so that the fluid will always be in the (supercritical) single-phase

region. This allows us to formulate energy conservation as a function of temperature:

$$\left(\phi\rho_f c p_f + (1-\phi)\rho_r c p_r\right) \frac{\partial T}{\partial t} = \nabla \cdot (\kappa \nabla T) - \rho_f c p_f \vec{v} \cdot \nabla T + \frac{\mu_f}{k} \vec{v}^2 - \left(\frac{\partial \ln \rho}{\partial \ln T}\right)_p \frac{DP}{Dt} \quad (3.8)$$

Fluid and rock are assumed to be in local thermal equilibrium (i.e. $T = T_f = T_r$) so that the mixture appears on the left hand side (lhs) of equation 3.8. Changes in temperature depend on heat conduction (1st term on rhs, see also section 1.3.2, Equ. 1.3), heat advection by fluid flow (2nd term), heat generation by internal friction of the fluid (3rd term; viscous dissipation; e.g. (Magyari et al., 2005 p. 374)), and pressure-volume work including dependence of enthalpy (h) on pressure (4th term, (Bird et al., 2007 p. 337)).

All fluid properties ($\alpha_f, \beta_f, \rho_f, \mu_f, c p_f$) are functions of both pressure and temperature (see examples Fig. 3.2) and are evaluated from pre-calculated look-up tables based on the IAPS-84 formulation of water and steam properties. The tables have been computed using the program PROST 4.1 (PROPERTIES of water and STEAM developed by Bauer (1998)), which is available at: http://fluidos.etsii.upm.es/faculty/Jaime_Carpio/Fumatas_negas/PROST%20Properties%20of%20Water%20and%20Steam.htm. The high water depth along the modeled transect in chapter 4 causes a high hydrostatic pressure, which ensures that pure water remains at supercritical pressure-temperature (P - T) conditions so that two-phase phenomena do not need to be accounted for in our model. This is also respected in all other model applications (Chapter 5).

3.2.2 Numerical formulation and solution techniques

We use 3-node triangular elements that form unstructured meshes. In the case study of the Logatchev hydrothermal field (LHF) (Chapter 4) the model domain consists of ~90k to 570k elements depending on the modeled fault width, which corresponds to elements sizes between 0.4 m² and 40 m² inside the permeable fault.

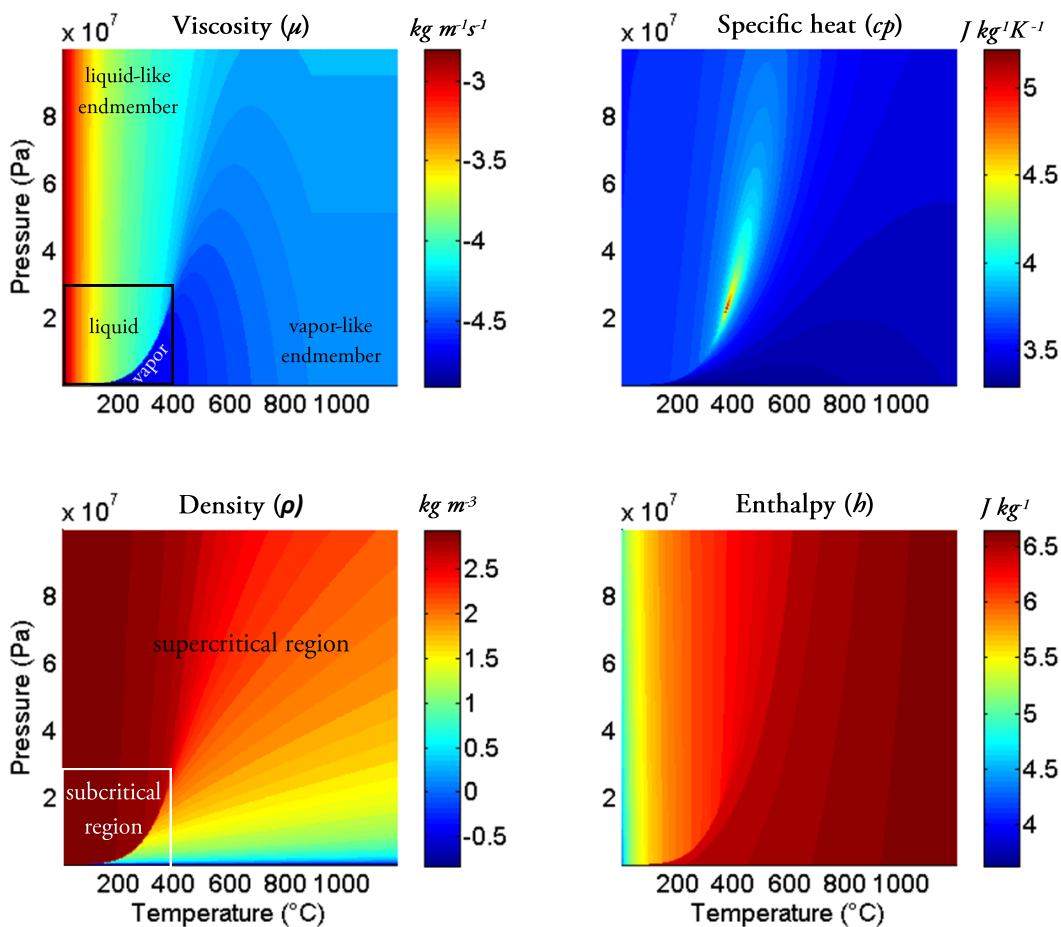


Figure 3.2: Pressure and temperature dependent fluid properties of pure water as well as fluid enthalpy (all in log scale). The boiling curve for water is visible as a sharp contrast in density and viscosity as well as fluid enthalpy at temperatures below 400°C and pressures of below 3×10^7 Pascal, which roughly corresponds with the critical endpoint for subcritical phase transitions (boiling or condensation). Above that point water is in a supercritical state, where transitions between a liquid-like and a vapor-like phase occur gradually. Hot fluids ($>400^\circ\text{C}$) in a vapor or vapor-like phase have the highest enthalpy and are thus transporting most energy during hydrothermal convection. Due to the inherent fluid properties of water, buoyancy-driven energy transport of a hydrothermal fluid is optimized at a $\sim 400^\circ\text{C}$ (maximum fluxibility, Jupp and Schultz, (2000)), where both density and viscosity are low, which allows the fluid to easily move (see also section 4.4 and chapter 5).

We solve the equations for velocity 3.1, pressure 3.7, and temperature 3.8 separately. Using an implicit Finite Element Method we solve equation 3.7 to derive the pressure field and subsequently 3.1 to obtain Darcy velocities. Equation

3.8 is solved by operator splitting: The advection term is treated by a semi-Lagrange scheme with 2nd-order accurate Predictor-Corrector integration along flow trajectories and a cubic interpolation scheme on the unstructured meshes. The diffusion part of the energy equation is also solved using an implicit FEM. This algorithm has been implemented into a modified version of the MATLAB code MILAMIN (Dabrowski et al., 2008). All matrix equations are solved using the Cholesky direct solver of the numerical library SuiteSparse (Davis and Hager, 2009) (<http://www.cise.ufl.edu/research/sparse/SuiteSparse/>).

3.2.3 Boundary conditions

At outer margins of any numerical domain it is necessary to set specific conditions. All $\partial T / \partial z = 0$ domain boundaries during our hydrothermal flow simulations are impermeable except the top boundary, through which the fluid is allowed to enter and leave the domain. All side boundaries are insulating. At the top boundary we use mixed boundary conditions: Temperature is set to 4°C seawater temperature where fluid enters the domain, and at discharge nodes the vertical temperature gradient is set to zero to mimic free venting conditions. At the bottom boundary either a Neumann condition where boundary nodes are given fixed values for temperature or a Dirichlet condition is applied where the heat flux entering the model domain is kept constant. In the model set-up of the LHF (section 4.3) a Dirichlet boundary condition is used with a Gaussian-shaped heat flux profile simulating the driving heat source at the base of the model domain:

$$Hf(x) = Hf_{tot} \exp\left(-\frac{(x-x_0)^2}{2\sigma^2}\right), \quad (3.9)$$

where x_0 denotes the center of the heat source at $x_0=6500\text{m}$. Hf_{tot} is chosen such that the integrated heat-input along the transect is 12.5 kW per meter ridge axis — a reasonable value for the Mid-Atlantic Ridge (Sinha et al., 2004). The width of the

heat source, controlled by the half-width of the Gaussian curve, $\sigma=1.25$ km, was chosen based on the approximate lateral extent of the zone of enhanced seismicity in Figure 1. All hydrothermal flow calculations began with cold hydrostatic conditions and were ran into thermal steady-state, at which all mass and energy fluxes were balanced and the thermal energy inside the box remained constant.

References Cited

- Andersen, C., Rüpke, L., Hasenclever, J., Grevemeyer, I., and Petersen, S., 2015, Fault geometry and permeability contrast control vent temperatures at the Logatchev 1 hydrothermal field, Mid-Atlantic Ridge: *Geology*, v. 43, no. 1, p. 51-54.
- Bauer, O., 1998, Prost 4.1 PROPERTIES of water and STEAM: TU Hamburg Harburg.
- Bird, R. B., Stewart, W. E., and Lightfoot, E. N., 2007, *Transport Phenomena*, John Wiley & Sons.
- Bischoff, J. L., and Rosenbauer, R. J., 1984, The critical point and two-phase boundary of seawater, 200-500°C: *Earth and Planetary Science Letters*, v. 68, no. 1, p. 172-180.
- Coumou, D., Driesner, T., Geiger, S., Paluszny, A., and Heinrich, C. A., 2009a, High-resolution three-dimensional simulations of mid-ocean ridge hydrothermal systems: *Journal of Geophysical Research-Solid Earth*, v. 114.
- Coumou, D., Driesner, T., Weis, P., and Heinrich, C. A., 2009b, Phase separation, brine formation, and salinity variation at Black Smoker hydrothermal systems: *Journal of Geophysical Research-Solid Earth*, v. 114, p. 16.
- Cowan, J., and Cann, J., 1988, Supercritical two-phase separation of hydrothermal fluids in the Troodos ophiolite: *Nature*, v. 333, no. 6170, p. 259-261.
- Dabrowski, M., Krotkiewski, M., and Schmid, D. W., 2008, MILAMIN: MATLAB-based finite element method solver for large problems: *Geochemistry Geophysics Geosystems*, v. 9.
- Davis, T. A., and Hager, W. W., 2009, Dynamic Supernodes in Sparse Cholesky Update/Downdate and Triangular Solves: *Acm Transactions on Mathematical Software*, v. 35, no. 4.
- Donaldson, I. G., 1962, Temperature gradients in the upper layers of the Earth's crust due to convective water flows: *Journal of Geophysical Research*, v. 67, no. 9, p. 3449-3459.
- Driesner, T., 2007, The system H₂O-NaCl. Part II: Correlations for molar volume, enthalpy, and isobaric heat capacity from 0 to 1000 degrees C, 1 to 5000 bar, and 0 to 1 X-NaCl: *Geochimica et Cosmochimica Acta*, v. 71, no. 20, p. 4902-4919.
- Driesner, T., and Geiger, S., 2007a, Numerical simulation of multiphase fluid flow in hydrothermal systems, *in* Liebscher, A., and Heinrich, C. A., eds., *Fluid-Fluid Interactions*, Volume 65, p. 187-212.
- Driesner, T., and Heinrich, C. A., 2007, The system H₂O-NaCl. Part I: Correlation formulae for phase relations in temperature-pressure-composition space from 0 to 1000 degrees C, 0 to 5000 bar, and 0 to 1 X-NaCl: *Geochimica et Cosmochimica Acta*, v. 71, no. 20, p. 4880-4901.
- Faust, C. R., and Mercer, J. W., 1979a, Geothermal reservoir simulation 1: Mathematical models for liquid-dominated and vapor-dominated hydrothermal systems: *Water Resources Research*, v. 15, no. 1, p. 23-30.

- , 1979b, Geothermal reservoir simulation 2: Numerical solution techniques for liquid-dominated and vapor-dominated hydrothermal systems: *Water Resources Research*, v. 15, no. 1, p. 31-46.
- , 1979c, A review of numerical simulation of hydrothermal systems: *Hydrological Sciences-Bulletin-des Sciences Hydrologiques*, v. 24, no. 3, p. 335-343.
- Geiger, S., Robert, S., Matthai, S. K., Zoppou, C., and Burri, A., 2004, Combining finite element and finite volume methods for efficient multiphase flow simulations in highly heterogeneous and structurally complex geologic media: *Geofluids*, v. 4, no. 4, p. 284-299.
- Hasenclever, J., Theissen-Krah, S., Rupke, L. H., Morgan, J. P., Iyer, K., Petersen, S., and Devey, C. W., 2014, Hybrid shallow on-axis and deep off-axis hydrothermal circulation at fast-spreading ridges: *Nature*, v. 508, no. 7497, p. 508-512.
- Huber, R., and Helmig, R., 1999, Multiphase flow in heterogeneous porous media: A classical finite element method versus an implicit pressure explicit saturation-based mixed finite element finite volume approach: *International Journal for Numerical Methods in Fluids*, v. 29, no. 8, p. 899-920.
- Ingebritsen, S. E., Geiger, S., Hurwitz, S., and Driesner, T., 2010, Numerical simulation of magmatic hydrothermal systems: *Reviews of Geophysics*, v. 47.
- Jupp, T., and Schultz, A., 2000, A thermodynamic explanation for black smoker temperatures: *Nature*, v. 403, no. 6772, p. 880-883.
- Lowell, R. P., 1991, Modeling continental and submarine hydrothermal systems: *Reviews of Geophysics*, v. 29, no. 3, p. 457-476.
- Magyari, E., Rees, D. A. S., and Keller, B., 2005, Effect of viscous dissipation on the flow in fluid saturated porous media, *in* Vafai, K., ed., *Handbook of porous media*: Boca Raton, Taylor & Francis Group, p. 374-406.
- Sinha, M. C., Evans, R. L., German, C., Lin, J., and Parson, L., 2004, Mid-Ocean Ridges: Hydrothermal Interactions Between the Lithosphere and Oceans, p. 19-62.
- Von Damm, K. L., Lilley, M. D., Shanks Iii, W. C., Brockington, M., Bray, A. M., O'Grady, K. M., Olson, E., Graham, A., and Proskurowski, G., 2003, Extraordinary phase separation and segregation in vent fluids from the southern East Pacific Rise: *Earth and Planetary Science Letters*, v. 206, no. 3-4, p. 365-378.
- Weis, P., Driesner, T., Coumou, D., and Geiger, S., 2014, Hydrothermal, Multi-phase Convection of H₂O-NaCl Fluids from Ambient to Magmatic Temperatures: A new Numerical Scheme and Benchmarks for Code Comparison: *Geofluids*, p. n/a-n/a.
- Whiting, R. L., and Ramey, H. J., Jr., 1969, Application of Material and Energy Balances to Geothermal Steam Production: *Journal of Petroleum Technology*, v. 21, no. 7.
- Wooding, R. A., 1957, Steady state free thermal convection of liquid in a saturated permeable medium: *Journal of Fluid Mechanics*, v. 2, p. 273-285.

4 Fault geometry & permeability contrast control vent temperatures at the Logatchev 1 hydrothermal field, Mid-Atlantic Ridge

Christine Andersen, Lars Rüpke, Jörg Hasenclever, Ingo Grevemeyer, and Sven Petersen*
GEOMAR, Helmholtz Centre for Ocean Research, Wischhofstrasse 1-3, 24148 Kiel, Germany

Abstract

High-temperature (>300 °C) off-axis hydrothermal systems found along the slow-spreading Mid-Atlantic Ridge are apparently always located at outcropping fault zones. While preferential flow of hot fluids along highly permeable, fractured rocks seems intuitive, such efficient flow inevitably leads to the entrainment of cold ambient seawater. The temperature drop this should cause is difficult to reconcile with the observed high-temperature black smoker activity and formation of associated massive sulfide ore deposits. Here we combine newly acquired seismological data from the high-temperature, off-axis Logatchev 1 hydrothermal field (LHF1) with numerical modeling of hydrothermal flow to solve this apparent contradiction. The data show intense off-axis seismicity with focal mechanisms suggesting a fault zone dipping from LHF1 toward the ridge axis. Our simulations predict high-temperature venting at LHF1 only for a limited range of fault widths and permeability contrasts, expressed as the fault's relative transmissibility (the product of the two parameters). The relative transmissibility must be sufficient to "capture" a rising hydrothermal plume and redirect it toward LHF1 but low enough to prevent extensive mixing with ambient cold fluids. Furthermore, the temperature drop associated with any high permeability zone in heterogeneous crust may explain why a significant part of hydrothermal discharge along slow-spreading ridges occurs at low temperatures.

*Paper published in *Geology* 01/2015: doi: 10.1130/G36113.1

4.1 Introduction

High-temperature hydrothermal systems at slow-spreading ridges are often linked to fault zones that cut the seafloor several kilometers off-axis (McCaig et al., 2007). Extensional deformation increases permeability and makes fault zones the preferred pathways for hydrothermal fluids. The Mid-Atlantic Ridge (MAR) black-smoker vent fields TAG (Trans-Atlantic Geotraverse; deMartin et al., 2007), Logatchev (Petersen et al., 2009), and Petersburg (Shilov et al., 2012) are all located at such faults that outcrop up to 16 km away from the ridge axis. Fault-related vent fields are active over longer periods of time than ridge-centered hydrothermal systems at fast-spreading ridges (50–100 k.y. versus 100–1000 yr; Jamieson et al., 2014). As a consequence of this longevity, fault-controlled submarine massive sulfide deposits at slow spreading ridges tend to be larger than their on-axis counterparts at fast-spreading ridges (Fouquet, 1997). Fluids feeding these systems must be hot enough ($>300\text{ }^{\circ}\text{C}$) to transport metals from the crust to the seafloor (Hannington et al., 2011). If fault zones were isolated conduits, hot hydrothermal fluids could easily flow through them without significant cooling. However, fault zones are open systems and, depending on their geometry and fluid-dynamic properties, significant mixing between hot hydrothermal fluids and colder ambient fluids occurs. Therefore, the fundamental dilemma in high-temperature fault-controlled hydrothermal systems is that a certain permeability contrast is required to provide a preferred fluid pathway but that mixing with colder ambient fluids should result in a significant reduction in temperature.

These processes can be excellently studied at the fault-controlled Logatchev 1 hydrothermal field (LHF1), which is located on a segment of the MAR undergoing tectonic extension and core-complex formation. Here we combine new seismological data with numerical modeling of hydrothermal flow to elucidate the hydrological regime beneath LHF1 and to show under which conditions fluid flow along fault zones can be reconciled with the observed high vent temperatures.

4.2 The Logatchev 1 hydrothermal field

The LHF1 is located 8 km off-axis at 14.75°N on the MAR (Fig. 4.1a). High-temperature discharge has been stable at ~300–350 °C for the past decade (Schmidt et al., 2007). Evidence for detachment faulting and core complex formation is manifested in outcropping serpentinitized ultramafics and gabbroic rocks, in surface structures (Petersen et al., 2009) as well as in off-axis seismic activity. New seismological data were acquired during two deployments in 2009 (Fig. 4.1 and Grevemeyer et al., 2013) and indicate that deformation is concentrated along the eastern rift mountains in the vicinity of LHF1. Hypocenters of normal faulting earthquakes roughly line-up with the outcrop of a fault zone near LHF1 (Fig. 4.1b) and are likely to mark the subsurface continuation of the fault zone. This fractured, more permeable region could be the preferred pathway for hydrothermal fluids feeding the LHF1 vent system, and the diffuse seismicity pattern surrounding the normal faulting earthquakes may reflect thermal stresses caused by this hydrothermal circulation. The absence of earthquakes at depths >5 km below seafloor (i.e., >9 km bsl; Fig. 4.1b) suggests that temperatures there are too high for brittle failure (>600 °C) indicating a high geothermal gradient and possibly the presence of an intrusion providing heat to drive the hydrothermal convection.

4.3 Modeling framework and setup

Based on the geophysical data discussed above, we constructed a two-dimensional (2-D) numerical model for hydrothermal flow along the 8 km long transect shown in figure 4.1. The numerical mesh follows the observed bathymetry and includes the seismically imaged fault zone. Because the precise width of the fault zone cannot be inferred from the seismic data., we have conducted calculations with width, d , of the fault zone varying between 1 m and 2 km to cover the range from a narrow permeable fault zone to a much wider deformation zone containing multiple faults. In addition, we have varied the fault zone's permeability, k_f , to obtain different

permeability contrasts ($c = k_d/k_b$, = 3, 10, 30, and 100) with respect to a background permeability $k_b = 5 \times 10^{-16} \text{ m}^2$. This constant background permeability was chosen such that a homogenous model without fault zone predicts both high-temperature venting as well as magmatic temperatures at depth for a reasonable heat input. The heat source is simulated by a Gaussian-shaped profile and an integrated heat input of 12.5 kW per meter ridge axis, an average value for the MAR (Sinha and Evans, 2004). The heat source is assumed to lie beneath an off-axis volcano marked by a cluster of micro-earthquakes at transect kilometer 6.5, which is ~ 2 km to the west of LHF1 (Fig. 4.1b). See table 4.1 for rock properties and other model parameters.

The governing equations for convection of supercritical

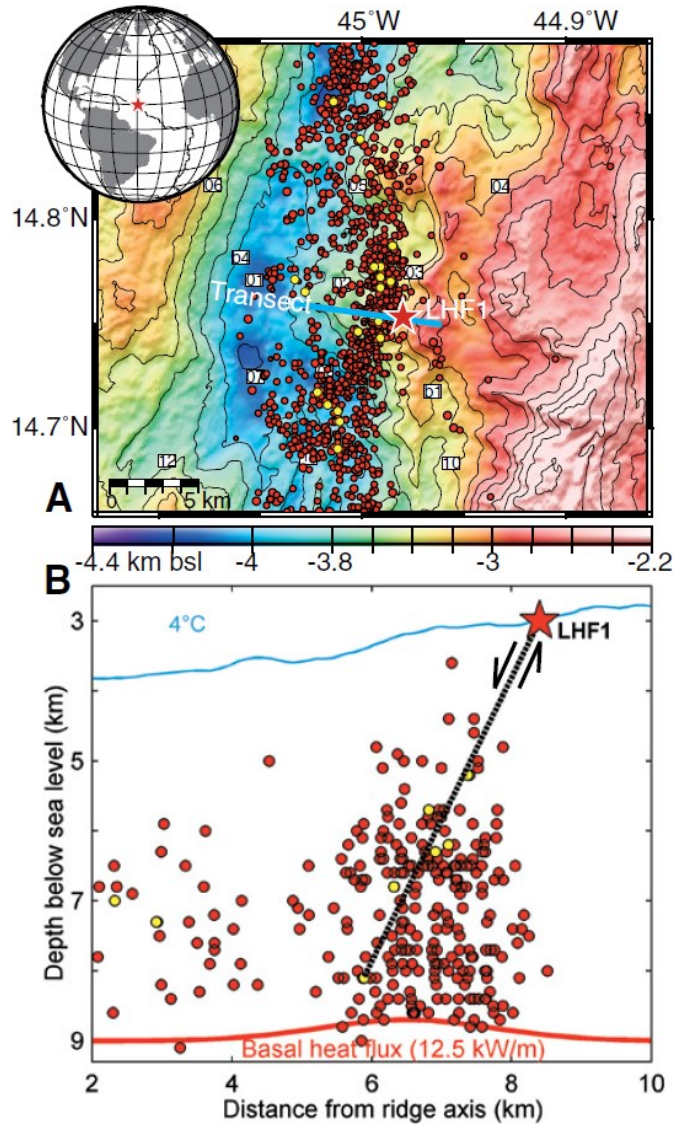


Figure 4.1. A: Seafloor bathymetry around the off-axis Logatchev 1 hydrothermal field (red star, LHF1) and observed seismicity (red dots, first published by Grevenmeyer et al., 2013). Our numerical model is oriented along transect shown in blue. bsl—below sea level. B: Normal faulting earthquakes (yellow dots) roughly line up along fault zone dipping from LHF1 toward ridge axis. Locations of oceanbottom seismometers are labeled b1, b2, and b4 (broadband) and 01–12 (short-period).

pure-water, taking into account the thermodynamic properties of water, are solved on an unstructured triangular mesh using the Finite Element method (see the GSA Data Repository¹ and Hasenclever et al., 2014 for details). All simulations were run until steady-state temperature fields evolved and hydrothermal heat flow at the seafloor was equal to magmatic heat input.

Parameter	Value	Unit
Half width heat source, σ	1.25	km
Fault width, d	1–2000	m
Rock properties		
Density	2750	kg m ⁻³
Porosity	10	%
Conductivity	2	W m ⁻¹ K ⁻¹
Specific heat	880	J kg ⁻¹ K ⁻¹
Background permeability*, k_b	0.5x, 1x, 2x10 ⁻¹⁵	m ²
Permeability contrast, $c = k_f/k_b$	3, 10, 30, 100	
Fluid properties		
Thermodynamic tables for pure water [†]		

Table 4.1: Applied model parameters.

Note: k_f is fault permeability, k_b is background permeability.

* $k_b = 0.5 \times 10^{-15} \text{ m}^2$ was used in simulations described in the main text; the others apply to simulations in the Data Repository¹ and to simulations in chapter 5 of this thesis.

[†]Fluid properties are evaluated from look-up tables computed using the program PROST 4.1 (Properties of water and Steam) based on the IAPS-84 formulation developed by Bauer (1998); see the Data Repository¹ for details.

4.4 Simulation results

Figure 4.2 shows the three different regimes of hydrothermal convection that we identified in our 66 model calculations. In figure 4.2, the fault has a $10 \times$ higher permeability compared to the surrounding crust and only its width is varied. When the fault width is small ($d = 10\text{m}$; Fig. 4.2a) the rising hydrothermal plume is not captured so that high temperature venting occurs above the heat source rather than at the location of LHF1. When the fault width is increased to 30 m (Fig. 4.2b), the plume is deflected into the fault zone and high-temperature venting ($\sim 330^\circ\text{C}$) is predicted at the location of LHF1. Increasing the fault width even further (150m; Fig. 4.2c) leads to strongly enhanced upward mass flux within the fault combined

¹GSA Data Repository item 2015032; doi:10.1130/G36113.1, available online at www.geosociety.org/pubs/ft2015.htm

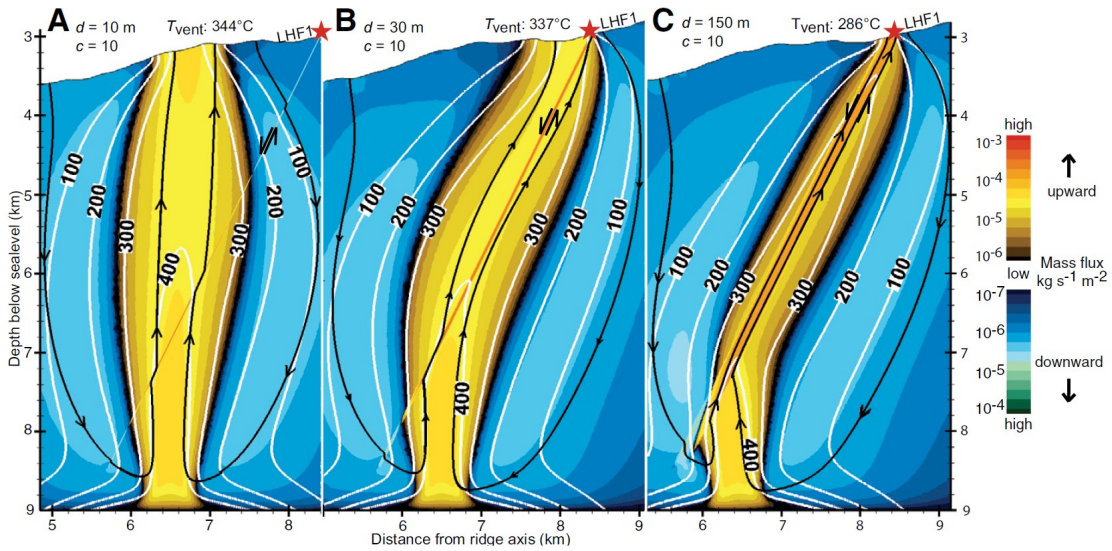


Figure 4.2: Three example calculations with constant fault ($k_f = 5 \times 10^{-15} \text{ m}^2$) to background ($k_b = 0.5 \times 10^{-15} \text{ m}^2$) permeability contrast $c = k_f/k_b = 10$. We only varied fault width (d). Isotherms for 100, 200, and 300°C in white. Black flow lines show pattern of convecting hydrothermal fluids. **A:** Fault width 10m. Rising plume is almost unaffected and high-temperature venting ($>340^\circ\text{C}$) occurs vertically above heat source. **B:** Fault width 30m. Rising plume is redirected, and high-temperature venting occurs at location of Logatchev 1 hydrothermal field (LHF1). The increase in mass flux inside the fault zone leads to the lower vent temperature compared to A. **C:** Fault width 150m. Further increasing fault width leads to significant increase in mass flux that causes entrainment of ambient colder fluids. As a consequence, maximum vent temperature at fault tip is strongly reduced.

with a significant decrease in vent temperature to $\sim 285^\circ\text{C}$, in disagreement with measured vent fluid exit temperatures at LHF1 ($\sim 350^\circ\text{C}$; Schmidt et al., 2007).

We have systematically varied fault width and permeability contrast in our model calculations and find similar trends for each permeability contrast (Fig. 4.3). When the fault is very narrow, vent temperatures are as high as observed but venting occurs above the heat source rather than at LHF1 (open symbols in figures 4.3a and 4.3b). For wider fault zones, the hydrothermal plume is redirected toward LHF1 but vent temperatures are gradually reduced (filled symbols in figures 3a and b). We have also tested varying background permeabilities (see additional 32 simulations in the GSA Data Repository¹ and Chapter 5 of this work) and find that only the overall maximum vent temperature decreases if background permeability is higher, consistent with the thermodynamic processes described by

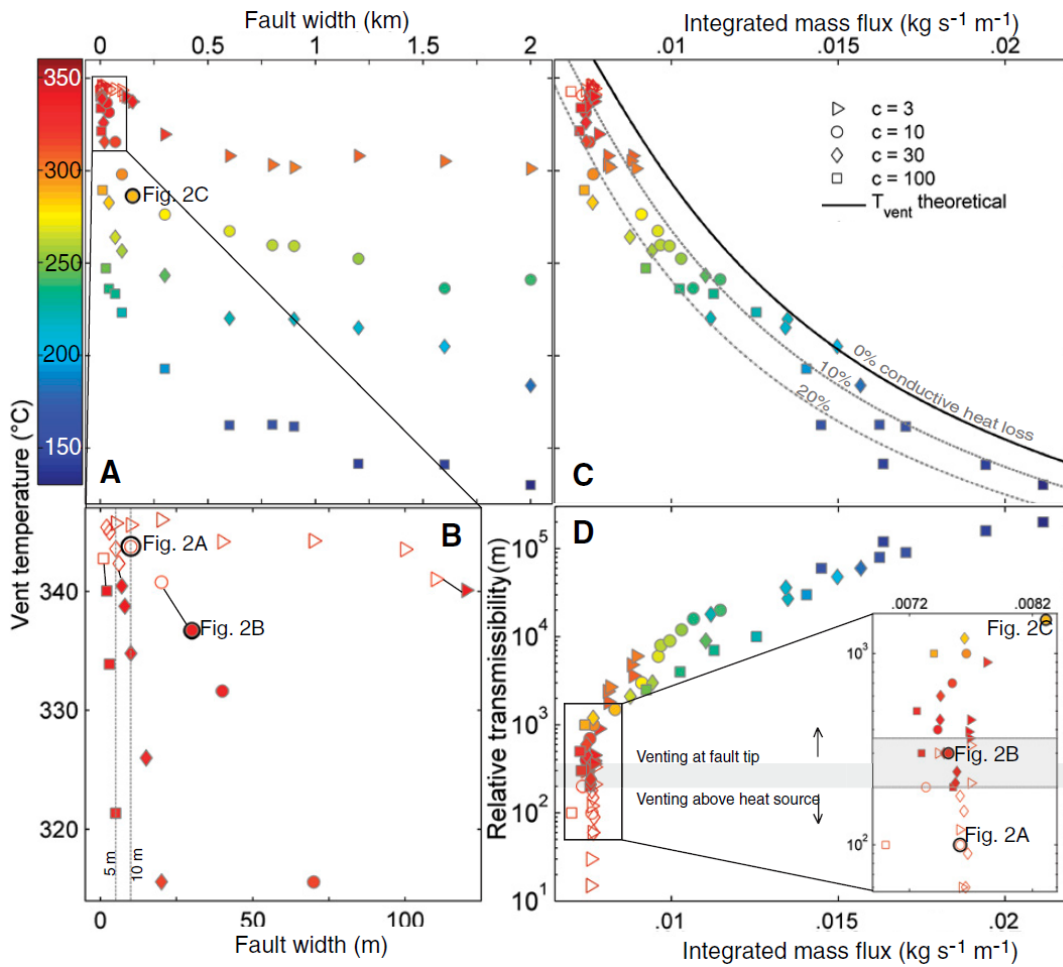


Figure 4.3: Results of all simulations with background permeability $0.5 \times 10^{-15} \text{ m}^2$. Symbols indicate different permeability contrasts, c , and their color shows maximum vent temperature. Filled symbols are simulations with venting at fault tip at Logatchev 1 hydrothermal field (LHF1); open symbols indicate venting above heat source. **A:** For every permeability contrast, vent temperatures decrease with increasing fault width. **B:** Enlargement of part of A. For each permeability contrast, a minimum fault width (connecting black lines) exists above which the rising plume is redirected toward LHF1. **C:** Vent temperatures systematically decrease with increasing integrated mass flux through seafloor. Model results are well fitted by theoretical vent temperatures calculated from equation of state for pure water (curves for 0%, 10%, and 20% conductive cooling at seafloor). **D:** Mass flux and corresponding vent temperatures as function of relative fault transmissibility (fault width times permeability contrast). Inset shows that the transition from venting above heat source to fault-controlled venting at LHF1 occurs over a range of fault transmissibilities of 200–360 m (gray shading). For transmissibilities above 360 m, all venting occurs at LHF1 but at progressively lower temperatures for transmissibilities above 1000 m.

Driesner (2010). Nonetheless, for each permeability contrast there is an optimal fault width that maximizes the vent temperature at the fault termination.

The fluid-dynamic and thermodynamic mechanisms responsible for the trends in figure 4.3a can be explained by the fluid mass fluxes (Figs. 4.2 and 4.3c). The fluid-dynamic influence of a more permeable fault zone is twofold: (1) the inclined geometry of the fault zone induces a horizontal pore-pressure gradient that deflects the mainly buoyancy-driven vertical fluid flow, and (2) the higher permeability within the fault zone results in higher fluid velocities and thereby a higher mass flux compared to upflow outside the fault zone. The example runs shown in figure 4.2 illustrate this: In (A) the mass flux near the fault zone is slightly enhanced but not sufficient to deflect the plume. With a wider fault (B) the horizontal pore-pressure gradient induced by the permeability contrast is sufficient to redirect the entire plume. The mass flux inside an even wider fault zone (C) is further enhanced and causes entrainment of ambient cold seawater, thereby reducing the temperature of the venting fluid.

For a given magmatic energy input, an increase in total discharge mass flux must result in a decrease in vent temperature in order for the transported energy to remain the same. This is highlighted in figure 4.3c, where total discharge mass flux through the seafloor is plotted against maximum vent temperature. Clearly, the higher the mass discharge rate the lower the discharge temperature. The same conclusion can also be reached from a theoretical point of view. Submarine hydrothermal systems are known to operate close to optimal efficiency (Jupp and Schultz, 2004). This implies that rising hydrothermal plumes have a dominant temperature – the one that maximizes buoyancy-driven energy transport (maximum “fluxibility”, Jupp and Schultz, 2000). With this assumption of a dominant characteristic temperature in the upflow zone, a simple energy balance between basal heat input and advective heat loss can be formulated:

$$Q_m = \dot{m}h(T = T_{vent}) - \dot{m}h(T = 4^\circ C) \quad (4.1)$$

Q_{in} denotes total magmatic heat input in W/m, \dot{m}_f is fluid mass flux (both recharging and discharging in steady state) in kg/s/m, and h is the temperature-dependent specific fluid enthalpy in J/kg evaluated at a constant pressure of 30 MPa. Employing the equation-of-state of pure water equation 4.1 can be solved for the venting temperature T_{vent} , providing a theoretical relationship between discharge mass flux and discharge temperature. This theoretical relation is shown as three curves in figure 4.3c, corresponding to cases in which 0%, 10%, and 20% of the basal energy input is conductively transported through the seafloor. In our simulations we quantify the conductive heat flow through the seafloor to be 10-20% of the basal heat input, which explains why most of our predicted venting temperatures plot between these theoretical temperatures.

The striking agreement between modeled vent temperature and the theoretical estimate highlights the strong relationship between discharge mass flux and vent temperature. If we define a fault's relative transmissibility as the product of its width and its permeability contrast to the surroundings, we can examine how relative transmissibility, discharge mass flux and vent temperature are related. From figure 4.3d, we see that the higher the relative transmissibility, the higher is the total mass flux and the lower is the vent temperature— and only a narrow range of relative fault transmissibilities exists for which venting occurs at the fault zone termination with the observed high-temperatures.

4.5 Discussion

The repeated observation of high-temperature off-axis venting on fault traces could have two possible explanations: (1) The driving heat source is located vertically beneath the fault outcrop and the fluids rise more-or-less vertically through less fractured low-permeability rocks, exiting by chance on a fault outcrop. While this could be an explanation for a single vent site, we see no reason to expect it to be generally applicable for the many cases of fault-related high-temperature venting

(e.g. TAG, LHF 1, etc.). (2) As suggested by our numerical results venting fault zones must have a relative transmissibility high enough to redirect a vertically rising plume but low enough to minimize mixing processes between hot hydrothermal and cold ambient fluids. This then raises the question of whether this condition is an innate characteristic of venting faults or whether processes associated with hydrothermal flow somehow modify fault width and/or permeability to favor high-temperature flow.

Potentially important processes for facilitating fault-controlled high-temperature venting are precipitation reactions within the fault zone that clog pore space in an initially too wide or too permeable fault zone. Anhydrite, for example, will precipitate from ambient seawater when it is heated over a temperature interval of 150–200 °C (Seyfried and Bischoff, 1981). This would lead to a progressive sealing of porosity in the fault zone, reducing its relative transmissibility. Silica precipitation may have a similar effect. Such precipitation reactions would progressively reduce mass flux within the fault zone until mixing processes between hot hydrothermal and cold ambient fluid are minimized. At this point, hydrothermal upflow temperatures would reach their maximum. Testing such a self-adjusting mechanism for various initial fault geometries is, however, beyond the scope of this study.

The here studied processes may well be the reason why diffuse low temperature venting is more common than high-temperature venting (Baker et al., 1993). Especially slow-spreading ridges such as the MAR, whose tectonically dominated accretion mechanisms form more heterogeneous crust than fast-spreading ridges, may have a much larger fraction of low- than high-temperature discharge. Supporting evidence comes from global mass-balance budgets for hydrothermal metals in the ocean: If hydrothermal cooling of the young ocean floor would predominantly result in high-temperature venting, the amount of copper carried by the fluids and deposited at the seafloor in the neovolcanic zone should be much larger than observed (Cathles, 2011; Hannington, 2013).

4.6 Summary & Conclusions

High-temperature black smoker systems along slow-spreading ridges such as the MAR are almost always related to tectonic fault zones and therefore are frequently found off-axis. Here we have shown that the intuitive assumption of more efficient high-temperature upflow along high-permeability fault zones only can work under specific conditions. To do so, fault zones need to be just permeable and wide enough to capture and redirect hydrothermal plumes rising from depth but, since they are not isolated conduits, must not be too wide or permeable to prevent cooling through mixing with ambient colder fluids. The frequent occurrence of fault-linked high-temperature vent fields strongly points at a not yet quantified self-adjusting permeability that depends on pore-space clogging reactions between hydrothermal and ambient cold fluids.

Based on these findings and the seismological data, a consistent picture for the Logatchev 1 vent field may be drawn: A magmatic intrusion below a cluster of earthquakes 2 km west of LHF1 drives high-temperature hydrothermal convection. A fault zone, indicated by normal faulting earthquakes, has the optimal relative transmissibility (either by coincidence but more likely by some self-adjusting precipitation reactions) to redirect the rising hydrothermal plume toward the location of the LHF1, resulting in the observed high-temperature venting at the tip of the fault zone.

Our findings further show that an intrinsic relationship exists between permeability, mass flux, and upflow temperature. The higher the permeability, the higher the mass flux, and the lower the vent temperature. This simple relationship may well explain the sparse high-temperature vent fields along the MAR and why the heterogeneous crust of the Atlantic, with its strong permeability contrasts, predominantly cools by lower temperature fluid flow.

Acknowledgments

Constructive reviews of Philipp Weis improved the paper considerably. This paper benefited from valuable feedback of anonymous reviewers and helpful remarks of Colin Devey. We thank Editor Ellen Thomas for the editorial handling. This project could be realized due to the funding of DFG project RU1469/2-1.

References Cited

- Baker, E. T., Massoth, G. J., Walker, S. L., and Embley, R. W., 1993, A method for quantitatively estimating diffuse and discrete hydrothermal discharge: *Earth and Planetary Science Letters*, v. 118, no. 1–4, p. 235-249.
- Bauer, O., 1998, Probst 4.1 PROPERTIES of water and Steam: TU Hamburg Harburg.
- Cathles, L., 2011, What processes at mid-ocean ridges tell us about volcanogenic massive sulfide deposits: *Mineralium Deposita*, v. 46, no. 5, p. 639-657.
- deMartin, B. J., Canales, R. A. R., Canales, J. P., and Humphris, S. E., 2007, Kinematics and geometry of active detachment faulting beneath the Trans-Atlantic Geotraverse (TAG) hydrothermal field on the Mid-Atlantic Ridge: *Geology*, v. 35, no. 8, p. 711-714.
- Driesner, T., 2010, The interplay of permeability and fluid properties as a first order control of heat transport, venting temperatures and venting salinities at mid-ocean ridge hydrothermal systems: *Geofluids*, v. 10, no. 1-2, p. 132-141.
- Fouquet, Y., 1997, Where are the large hydrothermal sulphide deposits in the oceans?: *Philosophical Transactions of the Royal Society of London. Series A: Mathematical, Physical and Engineering Sciences*, v. 355, no. 1723, p. 427-441.
- Grevemeyer, I., Reston, T. J., and Moeller, S., 2013, Micro-seismicity of the Mid-Atlantic Ridge at 7°S to 8°15'S and at the Logatchev Massif oceanic core complex at 14°40'N to 14°50'N: *Geochemistry, Geophysics, Geosystems*, p. n/a-n/a.
- Hannington, M., Jamieson, J., Monecke, T., Petersen, S., and Beaulieu, S., 2011, The abundance of seafloor massive sulfide deposits: *Geology*, v. 39, no. 12, p. 1155-1158.
- Hannington, M. D., 2013, The role of black smokers in the Cu mass balance of the oceanic crust: *Earth and Planetary Science Letters*, v. 374, p. 215-226.
- Hasenclever, J., Theissen-Krah, S., Rupke, L. H., Morgan, J. P., Iyer, K., Petersen, S., and Devey, C. W., 2014, Hybrid shallow on-axis and deep off-axis hydrothermal circulation at fast-spreading ridges: *Nature*, v. 508, no. 7497, p. 508-512.
- Jamieson, J. W., Clague, D. A., and Hannington, M. D., 2014, Hydrothermal sulfide accumulation along the Endeavour Segment, Juan de Fuca Ridge: *Earth and Planetary Science Letters*, v. 395, p. 136-148.
- Jupp, T., and Schultz, A., 2000, A thermodynamic explanation for black smoker temperatures: *Nature*, v. 403, no. 6772, p. 880-883.
- Jupp, T. E., and Schultz, A., 2004, Physical balances in subseafloor hydrothermal convection cells: *Journal of Geophysical Research-Solid Earth*, v. 109, no. B5.

- McCaig, A. M., Cliff, R. A., Escartin, J., Fallick, A. E., and MacLeod, C. J., 2007, Oceanic detachment faults focus very large volumes of black smoker fluids: *Geology*, v. 35, no. 10, p. 935-938.
- Petersen, S., Kuhn, K., Kuhn, T., Augustin, N., Hekinian, R., Franz, L., and Borowski, C., 2009, The geological setting of the ultramafic-hosted Logatchev hydrothermal field (14 degrees 45 ' N, Mid-Atlantic Ridge) and its influence on massive sulfide formation: *Lithos*, v. 112, no. 1-2, p. 40-56.
- Schmidt, K., Koschinsky, A., Garbe-Schonberg, D., de Carvalho, L. M., and Seifert, R., 2007, Geochemistry of hydrothermal fluids from the ultramafic-hosted Logatchev hydrothermal field, 15 degrees N on the Mid-Atlantic Ridge: Temporal and spatial investigation: *Chemical Geology*, v. 242, no. 1-2, p. 1-21.
- Seyfried, W. E., and Bischoff, J. L., 1981, Experimental seawater-basalt interaction at 300°C, 500 bars, chemical exchange, secondary mineral formation and implications for the transport of heavy metals: *Geochimica et Cosmochimica Acta*, v. 45, no. 2, p. 135-147.
- Shilov, V. V., Bel'tenev, V. E., Ivanov, V. N., Cherkashev, G. A., Rozhdestvenskaya, I. I., Gablina, I. F., Dobretsova, I. G., Narkevskii, E. V., Gustaitis, A. N., and Kuznetsov, V. Y., 2012, New hydrothermal ore fields in the Mid-Atlantic Ridge: Zenith-Victoria (20°08' N) and Petersburg (19°52' N): *Doklady Earth Sciences*, v. 442, no. 1, p. 63-69.
- Sinha, M. C., and Evans, R. L., 2004, Geophysical constraints upon the thermal regime of the ocean crust, *Mid-Ocean Ridges: Hydrothermal Interactions Between the Lithosphere and Oceans*, Volume 148: Washington, DC, AGU, p. 19-62.

Manuscript received 23 July 2014

Revised manuscript received 22 October 2014

Manuscript accepted 28 October 2014

5 Energetics of hydrothermal circulation in heterogeneous ocean crust

Christine Andersen, Lars Rüpke and Jörg Hasenclever*
GEOMAR, Helmholtz Centre for Ocean Research Kiel, Germany

Abstract

Slow-spreading ridges produce highly heterogeneous crust along their tectonic and magmatic segments with significant permeability contrasts across structural and lithological interfaces. The crustal permeability structure has a strong control on vent field location such that off-axis hydrothermal systems are frequently located at outcropping fault zones on the seafloor. We have previously shown that preferential flow of hydrothermal fluids along high-permeability conduits inevitably causes a temperature drop. This is difficult to reconcile with fault-related high-temperature venting that has been observed. Here we further address this problem by exploring the energetics of hydrothermal convection in heterogeneous ocean crust using 2D flow simulations. We focus our analysis on the energy balance of rising hydrothermal plumes and on mixing processes at permeability boundaries and have established a more robust theoretical framework for hydrothermal flow through heterogeneous ocean crust. A semi-analytical relation between heat input, upward mass flux and temperature in the upflow zone is used to predict vent temperatures in systems with a heterogeneous permeability field.

5.1 Introduction

Recent advances in hydrothermal flow modeling have revealed the key thermodynamic and fluid-dynamic controls on hydrothermal convection patterns and vent temperatures at oceanic spreading centers. The observed upper limit to black smoker vent temperatures of approx. 400°C can be explained by the

*Paper in preparation

thermodynamic properties of water (Jupp and Schultz, 2000). 3D models of hydrothermal flow at fast-spreading ridges show cylindrical upwellings with closely interwoven recharge flow (Coumou et al., 2008; Hasenclever et al., 2014). Driesner (2010) has shown that black smoker temperatures can only be reached when rock permeability is not too high, since vent temperatures decrease with increasing homogenous permeability. These studies provide a robust theoretical basis for hydrothermal flow observations at fast-spreading ridges, which commonly are not associated with sharp permeability contrast. The situation in slow-spreading environments like the Mid-Atlantic Ridge is different since significant heterogeneities in the permeability field have a major influence on hydrothermal fluid temperatures.

In addition to the simulation runs which examined the hydrothermal circulation of the Logatchev 1 field at the Mid-Atlantic ridge (Chapter 4, Andersen et al., 2015) we have conducted a series of simplified model runs, which were performed to assess further details of mixing processes at permeability boundaries by looking at the energy balance of rising hydrothermal plumes. Moreover the simplified model runs help to evaluate the role of fault dip and bathymetry on the relation between permeability, hydrothermal flow pattern, mass flux and resulting vent temperatures at the seafloor. All runs assume a flat seafloor at the top of the domain; the permeability field is becoming increasingly more complex: following hydrothermal flow simulations in a model domain with a homogenous permeability, we conducted a set of runs with a layered set-up, including a permeable upper layer. The next, more complex runs include a vertical fault zone (i.e. a slot). The same processes that control vent temperatures in the more complex Logatchev (Chapter 4) setup can also be identified in the simplified model runs including a vertical slot. The higher the relative fault transmissibility, which is controlled by slot width and permeability contrast to the surrounding (section 4.4), the higher is the mass flux in the slot and the more cold water is drawn into the slot, which reduces the upflow temperature.

5.2 Theoretical framework

Simplified 2D flow models can be used to predict temperatures of hydrothermal fluids in the upflow zone within a permeable layer and in a permeable slot (see Fig. 5.1). If we assume a cold hydrostatic pressure gradient ($\nabla P = \rho_0 g$) in the upflow zone, Darcy's law (see also Equ. 3.1) can be used to compute upflow velocities v_u :

$$v_u = -\frac{k}{\mu(T_u)} (\rho_0 g - \rho_u(T_u) \vec{g}) \quad (5.1)$$

Subscript u refers to upflow properties and $g = -9.81$ is used as value for the gravitational acceleration vector (see table 4.1 in chapter 4 for all other model parameters). The total discharging mass flux m_u (see also section 3.2.1.2) leaving reaction zone 1 in figure 5.1 is described by:

$$\dot{m}_u = 2L v_u \rho_u(T_u) \quad (5.2)$$

with L being the half width of the rising hydrothermal plume. Equation 5.1 and 5.2 show clearly that upflow velocity and consequently mass flux is directly dependent on permeability and indirectly (via fluid viscosity and density) on temperature inside the upflow zone. Energy conservation (see also section 3.2.1.2) requires that the energy (mass flux times specific fluid enthalpy h , which also is temperature dependent) of the fluids leaving the reaction zone is equal to the energy carried by the recharge flow plus the energy input from the magmatic heat source Q_{in} :

$$\dot{m}_u h_u = \dot{m}_r h_r + Q_{in} \quad (5.3)$$

Mass conservation (see also section 3.2.1.2) requires that the recharging mass flux is equal to the discharging mass flux ($m_r = m_u$), such that we can express the magmatic heat input as:

$$Q_{in} = \dot{m}_u (T_u) \cdot (h_u(T_u) - h_0) \quad (5.4)$$

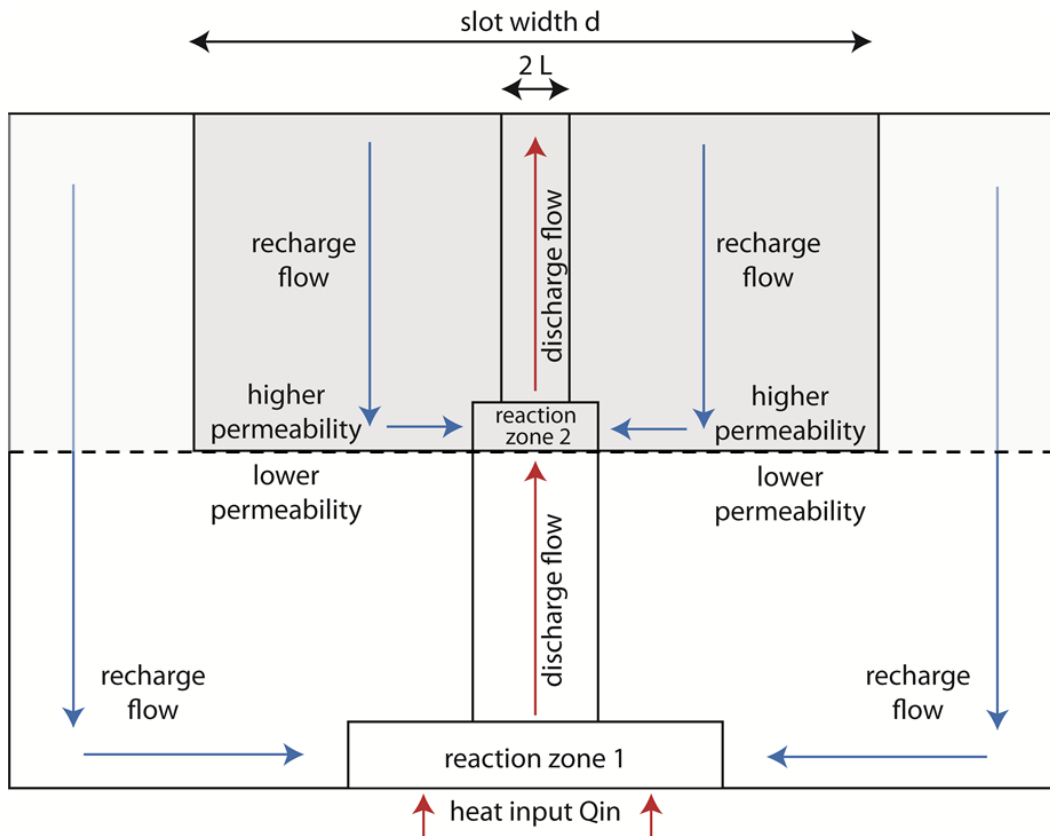


Figure 5.1: Schematic model set-up for the regions referred to in the derivation of the semi-analytical solution (Equ. 5.4, section 5.2). The dark grey area marks a permeable slot, the light grey area a permeable upper layer.

where T_u is upflow temperature and h_0 refers to the specific enthalpy of cold recharging seawater. This equals equation 6 (p. 137) in Driesner (2010) and equation 7 in Jupp and Schultz (2004). Driesner (2010) successfully used this equation to predict and explain temperatures in the upflow zone for a homogenous medium and a constant heat input. Equation 5.4 can be used to predict fluid temperatures in the upflow zone for a given energy input. Since equation 5.4 does not provide a direct analytical solution for T_u , which has to be solved for by a root finding algorithm in combination with the equation of state for water, we call it semi-analytical solution (see example Fig.5.3).

5.3 Simulation results

In all model runs the peak of the Gaussian-shaped heat source is located in the center of the lower model boundary and the heat input is constant ($Q = 12.5$ kW per meter ridge axis as typical value for the slow-spreading MAR, Sinha and Evans (2004)). The same numerical approach as described in section 3.2 is applied for all hydrothermal flow simulations presented in this chapter.

5.3.1 Homogenous and simple layered systems

The temperature field of a layered model domain with a permeable upper layer (permeability upper layer: 10^{-14} m², permeability lower layer: 2×10^{-15} m², permeability contrast: $c=5$) is shown in figure 5.2. The rising hydrothermal plume is narrowing and peak temperatures inside the plume are decreased when the plume is crossing the permeability boundary between the two layers.

Fig. 5.3 shows vent temperatures and mass fluxes computed by the hydrothermal flow model for homogeneous permeability field (red crosses) and for a layered (2km x 2km, as in Fig. 5.2) system (green circles) compared to the semi-analytical solution (Equ. 5.4) derived above (blue curves). Fluid properties are evaluated at 35 MPa and the half width L of the upflow zone is set to 50m (roughly corresponding to the narrow hydrothermal plume in the permeable upper layer, Fig. 5.2). Vent temperatures and mass fluxes from model runs with a homogeneous permeability agree well with both the vent temperatures and mass fluxes predicted from the analytical solution. In the layered model runs the lower layer has a constant permeability of 2×10^{-15} m² as above and the permeability of the upper layer is systematically varied between 3×10^{-15} m² and 10^{-13} m² (corresponding to values on the x-axis). It can clearly be seen, that vent temperatures in a layered system are controlled by the higher permeability of the upper layer and can thus be predicted from the semi-analytical solution in the same way as a homogenous system (with the higher permeability of the upper layer).

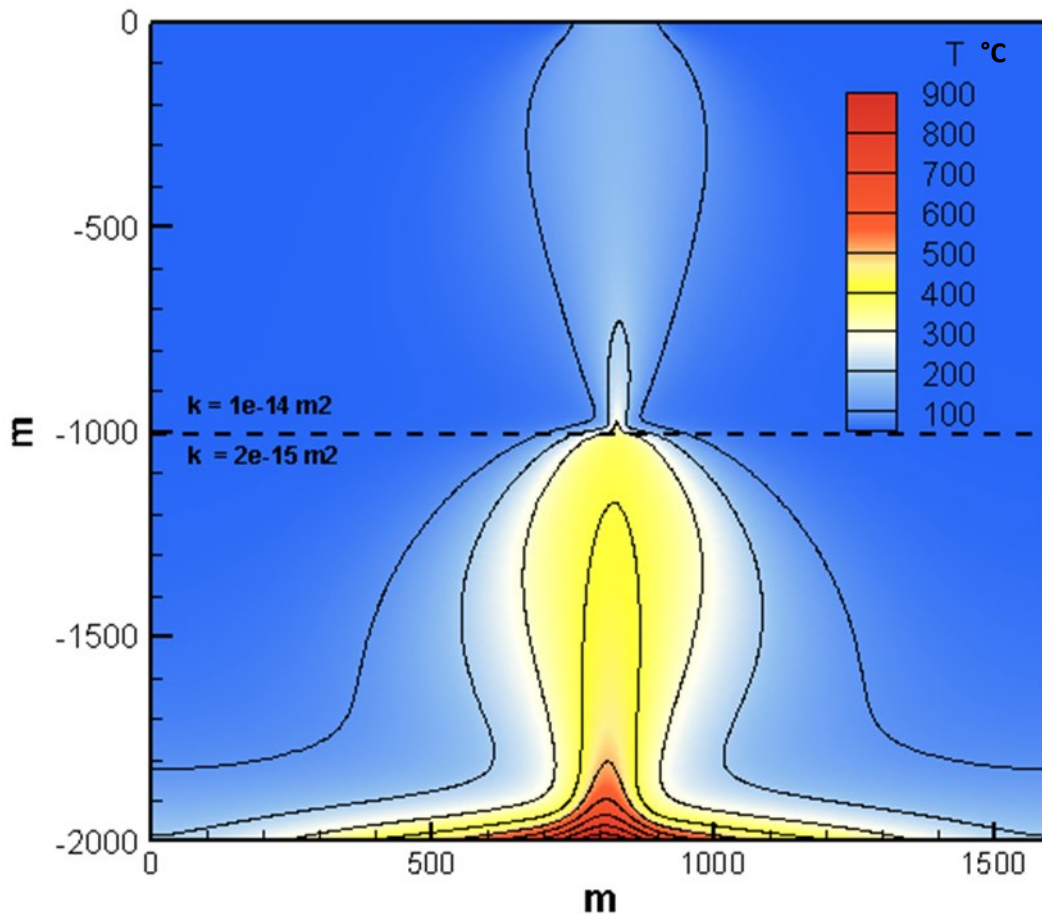


Figure 5.2: Temperature field of a rising hydrothermal plume in a layered system. The plume is significantly narrowed and temperatures are reduced when it crosses the boundary to the more permeable upper layer.

5.3.2 Heterogeneous systems including a vertical slot

As a next step we have conducted two series of model runs, which include a vertical permeable slot as shown in figure 5.1 (also Fig. 5.5) with a permeability of $5 \times 10^{-15} \text{m}^2$ and 10^{-14}m^2 respectively. The background permeability was remaining constant on $2 \times 10^{-15} \text{m}^2$, the dimensions of the model domain was $2 \text{km} \times 2 \text{km}$. The width of the slot has systematically been increased from 50m to 1km in order to investigate the influence of slot width on vent temperature. It can be seen how both sets show a clear decrease in vent temperature with increasing slot width (Fig. 5.4). The vent temperature from the model run with the homogeneous permeability of the

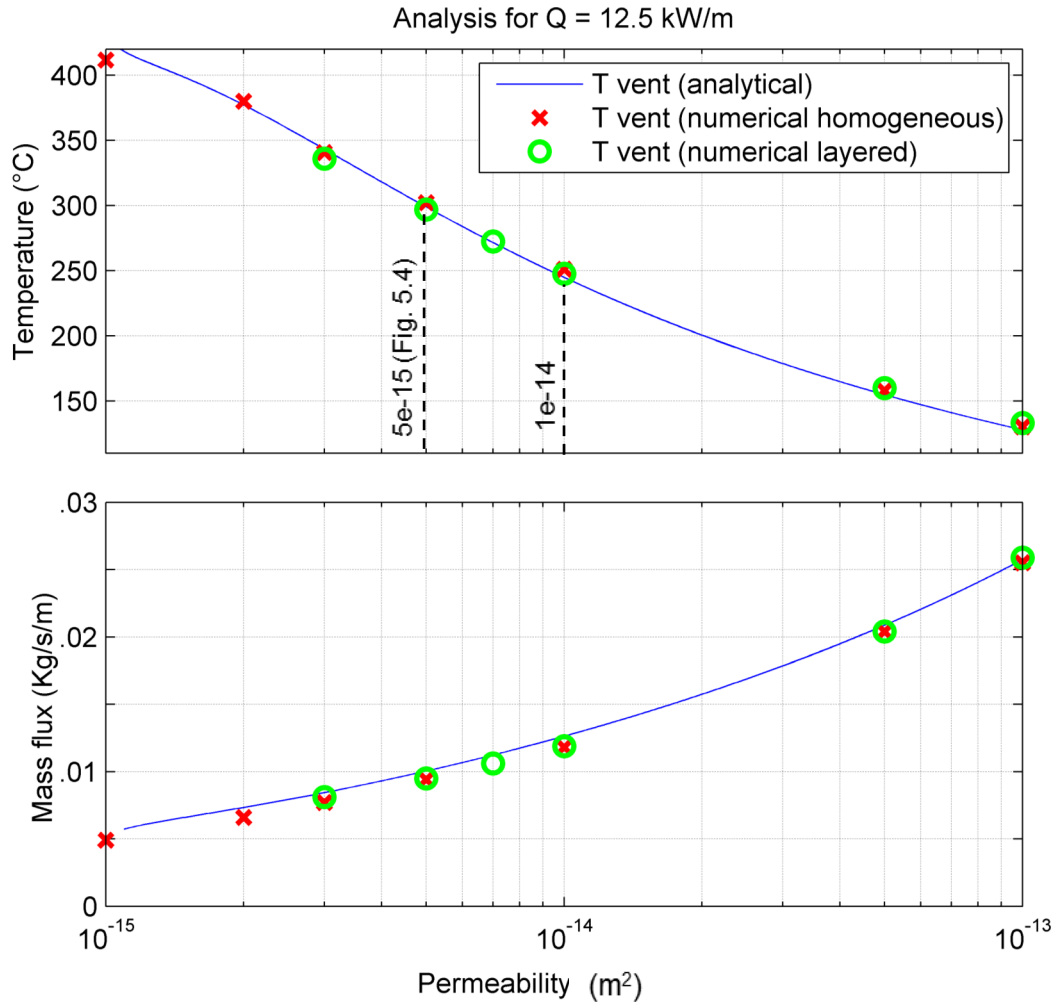


Figure 5.3: Temperatures and mass fluxes from numerical simulations in a system with homogeneous permeability (x-axis) and in a layered system agree well with the semi-analytical solution (Equ. 5.4). The lower layer in the layered model runs has a constant permeability of $2 \times 10^{-15} \text{ m}^2$ and the permeability of the upper layer varies between $3 \times 10^{-15} \text{ m}^2$ and 10^{-13} m^2 (x-axis).

background marks an upper endmember for both set of runs (red star). This homogeneous endmember can also be viewed as a slot run with infinitely small slot width. On the lower end each set of runs approaches the vent temperature corresponding to the homogeneous set-up with the higher permeability of the slot. A very wide slot is approaching the layered set-up described above, for which vent temperatures can be predicted from the semi-analytical solution. Therefore, the

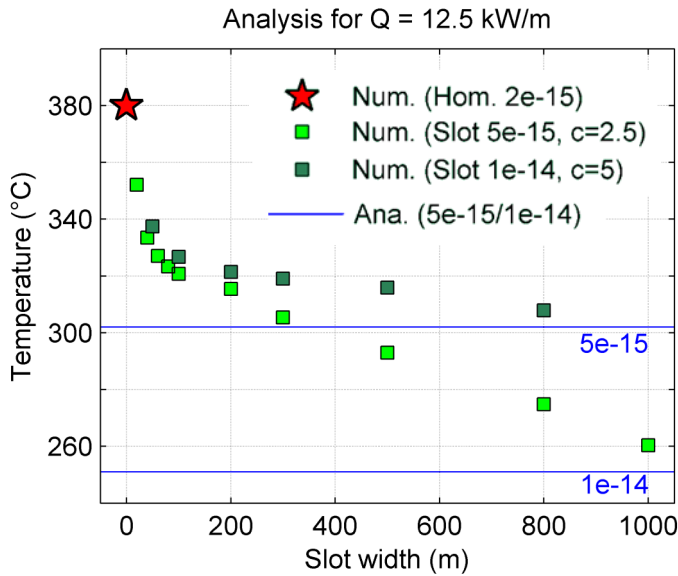


Figure 5.4. Systematic results from two sets of model runs including a vertical permeable slot. With increasing slot width, each set approaches the lower temperature limit given by the semi-analytical solution for the higher permeability of the slot (very wide slot = layered case). The lower background permeability (marked by the red star, homogeneous case = infinitely narrow slot) marks an upper boundary for temperatures.

width of the slot seems to be the parameter which determines the vent temperature, which lies between the two endmember values controlled by background and slot permeability respectively. In agreement to our previous findings (Chapter 4) vent temperature are thus decreasing with increasing transmissibility of the slot (width*c). In this hydrothermal system, associated with a heterogeneous permeability, vent temperature thus depends on the slot width, which defines an average (or effective) permeability along the fluid pathway.

To further illustrate the active processes and to investigate the control of the model dimension as well as to compare the slot results to the results from the Logatchev hydrothermal field from chapter 4, we have conducted additional slot runs using a larger model domain ($\sim 5.5 \times 5.5 \text{ km}$). Results from these runs are illustrated in figure 5.5, which show runs with 500m and 5km wide slots and a permeability contrast between slot and background rocks of $c=3$ and 50. The flat seafloor at the top of the domain is assumed 3.5 km below sealevel, which is the average depth of the LHF1 transect (Fig. 4.1). The slot extends 3.5km below the seafloor which roughly corresponds to the depth where the plumes enter the fault in the more complex LHF1 setup. Vent temperatures decrease from (a) to (d) with

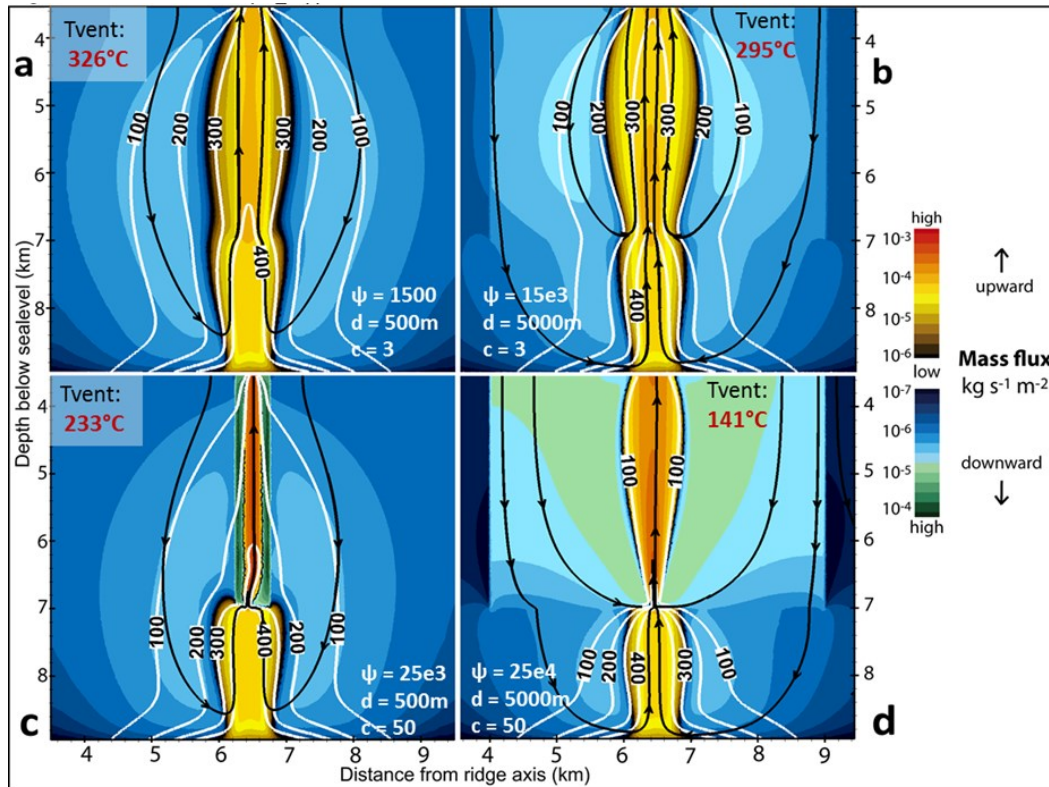


Figure 5.5: Results of simulations including a flat seafloor 3.5 km below sealevel and a vertical slot with width d . The permeability contrast between slot and surrounding is given by $c=3$ in (A and B) or $c=50$ (D and C). Slot transmissibility ($\psi=c*d$) increases from A to D, which results in a constant increase in mass flux with a decrease in vent temperature as the consequence of entraining cold seawater.

increasing relative transmissibility $\gamma = d*c$, ($c =$ permeability contrast between slot and background). In (a) mass flux increases when the hydrothermal plume is entering the 500m wide slot. Recharge flow, indicated by the downward mass flux in blue and by the black flow lines, occurs mainly through the low-permeability rocks in the vicinity of the slot. Recharging fluids feed the lower part of the rising, 400°C hot plume (indicated by white isotherms) and as consequence resulting vent temperature at the top are high (326°C). In (b) the relative transmissibility of the slot is enhanced by increasing slot width by a factor of 10 to 5km. A separate upper recharge convection cell develops inside the wide slot. The cold seawater entrains the rising hot hydrothermal plume at the base of the slot further away from the heat

source at depth. This extensive mixing in the upper part of the hot plume leads to significantly reduced vent temperatures in contrast to the narrower slot with the same permeability structure (a). The high permeability contrast in (c) and (d) strongly increases the mass flux inside the slots. In both cases a hydrothermal recharge and discharge flow occur next to each other inside the slot. In the narrower slot (c) the recharge flow inside the slot can be identified by the downwards mass flux indicated by the dark green color. The rising hydrothermal plume is narrowed and mixes with the colder entraining fluids. A high permeability contrast in a wide slot (d) yields the highest relative transmissibility and hence the highest mass flux which results in the lowest vent temperatures of the four calculations.

In chapter 4 simulation results of the Logatchev 1 field were presented, where fault width and permeability contrast have systematically been varied. For each permeability contrast all sets of runs show the same trend: if the fault is narrow, vent temperatures are high but venting occurs above the heat source rather than at the known position of the LHF1. Increasing the fault width leads to venting at LHF1 but vent temperatures decrease (Fig. 4.3 and filled symbols in Fig. 5.6). We have performed a series of 29 additional simulations with the above described setup including a vertical slot (Fig. 5.5). The width of the vertical slot has been varied between 200m and 5km. Symbols with grey filling are vent temperatures from the slot runs and solid filled symbols are the vent temperatures from the LHF1 simulations (Fig. 5.6). It can clearly be seen that even if vent temperatures from the more complex LHF1 simulations are systematically lower, they nicely match the trends of the simplified slot simulations. This implies that the same mixing processes are active at permeability boundaries in a more complex system including an inclined fault zone and actual seafloor bathymetry. However vent temperatures achieved during the slot runs on the large model domain (Fig. 5.5) are not approaching the vent temperatures for the homogeneous permeability of the slot predicted from the semi-analytical solution (Fig. 5.3) but are significantly lower (see also discussion (5.4)).

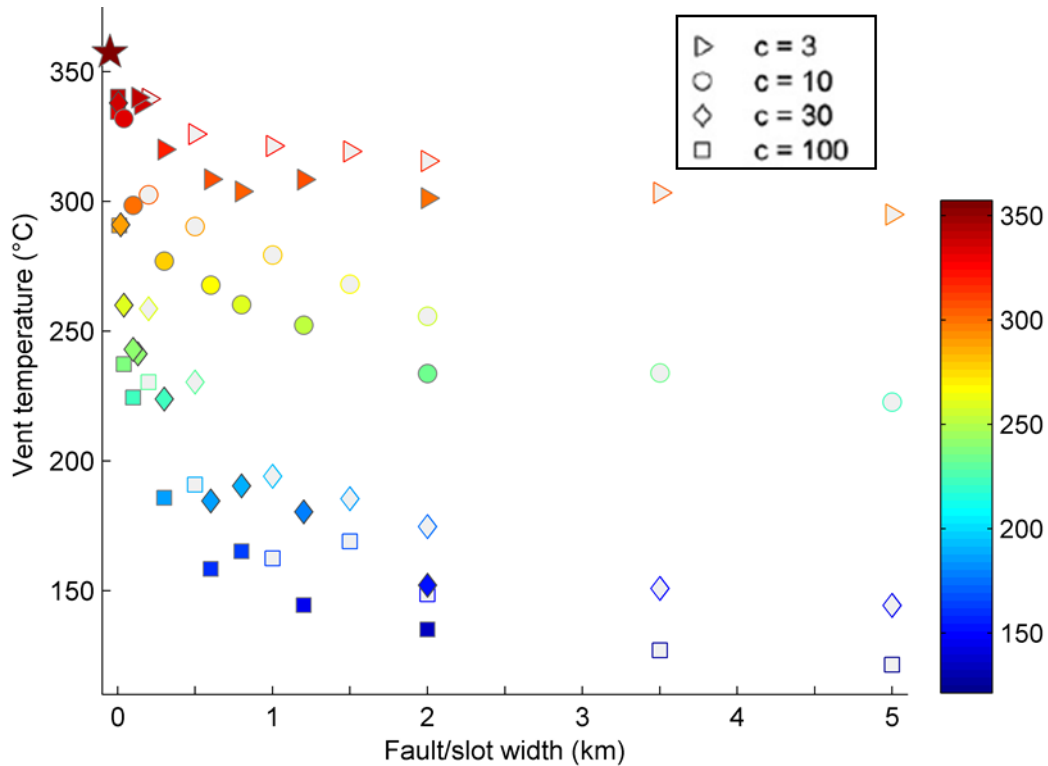


Figure 5.6: Simulation results from slot runs with systematically varied slot width (symbols with grey filling) compared to the results from the LHF1 study (symbols with solid filling, see also Fig. 4.3a, chapter 4). For each permeability contrast c , the slot runs follow the trends of the LHF1 set with the same c , the LHF1 temperatures however are systematically lower.

5.3.3 Heterogeneous, faulted systems

We have further conducted 32 model runs (these results have been published in the supplement¹ to Andersen et al., (2015)) where the setup of LHF1 (see section 4.3) was applied and a constant permeability contrast $c = 10$ between fault zone and surrounding. In order to test the influence of background permeability, it was enhanced to 10^{-15} m^2 and $2 \times 10^{-15} \text{ m}^2$ in comparison to the original runs which had a background permeability of $0.5 \times 10^{-15} \text{ m}^2$ (Chapter 4). The trend in vent temperature and mass flux which is described in chapter 4 is clearly also visible in

¹GSA Data Repository item 2015032; doi:10.1130/G36113.1, available online at www.geosociety.org/pubs/ft2015.htm

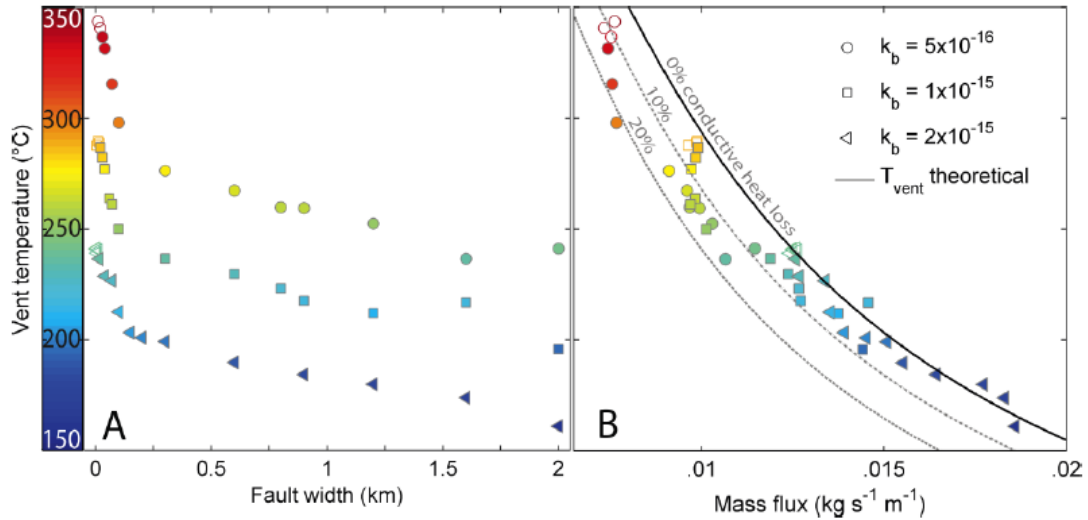


Figure 5.7: Vent temperatures of additional LHF1 simulations plotted against fault width and mass flux. The permeability contrast $c = 10$ is constant in all runs while the absolute background permeability k_b is changed as indicated by the different symbols. Their color shows maximum vent temperature. Filled symbols are simulations with venting at the fault tip at LHF1, open symbols indicate venting above the heat source. **A:** Vent temperatures decrease with increasing fault width for each constant background permeability. The same is valid for any fault width and increased background permeability **B:** Vent temperatures systematically decrease with increasing total mass flux through the seafloor. Model results are well fitted by theoretical vent temperatures calculated from the EOS for pure water (curves for 0, 10, and 20% conductive cooling at the seafloor) described in chapter 4.

these simulation sets: vent temperature decreases with increasing fault width, the highest mass fluxes occur at the lowest vent temperatures (Fig. 5.7). For any simulated fault width the vent temperature is decreased by $\sim 40^\circ\text{C}$ when the permeability of the background is doubled (Fig. 5.7). Consequently, at the lowest background permeability ($0.5 \times 10^{-15} \text{ m}^2$) the highest vent temperature is reached at the fault termination at the seafloor. The threshold width for deviation of the rising hydrothermal plume into the fault is decreased with increasing absolute background permeability, visible at the transition from unfilled to filled symbols (Fig. 5.7).

5.4 Discussion

The underlying physics of the simulation results presented above can be understood by reviewing the key processes that control vent temperatures in a homogenous medium. According to the ‘fluxibility’ approach by Jupp and Schultz (2000) hydrothermal plumes have a natural tendency to form and rise at $\sim 400^\circ\text{C}$ due to the thermodynamic properties of pure water (see also Fig. 3.2). This implies that the temperature at maximum fluxibility is also the maximum temperature that can be achieved in pure water convection. They can, however, only be achieved if the balance between hydrothermal cooling and basal heating permits the build-up of a hot enough boundary layer (Driesner, 2010). All processes that can cool a hot hydrothermal plume during ascend will cause a reduction in vent temperature, which is what happens in the here discussed simulations.

The mass and energy conservation principles derived in section 5.2 above can be used to explain fluid temperatures in a hydrothermal plume that flows through a medium that has a heterogeneous permeability structure (layered system or vertical slot). We predict temperatures of the discharge flow leaving reaction zone 2 in figure 1, where the hydrothermal plume enters the region with higher permeability. The heat input is still Q_{in} , which is now transferred into the reaction zone by advection. The discharge velocity is now controlled by the higher permeability above the interface (permeability of upper layer/slot). As a consequence, the discharging mass flux is higher than the mass flux of the hydrothermal plume coming from below, which causes additional recharge flow into reaction zone 2. This entrainment of cold water causes a reduction in upflow temperature above reaction zone 2. If the slot is wide enough the entire recharge and discharge flow occurs within the more permeable slot, the domain is then comparable to a layered system. In this case the upflow (aka vent temperature) can be predicted with equation 5.4. If the slot width is not big enough, part of the recharge flow will happen through the less permeable matrix around the slot. In this case, the upward

mass flux is buffered by the limiting recharge flow through the less permeable rocks surrounding the slot. As a consequence, vent temperatures are higher because the mass flux in the upflow zone is lower – this simply follows from energy conservation. In summary, total vertical mass flux increases with permeability (see Darcy’s law) and cross-sectional area of the upflow zone. Thus, for a given total energy input (12.5 kW in all our model calculations) fluid temperatures must decrease if mass flux increases, because energy conservation requires that the total energy carried by the fluid remains constant. Note that the above quantitative analysis is possible because we use a constant heat flux boundary condition in our models (i.e. Q_{in} is exactly known and constant). Imposing a constant temperature at the domain base would always heat fluids to the prescribed temperature (independent of the actual mass flux) so that there would be no control on the heat flux into the system. This, in turn, would make it difficult or impossible to systematically compare venting temperatures of runs with different fault width and permeability, because they develop very different mass fluxes.

It can further be noted that the above considerations are largely independent of the model setup as they are mainly controlled by the thermodynamic properties of water. The few existing 3D simulations of pure-water hydrothermal convection clearly show that fluid properties and not the exact 2D or 3D patterns of convection control upflow temperatures above a heat source (Coumou et al., 2008; Hasenclever et al., 2014). Likewise, Driesner (2010) showed that the relationship between vent temperature and permeability also holds when seawater, instead of pure water, is assumed.

The vent temperatures of the simplified runs are systematically higher than the ones from the more complex LHF1 runs (Fig. 5.6). The reason for this might be that the fault dip results in a longer transport way along the fault zone, which might cause a higher amount of conductive heat loss from the hot hydrothermal fluids to the surrounding rocks. Possibly for the same reason vent temperatures achieved during the slot-runs on the large model domain (Fig. 5.5) are not approaching the

vent temperatures for the homogeneous permeability of the slot (Fig. 5.6) predicted from the semi-analytical solution (Fig. 5.3) but are significantly lower.

Moreover a previous study has shown that in submarine settings rising hydrothermal plumes are attracted by bathymetric highs (Bani-Hassan et al., 2012). Thus seafloor bathymetry has an impact on hydrothermal flow pattern, which is why it does not seem relevant for the findings presented in this paper regarding the controls on hydrothermal vent temperatures. However, fault dip might control the deviation of a hydrothermal plume into the fault zone while bathymetry might further impact the exact location of hydrothermal discharge at the seafloor.

5.6 Summary & Conclusions

The results from the simplified simulation runs further illustrate the complexity of hydrothermal fluid flow in heterogeneous and faulted ocean crust. They confirm the fundamental difficulty of transporting high-temperature fluids through such rocks towards the seafloor, which was already pointed out in chapter 4. Here we have provided a more detailed analysis and explanation of the responsible physical processes.

The permeability above a heat source must be low for sustaining $>300^{\circ}\text{C}$ hot fluid flow (see also Driesner (2010)). The same is true for every lithological boundary that the rising hydrothermal plume may encounter during its ascent to the seafloor. If the plume enters a structure with higher permeability, like a fault zone or lithological boundary, upflow temperatures will decrease as a consequence of increased mass flux and mixing with ambient cold seawater.

We have further shown that a semi-analytical solution cannot only predict upflow temperatures in homogenous systems (Driesner, 2010) but can also be used to predict upflow temperatures in more complex, heterogeneous systems that include a vertical slot and trends in a system with an inclined fault zone and real seafloor bathymetry. Vent temperatures will range between two end-member

temperatures given by the semi-analytical solution: the homogeneous case with slot permeability (lower temperature limit) and the homogeneous case with background permeability (upper temperature limit). Vent temperature in hydrothermal systems associated with a heterogeneous crustal permeability thus depend on permeability contrasts and on the geometry of the permeable body, like the width of a fault, which defines an average (or effective) permeability along the fluid pathway.

References Cited

- Andersen, C., Rüpke, L., Hasenclever, J., Grevemeyer, I., and Petersen, S., 2015, Fault geometry and permeability contrast control vent temperatures at the Logatchev 1 hydrothermal field, Mid-Atlantic Ridge: *Geology*, v. 43, no. 1, p. 51-54.
- Bani-Hassan, N., Iyer, K., Rupke, L. H., and Borgia, A., 2012, Controls of bathymetric relief on hydrothermal fluid flow at mid-ocean ridges: *Geochemistry Geophysics Geosystems*, v. 13.
- Coumou, D., Driesner, T., and Heinrich, C. A., 2008, The structure and dynamics of mid-ocean ridge hydrothermal systems: *Science*, v. 321, no. 5897, p. 1825-1828.
- Driesner, T., 2010, The interplay of permeability and fluid properties as a first order control of heat transport, venting temperatures and venting salinities at mid-ocean ridge hydrothermal systems: *Geofluids*, v. 10, no. 1-2, p. 132-141.
- Hasenclever, J., Theissen-Krah, S., Rupke, L. H., Morgan, J. P., Iyer, K., Petersen, S., and Devey, C. W., 2014, Hybrid shallow on-axis and deep off-axis hydrothermal circulation at fast-spreading ridges: *Nature*, v. 508, no. 7497, p. 508-512.
- Jupp, T., and Schultz, A., 2000, A thermodynamic explanation for black smoker temperatures: *Nature*, v. 403, no. 6772, p. 880-883.
- Jupp, T. E., and Schultz, A., 2004, Physical balances in subseafloor hydrothermal convection cells: *Journal of Geophysical Research-Solid Earth*, v. 109, no. B5.
- Sinha, M. C., and Evans, R. L., 2004, Geophysical constraints upon the thermal regime of the ocean crust, *Mid-Ocean Ridges: Hydrothermal Interactions Between the Lithosphere and Oceans*, Volume 148: Washington, DC, AGU, p. 19-62.

II Seafloor spreading

6 Background on oceanic ridges

Only about half a century ago scientists discovered repeating magnetic anomalies on the seafloor of the Atlantic and Indian Ocean (Vine and Matthews, 1963; Vine, 1966). They suggested that variations in intensity and polarity of Earth's magnetic field may be fossilized in the oceanic crust, which is constantly created at oceanic ridges. This discovery should confirm the seafloor-spreading theory (Hess, 1962), which was based on Alfred Wegener's much criticized theory of Continental Drift, which he had published in 1912. Today the theory of plate tectonics is accepted by the major part of the scientific community and much research is done on the complex detailed processes associated with the movement of the tectonic plates. Ideas and scientific methods to study ocean ridges have developed rapidly, providing numerous new data and insights into the processes that are leading to the continuous generation of new oceanic crust. As Macdonald (1998) had already pointed out, instead of only focusing on a higher degree of specialization of different aspects of oceanic ridges it is important to study the links between tectonic and magmatic processes and hydrothermal activity at seafloor spreading centers. This agrees well with the goal of this thesis, which is to gain a better understanding of the interactions between the processes above (section 1.2). In order to test the key hypothesis of this work, stating that the tectono-magmatic state of slow-spreading ridges controls the position of hydrothermal vent fields, I have developed a mechanical model that simulates the lithosphere-scale deformation field during seafloor spreading (Chapter 7). This is the first step for a later coupling with hydrothermal convection models as in chapter 4 and 5.

6.1 Characteristics of ridges at different spreading rates

Oceanic ridges (Fig. 6.1) are located at divergent tectonic plate boundaries (also Fig. 2.2) of the Earth's rigid outer shell, the lithosphere. Oceanic ridges are frequently referred to as Mid-Ocean Ridges (MOR), while strictly speaking this term only

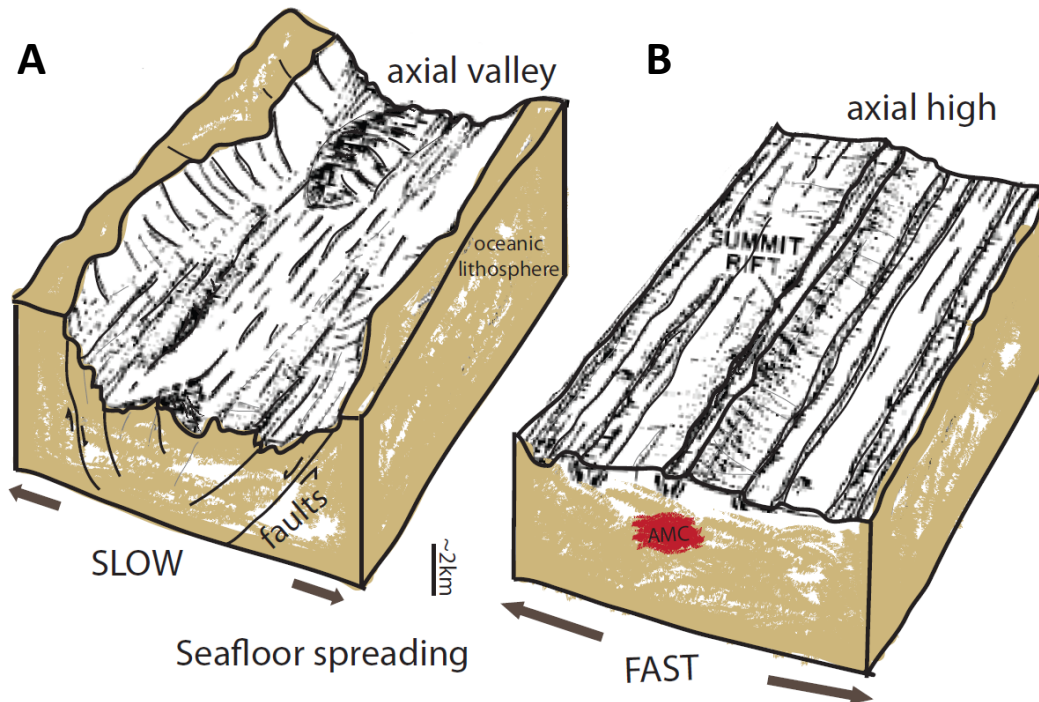


Figure 6.1: Schematic illustration of accretion of oceanic crust at two endmember types of Mid-ocean ridges, modified after Macdonald, (1982). **A:** a slow-spreading ridge with a distinct, axial valley, rough topography and numerous valley bounding faults. Here, seafloor spreading is occurring to a high degree via large scale tectonic faults. **B:** fast-spreading ridge, which shows an axial high and a more continuous topography along axis. Lava is erupting at a narrow rift at the summit of the axial high, an axial magma chamber (AMC) is situated at 1-2km below the ridge axis. Formation of new oceanic crust thus happens mainly via magmatic processes and to a lower degree via tectonic faulting.

applies to those ridges, which are located in the middle of an ocean, like the Mid-Atlantic Ridge. The global ridge system has a length of approximately ~50.000 km (German and Lin, 2004; Hannington et al., 2005). With only ~5-30km width, the ridges are narrow compared to the plates, which can be thousands of kilometers across (Macdonald, 2001). Oceanic ridges are large, volcanically highly active, submarine mountain chains, where a major part of the global volcanic activity occurs (Perfit and Chadwick, 1998; Macdonald, 2001; Hannington et al., 2005). Magma ascents from depth filling the gap between the separating tectonic plates such that new oceanic crust is constantly formed (Macdonald, 2001). Roughly 18

km³ of crust is formed at oceanic ridges per year (Sigurdsson and Houghton, 2000; Hannington et al., 2005). The velocity at which the plates are separating is highly varying. This has led to a classification according to spreading rate (which can vary somewhat in the literature e.g Baker and German, 2004; Hannington et al., 2005): slow-spreading ridges (Fig. 6.1a), like the most prominent example the MAR, have an opening velocity of up to 40 mm/yr (full spreading rate). Intermediate spreading ridge vary in spreading rate from 40 – 60 mm/yr. Fast spreading ridges (Fig. 6.1b) have a spreading rate of 60-100 mm/yr, like the East Pacific Rise (EPR) followed by superfast spreading ridges with spreading rates >100 mm/year.

Early exploration of seafloor spreading centers already suggested that ridge crest topography depends on spreading rate (Menard, 1967). Numerous following studies have confirmed such a relation (reviewed by e.g. Macdonald, 1982; Small, 1998): slow-spreading ridges typically show a ~1.5-3 km deep, rough valley at the axis of the oceanic ridge, which has flanks uplifted by faulting (Fig. 6.1a). At intermediate rates the valley is only on the order of tens – hundreds of m deep, while fast spreading ridges lack an axial valley and are marked by narrow, <250 m, often <50m (Perfit and Chadwick, 1998), and more regular axial highs, ~100-200m high (Morgan and Chen, 1993a), instead (Fig. 6.1b). In their MOR review papers Macdonald (1998) and Perfit and Chadwick (1998) discuss the control of magma supply on ridge axis morphology. This dependence has already been suggested from numerical modeling results by (Morgan and Chen, 1993a)). They proposed that axial morphology is controlled by the thermal structure at the ridge axis, which is a function of spreading rate and magma supply. It is now generally accepted that fast-spreading ridges have a higher magma supply (Baker and German, 2004; Hannington et al., 2005) than slow-spreading ridges (Fig. 6.1). At the fast-spreading EPR a bright reflector visible in seismic refraction data has been interpreted to be a narrow (1-2km) lens of partially molten magma (Fig. 6.1b) on top of a larger zone of crystal mush (Sinton and Detrick, 1992). The depth to this magma reservoir is also varying with spreading rate: at fast spreading ridges it has

been imaged at a depth of ~2km depth and at ~3-4km depth at intermediate spreading rates (Perfit and Chadwick, 1998). In slow-spreading ridge settings, like at the MAR, such magma reservoirs are found more rarely (Detrick et al., 1990). In a specific setting a magma chamber has been imaged below one of the largest central volcanoes along the MAR at the Lucky strike hydrothermal field (Singh et al., 2006). Also Morgan and Chen (1993b) suggest in their numerical modeling study that a steady-state magma reservoir is lacking in the shallow crust below slow-spreading ridges.

6.2 Background on mechanical modeling

The oceanic lithosphere is assumed to be a continuous medium (e.g. Ranalli, 1995, see also section 1.3.1) in order to numerically simulate processes at seafloor spreading centers. Rheological or flow laws relate the deformation (strain) inside any material to the forces (stresses) acting on it (Ranalli, 1995). They are thus based on Newton's 2nd law of motion (section 1.3.1).

6.2.1 Stress and strain analysis

6.2.1.1 The stress tensor

In continuum mechanics **stress** σ is mathematically defined as force per unit area:

$$\sigma = f/A \quad (6.1)$$

and describes the distribution and intensity of forces at any point within a medium (Ranalli, 1995; Van der Pluijm and Marshak, 2003; Gerya, 2010). Since forces act in all three spatial dimensions stress is a tensor quantity with three vector entries for each dimension: two *shear stress* components τ acting parallel to a given surface and one *normal stress* σ_n , perpendicular to that surface (Fig. 6.2a). The stress state of an object can fully be described by a stress ellipsoid, which contains the three principle stresses ($\sigma_1 > \sigma_2 > \sigma_3$) (which are orthogonal to each other and orthogonal to three

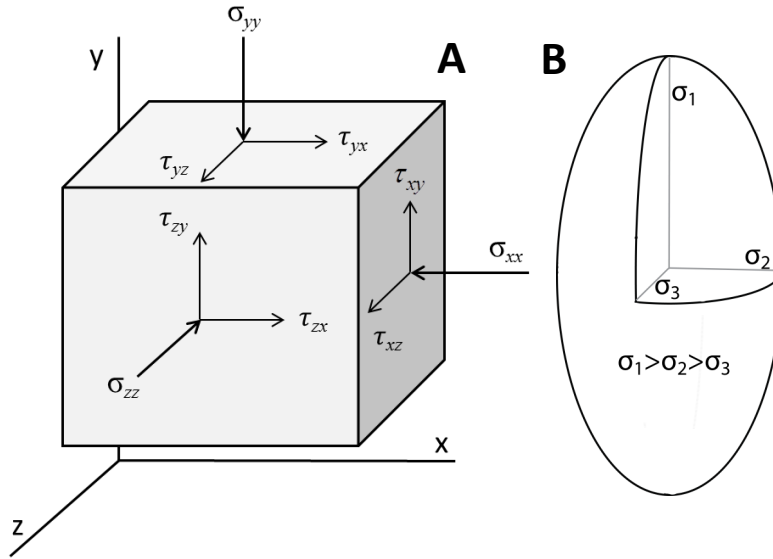


Figure 6.2: **A:** Three normal stress components (σ) perpendicular to the surfaces of the cube and six shear stress components (τ), which act parallel to the surfaces. **B:** The stress state of an object can be visualized by a stress ellipsoid, which has the three principal stresses as axes.

planes with zero shear stress) as axes (Fig. 6.2.b). If all principle stresses acting on one point inside a medium have the same magnitude the stress ellipsoid (Fig. 6.2b) describes a sphere and the stress state is called isotropic. The isotropic component of stress is also referred to as hydrostatic stress or pressure (strictly the pressure at the base of a water column). In nature the isotropic stress at depth caused by the column of overlying rocks (density times gravity times depth: ρgh) is called the lithostatic pressure. The mean stress or pressure σ_{mean} at one point inside a body can be defined in terms of the three normal stress components:

$$\sigma_{mean} = (\sigma_{xx} + \sigma_{yy} + \sigma_{zz})/3 \quad (6.2)$$

and equals the hydrostatic stress/pressure in case of a stationary medium.

Deviatoric stress σ' is defined as the remaining stress component after removal of the mean stress and contains the six shear stresses (e.g. Van der Pluijm and Marshak, 2003; Gerya, 2010)

$$\sigma'_{ij} = \sigma_{ij} - P\delta_{ij} \quad (6.3)$$

$\delta_{ij}=1$ if $i=j$ and $\delta_{ij}=0$, if $i \neq j$; indices i and j refer to spatial coordinates (x,y,z).

6.2.1.2 Deformation and strain

Stress acting on a body can result in its *deformation*, which describes the total displacement u of points in a body, e.g. (Van der Pluijm and Marshak, 2003). Deformation can include a *translation*, a movement from one place to another, a *rotation* around an axis, a *distortion*, which is a change in shape or a *dilation*, which are changes in area or volume (Fig. 6.3). *Strain* describes the displacement of points in a body relative to each other (Van der Pluijm and Marshak, 2003) (Fig. 6.4). The basic definition of strain, which is a dimensionless quantity, is:

$$\varepsilon = \frac{\Delta L}{L} \quad \underline{\underline{L}} \quad \underline{\underline{\Delta L}}$$

Figure 6.4: Strain illustration: ΔL is the change in length (displacement) of a line with original length L .

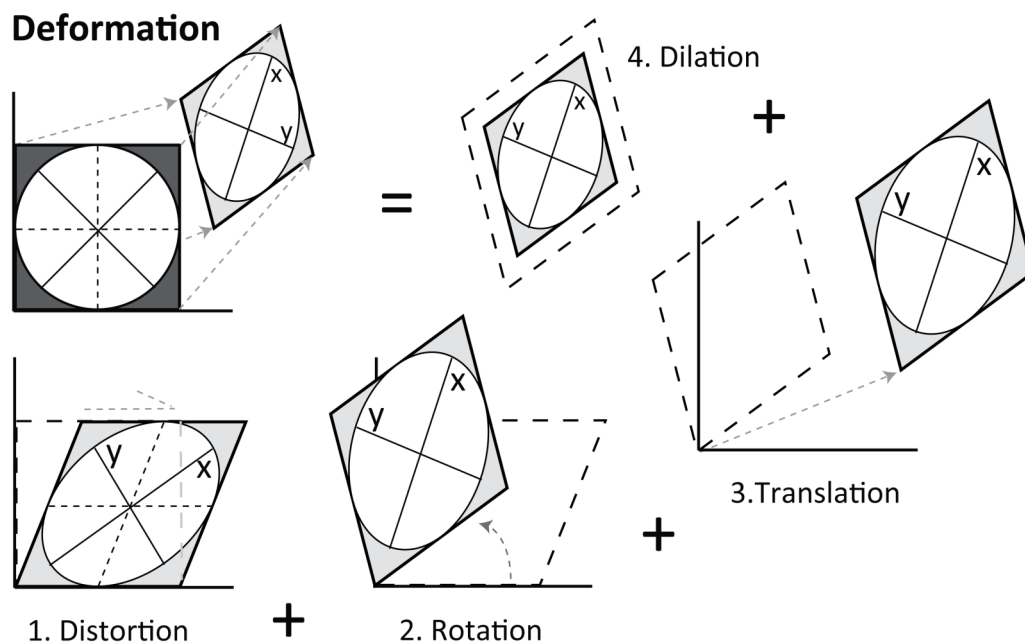


Figure 6.3: The deformation of the initially undeformed cube (dark grey) and circle can be described by the four independent components. The principle strain axes x and y (solid lines) of the strain ellipse are the lines of points which always remain perpendicular to each other during deformation (only valid for homogeneous strain). The dashed lines in the undeformed circle do not remain perpendicular to each other during deformation (see distortion). The length of the principle strain axes define the magnitude of strain in the respective direction.

Strain is thus a measure of the amount of deformation by distortion or by dilation. Strain by distortion (Fig. 6.3) can only be caused by the deviatoric stress component, which is the stress deviating from the stationary, hydrostatic stress state. Strain by dilation (Fig. 6.3) is caused by changes in the hydrostatic/lithostatic stress (pressure) component of the total stress applied to any material. Strain is considered homogeneous when two material lines remain perpendicular to each other before and after deformation. That means originally straight and parallel lines remain straight and parallel, e.g. during the deformation of a square to a rectangle or a sphere to an ellipsoid (Fig. 6.5a and b). During heterogeneous strain points in a body undergo varying amounts of strain (Fig. 6.5c and d). Homogeneous strain can be described by a strain ellipsoid, which in two dimensions consists of the two lines that remain perpendicular and are called principle strain axes (Fig. 6.3, 6.5a and b).

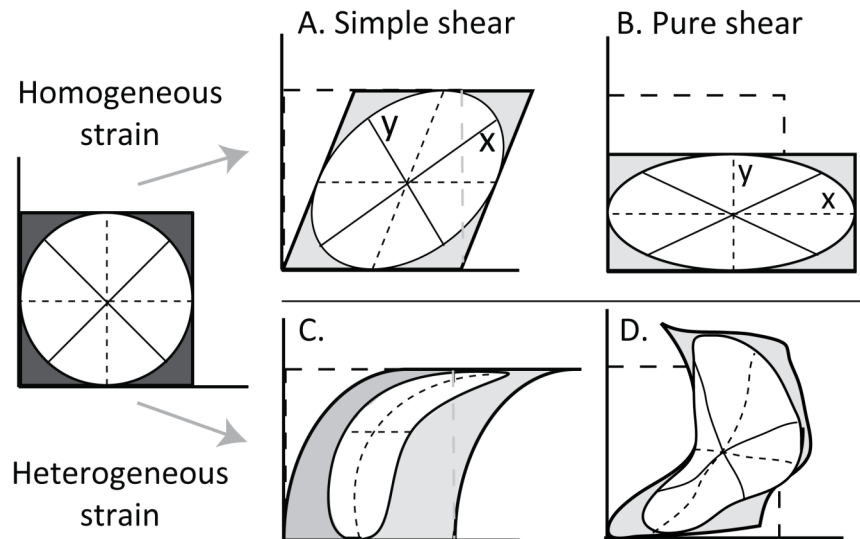


Figure 6.5: Illustration of homogeneous (A and B) and heterogeneous (C and D) strain. During homogeneous strain originally straight lines remain straight and originally parallel ones parallel. **A:** Strain is called non-coaxial (simple shear), when the principles strain axes (solid lines) rotate in comparison to the finite strain axes at the end of deformation. **B:** During pure shear or coaxial deformation the principle axes (dashed lines) remain their orientation throughout the deformation process. During heterogeneous strain material points experience varying amounts of strain and the initially straight lines do not remain straight (C and D).

The length of the principle strain axes defines the magnitude of strain in each direction. In analogy to stress, in strain analysis normal and shear strains are defined, corresponding to axial and shear deformation (e.g. Gerya, 2010). Strain is non-coaxial when the principle strain axes rotate relative to the finite strain axes at the end of deformation. Non-coaxial strain is also referred to as *simple shear*, where the length of the deformed body perpendicular to the shear surface remains constant e.g. the thickness of a deck of cards during shearing (see also distortion in Fig. 6.3 – and Fig. 6.5a). During coaxial strain accumulation (or *pure shear*) the principal strain axes maintain their orientation (Van der Pluijm and Marshak, 2003) (Fig. 6.5b). In analogy to the stress tensor, the 3D the full strain tensor ϵ_{ij} contains three normal (ϵ_{xx} , ϵ_{yy} , ϵ_{zz}) and six shear strain components ($\epsilon_{xy} = \epsilon_{yx}$, $\epsilon_{zx} = \epsilon_{xz}$, $\epsilon_{yz} = \epsilon_{zy}$) and is defined by:

$$\epsilon_{ij} = \frac{1}{2} \left(\frac{\partial u_i}{\partial x_j} + \frac{\partial u_j}{\partial x_i} \right) \quad (6.4)$$

where x_j and x_i refer to spatial coordinates (x,y,z), while i and j are coordinate indices referring to the direction in which displacement u is active. The time derivative of displacement u defines the velocity vector $v_i = (v_x, v_y, v_z) = \partial u / \partial t$.

The *strain rate* is defined as:

$$\dot{\epsilon}_{ij} = \frac{1}{2} \left(\frac{\partial v_i}{\partial x_j} + \frac{\partial v_j}{\partial x_i} \right) \quad (6.5)$$

and characterizes the dynamics of a deformation process, which is often more interesting than the total amount of deformation described by strain. The *deviatoric strain rate* is often used in geodynamic modeling, is achieved when the normal strain rates are subtracted from the total strain rate:

$$\dot{\epsilon}'_{ij} = \dot{\epsilon}_{ij} - \delta_{ij} \frac{1}{3} \dot{\epsilon}_{kk} \quad (6.6)$$

where kk are the indices of the normal strain rate components.

6.2.2 Rheology and deformation mechanisms in rocks

Materials show different types of behavior during deformation depending on the time scale and on the material properties at different P-T conditions (Ranalli, 1995; Jaeger et al., 2007). Crustal rocks show *brittle* behavior, which means that they can fail by fracture, at shallow levels and on short time scales. At greater depth and elevated temperatures lithospheric rocks behave *ductile*, which means that no brittle fracturing occurs (e.g. Turcotte and Schubert, 2002) and Fig. 6.6).

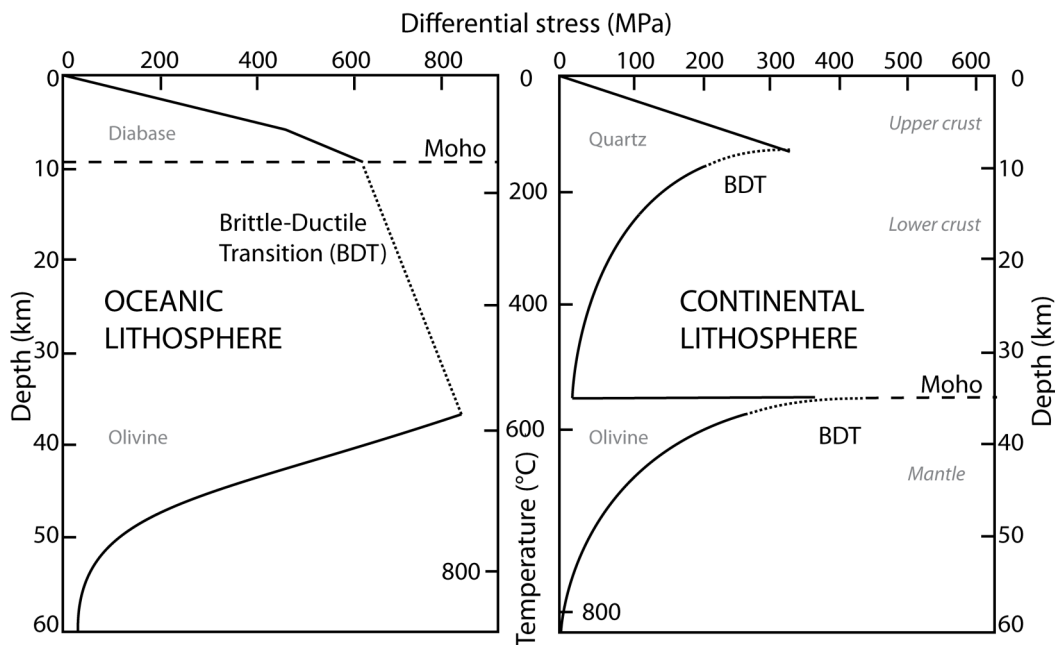


Figure 6.6: Strength envelopes for oceanic and continental lithosphere modified after Kohlstedt et al., (1995). Deformation occurs when the differential stress exceeds the maximum strength of the rocks. The BDT marks the region between brittle and ductile response of the rocks to applied stress (dotted lines). An oceanic geotherm corresponding to 60 million years old lithosphere is used and a dry olivine rheology. For the continental case wet rheologies are applied and a geotherm for a surface heat flow of 60mW m^{-1} . In the continental lithospheric mantle a second BDT occurs due to the compositional change to olivine rheology.

6.2.2.1 Viscous flow

On geological time scales deforming lithospheric rocks behave like viscous fluids (e.g. Turcotte and Schubert, 2002; Gerya, 2010). Perfectly viscous materials deform instantaneously and continuously under applied forces (Fig. 6.7), like e.g. a liquid as water. Viscous deformation is non-reversible (Fig. 6.7). The rheological relation between shear stress τ and the resulting shear strain rate of a viscous fluid is expressed in Newton's law of viscous friction:

$$\tau = 2\eta\dot{\epsilon} \quad , \quad (6.7)$$

where η is viscosity, which is a measure of a materials resistance to shear deformation. Viscosity differs between materials and can be dependent on parameters as e.g. temperature, pressure and strain rate. In terms of deviatoric stress (Equ. 6.3) and deviatoric strain rate (Equ. 6.6) the 3D law of viscous friction can be expressed as:

$$\sigma_{ij}' = 2\eta\dot{\epsilon}'_{ij} + \eta_{bulk}\delta_{ij}\frac{1}{3}\dot{\epsilon}'_{kk} \quad (6.8)$$

where η and η_{bulk} are shear viscosity and bulk viscosity respectively. The volumetric bulk strain rate is defined by the sum of normal strain rate components:

$\dot{\epsilon}'_{kk} = (\dot{\epsilon}_{xx} + \dot{\epsilon}_{yy} + \dot{\epsilon}_{zz}) = div(\vec{v})$, which is also equal to the divergence of the velocity vector (see Equ.6.5) and can cause volume changes of a body.

6.2.2.2 Elastic deformation

On shorter time scales most rocks at room temperature and atmospheric pressure show a brittle behavior (Ranalli, 1995; Turcotte and Schubert, 2002). They behave elastically until they fail by fracture (Turcotte and Schubert, 2002). By definition any elastic deformation in a material is occurring instantaneous when stress is applied and is fully recoverable (Ranalli, 1995) and Fig. 6.7) as e.g. the deformation

of an elastic rubber band. Hooke's law describes elastic deformation and relates applied stress to resulting elastic strain:

$$\boldsymbol{\sigma} = 2G\boldsymbol{\varepsilon} \quad (6.9)$$

Assuming 2D plane strain ($\boldsymbol{\varepsilon}_{zz}=0$), we obtain:

$$\sigma_{ij} = 2G\varepsilon_{ij} + \lambda\delta_{ij}\varepsilon_{kk} \quad (6.10)$$

λ and G are Lamé's constants, which are material properties (which in fact are not constant but depend on e.g. temperature and pressure). The Lamé constant G is also called shear modulus or Rigidity.

6.2.2.3 Visco-elastic rheology

Natural materials like e.g. rocks typically show a complex rheological behavior under applied forces, where several deformation modes can be active at the same time. A material that responds to an applied deviatoric stress with both viscous and elastic deformation is referred to as viscoelastic or Maxwell body (Fig. 6.8) (Ranalli, 1995; Turcotte and Schubert, 2002; Gerya, 2010). In a Maxwell material elastic deformation is dominating on short time scales while viscous deformation dominates on long ones. Graphically the viscous and elastic deformation modes active in a Maxwell material are combined in series to represent the timely order in which the respective deformation mode is dominating (Fig. 6.8). Elastic deformation occurs instantaneously at loading (t_0) and is followed by steady-state linear viscous deformation. When forces are removed (t_1) only the elastic strain is recovered (Fig. 6.8). A so called firmoviscous material or Kelvin body shows elastic afterworking (Ranalli, 1995; Turcotte and Schubert, 2002). Viscous and elastic deformation mechanisms are graphically represented parallel. If we look at the strain-time relation of a Kelvin body it can be seen that the elastic response upon loading is delayed by the viscous deformation. After unloading the strain exponentially approaches zero (Fig. 6.8).

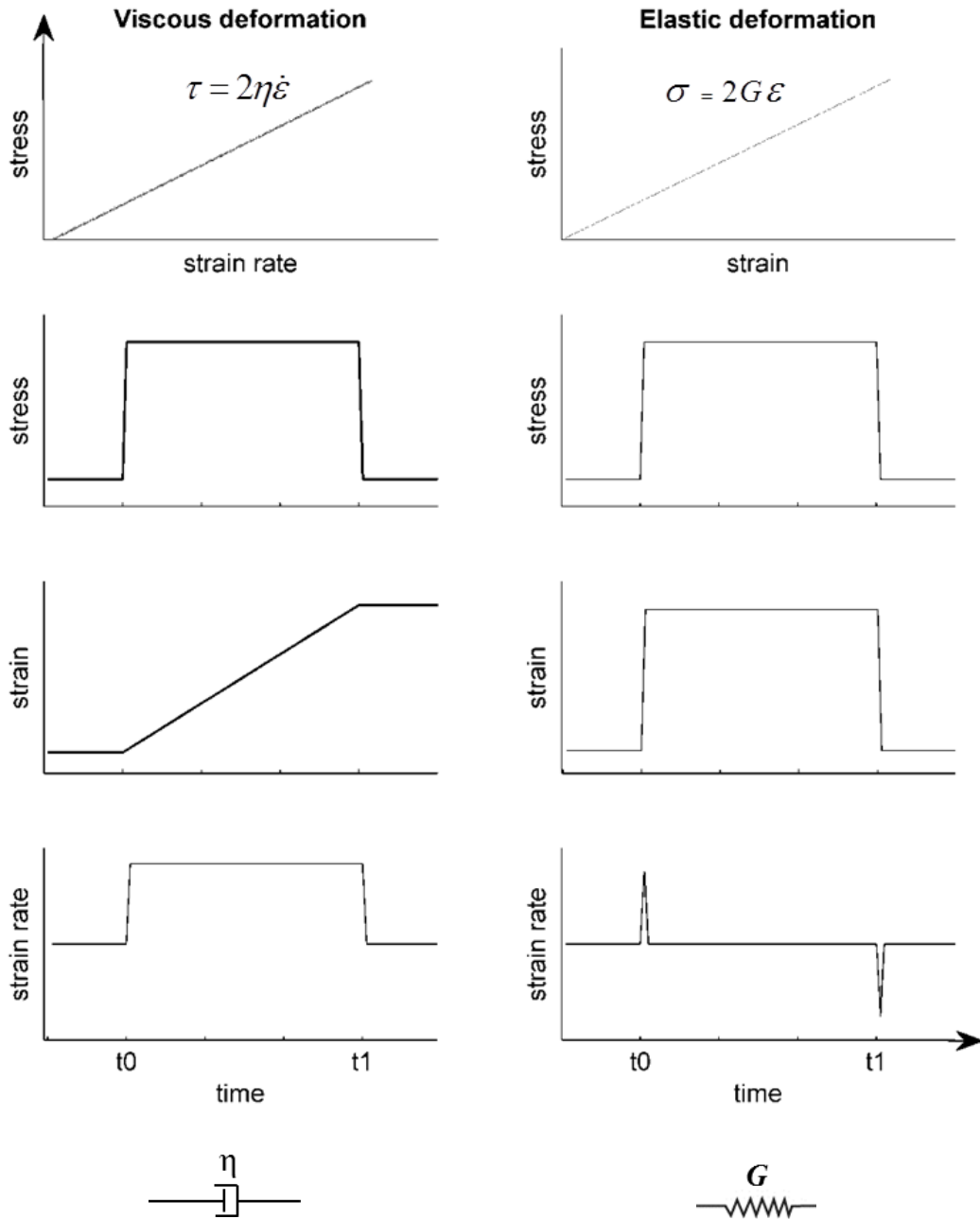


Figure 6.7: Stress-strain and time relations for viscous flow and elastic deformation. Viscous deformation occurs instantaneously and continuously from the time of loading (t_0) and is not recovered at unloading (t_1). Also elastic deformation is occurring instantaneously at loading and the full strain is reached immediately. It is fully recoverable (see strain at time of unloading (t_1)).

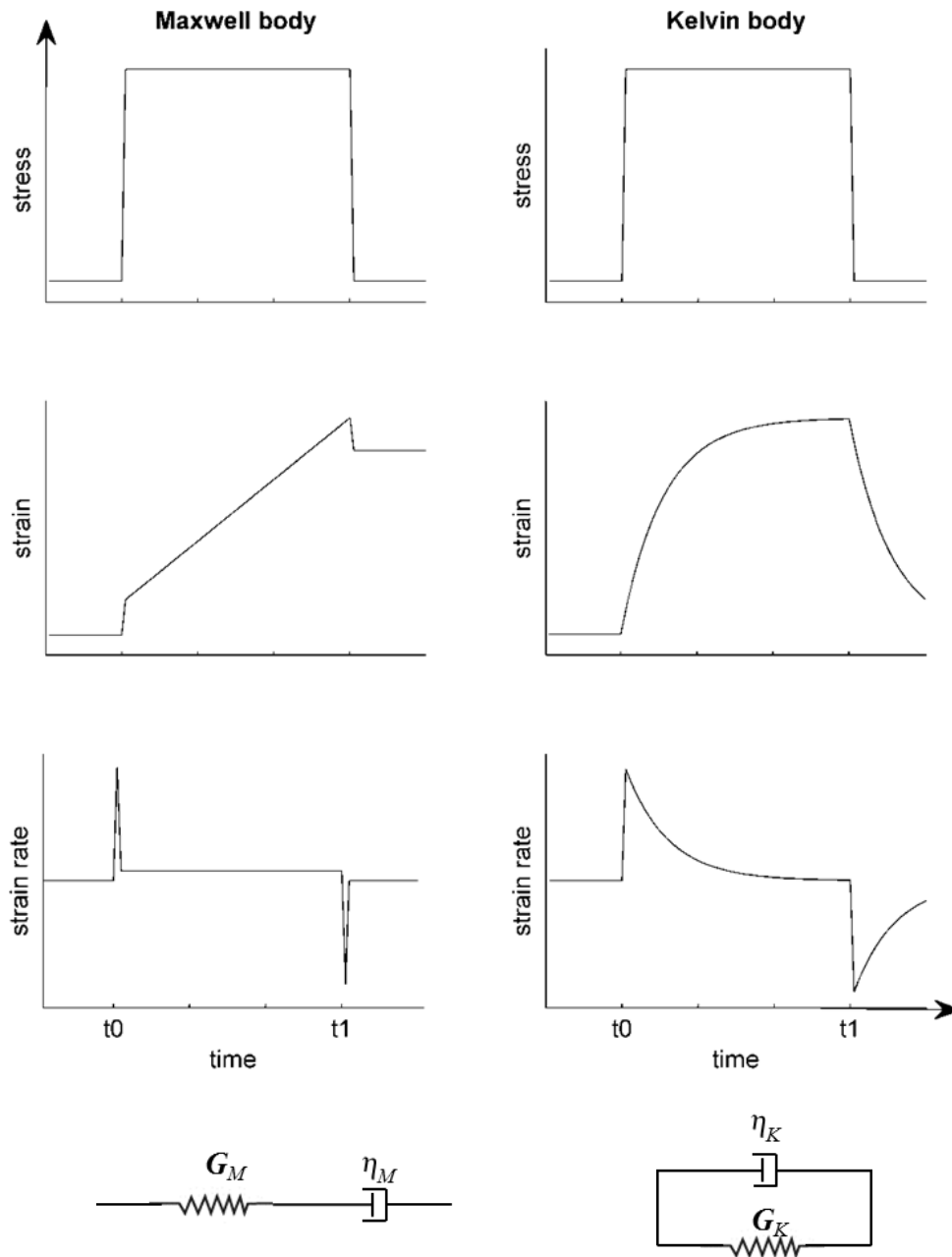


Figure 6.8: Illustration of visco-elastic behavior: in a Maxwell body the elastic part of the strain is recovered after the stress is removed at unloading (t_0). Elastic deformation is dominating on short- and viscous deformation on long time-scales. In a firmo-viscous Kelvin material the direct elastic response (strain) of the material is delayed by the viscous forces.

6.2.2.4 Plasticity

Plastic deformation does not occur until a certain stress threshold is reached (Fig. 6.9) and is non-reversible. Plastic deformation follows elastic deformation and sets in when the stress acting on a material exceeds its yield strength. Plastic deformation is thus occurring as fracture failure under brittle conditions and as plastic flow in the ductile regime. The behavior of materials under low temperature conditions during brittle plastic deformation is described by failure criterions like e.g. the Mohr-Coulomb yield criterion (Fig. 6.9) (Ranalli, 1995; Davis and Selvadurai, 2005; Jaeger et al., 2007; Kaus, 2010):

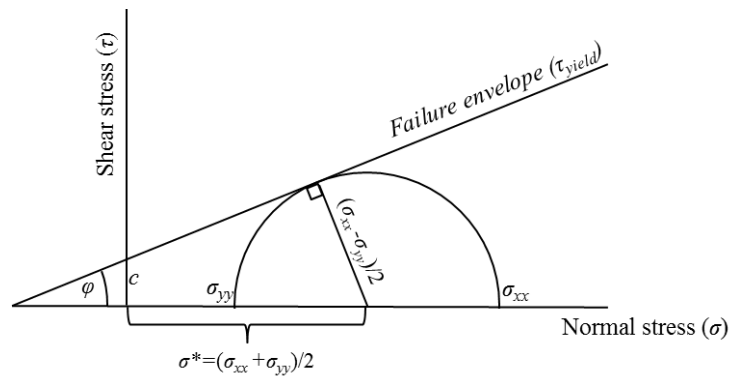
$$\begin{aligned} F &= \tau^* - \sigma^* \sin(\varphi) + c \cos(\varphi) & (6.11a \text{ and } b) \\ Q &= \tau^* - \sigma^* \sin(\psi) \end{aligned}$$

F defines the yield function, Q the plastic flow potential, c , φ and ψ are material parameters cohesion, friction and dilation angle respectively. σ^* is the mean stress (pressure, Equ. 6.2, Fig. 6.9). Plastic deformation occurs when $F > 0$, which is when the maximum shear stress τ^* :

$$\tau^* = \sqrt{\left(\frac{\sigma_{xx} - \sigma_{yy}}{2}\right)^2 + \sigma_{xy}^2} \quad (6.12)$$

exceeds the yield stress: $\tau_{yield} = \sigma^* \sin(\varphi) + c \cos(\varphi)$ (6.13)

Figure 6.9: Mohr-Coulomb failure criterion. The radius of the circle is described by the maximum shear stress acting on a body. If it exceeds the yield strength, the material will fail by fracture.



References Cited

- Baker, E. T., and German, C. R., 2004, On the global distribution of hydrothermal vent fields, *in* German, C. R., Lin, J., and Parson, M., eds., *Mid-Ocean Ridges: Hydrothermal Interactions Between the Lithosphere and Oceans*, Volume Geophysical Monograph Series: Washington, DC, American Geophysical Union, p. 245 - 266.
- Davis, R. O., and Selvadurai, A. P. S., 2005, *Plasticity and Geomechanics*, Cambridge University Press, 287 p.:
- Detrick, R. S., Mutter, J. C., Buhl, P., and Kim, I. I., 1990, No evidence from multichannel reflection data for a crustal magma chamber in the MARK area on the Mid-Atlantic Ridge: *Nature*, v. 347, no. 6288, p. 61-64.
- German, C. R., and Lin, J., 2004, The Thermal Structure of the Oceanic Crust, Ridge-Spreading and Hydrothermal Circulation: How Well Do We Understand Their Inter-Connections?, *Mid-Ocean Ridges: Hydrothermal Interactions Between the Lithosphere and Oceans*, Volume Geophysical Monograph 148, AGU.
- Gerya, T., 2010, *Introduction to Numerical Geodynamic Modelling*, New York, Cambridge University Press.
- Hannington, M. D., De Ronde, C. E. J., and Petersen, S., 2005, Sea-Floor Tectonics and Submarine Hydrothermal Systems, *in* Hedenquist, J. W., Thompson, J. F. H., Goldfarb, R. J., and Richards, J. P., eds., *Economic Geology: One Hundredth Anniversary Volume*, Volume 1: Littleton, Colorado, Economic Geology, p. 111-141.
- Hess, H., 1962, History of ocean basins, *in* Engel, A. E. J., James, L. J., and Leonard, B. F., eds., *Volume Petrologic studies: a volume in honor of A. F. Buddington*: Boulder, Geological Society of America.
- Jaeger, J. C., Cook, N. G. W., and Zimmerman, R. W., 2007, *Fundamentals of rock mechanics*, Blackwell Publishing, 475 p.:
- Kaus, B. J. P., 2010, Factors that control the angle of shear bands in geodynamic numerical models of brittle deformation: *Tectonophysics*, v. 484, no. 1-4, p. 36-47.
- Kohlstedt, D. L., Evans, B., and Mackwell, S. J., 1995, Strength of the lithosphere - constraints imposed by laboratory experiments: *Journal of Geophysical Research-Solid Earth*, v. 100, no. B9, p. 17587-17602.
- Macdonald, K. C., 1982, Mid-Ocean Ridges - fine scale tectonic, volcanic and hydrothermal processes within the plate boundary zone: *Annual Review of Earth and Planetary Sciences*, v. 10, p. 155-190.
- Macdonald, K. C., 1998, Linkages Between Faulting, Volcanism, Hydrothermal Activity and Segmentation on Fast Spreading Centers, *Faulting and Magmatism at Mid-Ocean Ridges*, American Geophysical Union, p. 27-58.
- Macdonald, K. C., 2001, Mid-Ocean Ridge Tectonics, Volcanism, and Geomorphology, *Encyclopedia of Ocean Sciences*, p. 852-866.
- Menard, H. W., 1967, Sea Floor Spreading, Topography, and the Second Layer: *Science*, v. 157, no. 3791, p. 923-924.
- Morgan, J. P., and Chen, Y. J., 1993a, Dependence of ridge-axis morphology on magma supply and spreading rate: *Nature*, v. 364, no. 6439, p. 706-708.
- Morgan, J. P., and Chen, Y. J., 1993b, The Genesis of Oceanic Crust: Magma Injection, Hydrothermal Circulation, and Crustal Flow: *J. Geophys. Res.*, v. 98, no. B4, p. 6283-6297.

- Perfit, M. R., and Chadwick, W. W., 1998, *Magmatism at Mid-Ocean Ridges: Constraints from Volcanological and Geochemical Investigations, Faulting and Magmatism at Mid-Ocean Ridges*, American Geophysical Union, p. 59-115.
- Ranalli, G., 1995, *Rheology of the earth*, Chapman & Hall, 413 p.:
- Sigurdsson, H., and Houghton, B. F., 2000, *Encyclopedia of Volcanoes*, Academic Press.
- Singh, S. C., Crawford, W. C., Carton, H., Seher, T., Combier, V., Cannat, M., Pablo Canales, J., Dusunur, D., Escartin, J., and Miguel Miranda, J., 2006, Discovery of a magma chamber and faults beneath a Mid-Atlantic Ridge hydrothermal field: *Nature*, v. 442, no. 7106, p. 1029-1032.
- Sinton, J. M., and Detrick, R. S., 1992, Mid-ocean ridge magma chambers: *Journal of Geophysical Research: Solid Earth*, v. 97, no. B1, p. 197-216.
- Small, C., 1998, *Global Systematics of Mid-Ocean Ridge Morphology, Faulting and Magmatism at Mid-Ocean Ridges*, American Geophysical Union, p. 1-25.
- Turcotte, D. L., and Schubert, G., 2002, *Geodynamics* New York, Cambridge University Press, 456 p.
- Van der Pluijm, B. A., and Marshak, S., 2003, *Earth Structure: An Introduction to Structural Geology and Tectonics*, Norton and Company, 672 p.:
- Vine, F. J., 1966, Spreading of the Ocean Floor: New Evidence: *Science*, v. 154, no. 3755, p. 1405-1415.
- Vine, F. J., and Matthews, D. H., 1963, Magnetic Anomalies Over Oceanic Ridges: *Nature*, v. 199, no. 4897, p. 947-949.

7 Seafloor spreading under varying tectono-magmatic conditions

Christine Andersen, Lars Rüpke and Jörg Hasenclever*

GEOMAR, Helmholtz Centre for Ocean Research Kiel, Germany

Abstract

The deformation of oceanic lithosphere during seafloor spreading with varying degrees of magma supplied to the ridge axis have been investigated with a fully 2D visco-elasto-plastic mechanical model. Fracturing in the brittle regions is modelled applying a Mohr-Coulomb yield criterion.

When the accretion of new oceanic crust is dominated by magmatic activity deformation, represented by elevated strain rates, is focused to the axial region of the ridge. No region of the model domain exceeds the yield stress, such that no brittle deformation is occurring. The rheology is thus visco-elastic and initial cohesion and viscosity are not modified. When the supply of magma to the ridge axis is low tectonic processes are dominating and crustal thinning is increasing. The rheological behavior of the oceanic crust is now visco-elasto-plastic. Deformation focuses into off-axis shear bands that dip towards the ridge axis. Those bands show elevated strain rates, decreased viscosity and cohesion as a result of plastic failure in the brittle crust.

If high strain rates are translated into highly deforming regions the results from the mechanical model simulations can be used as powerful tool to predict the permeability structure of the oceanic crust under varying tectono-magmatic conditions. A crustal permeability with little heterogeneities and deformation focused to the axial region would be the result of the high magma supply to fast-spreading ridges. A faulted crust with a highly heterogeneous permeability structure and zones of off-axis deformation would be the result of the low magma supply in slow-spreading environments.

*Paper in preparation

7.1 Background

In order to test the key hypothesis of this work, stating that the tectono-magmatic state of slow-spreading ridges controls the position of hydrothermal vent fields, the results of lithosphere dynamics modeling should be combined with hydrothermal convection models. The dynamics of crustal genesis (e.g. Sleep, 1975; Phipps Morgan and Chen, 1993; Quick and Denlinger, 1993) and feedbacks between crustal accretion and hydrothermal cooling at fast-spreading ridges have been explored by several numerical studies (Cherkaoui et al., 2003; Iyer et al., 2010; Theissen-Krah et al., 2011). Less work has been done for slow-spreading ridges, which show a more complex crustal structure (see also section 6.1). Due to a generally lower magma supply to the ridge axis in slow-spreading conditions, the ocean crust formed there is colder. There the crust behaves brittle and the formation of tectonic faults on different scales is dominating. This complexity and the fact that slow-spreading ridges are most likely not in steady-state presents a severe challenge for numerical models. Nevertheless several numerical studies have investigated modes of faulting at oceanic spreading centers using visco-elasto-plastic mechanical models that account for melt injection (Buck et al., 2005; Behn and Ito, 2008; Ito and Behn, 2008; Tucholke et al., 2008; Olive et al., 2010). They all found a clear control of melt supply on deformation mode. Tucholke et al. (2008) describe the interactions between magma supply and the faulting pattern of an oceanic detachment: if extension is fully balanced by the injected melt, deformation is focused on the axial region. This scenario possibly applies to magmatic segments of slow-spreading ridges. If the magma supply to the ridge is too low to fully accommodate the extension of the plates, deformation shifts off-axis, possibly applying to tectonic segments. These results agree well with our hypothesis about the ridge segment hosting the LHF currently being in a tectonic phase. The observed off-axis seismicity at LHF1 is fully compatible with the off-axis deformation predicted by the above models.

If we assume that highly deforming regions are also highly permeable we can relate deformation to the likely permeability structure of the lithosphere, which is a clear step forward. Off-axis venting would then be a direct consequence of off-axis deformation – as e.g. suggested for the Logatchev segment. This leads us to believe that the combination and coupling of lithosphere dynamics models for oceanic ridges with hydrothermal convection models will mark a crucial step forward in our understanding of seafloor spreading processes at ridges at different spreading rates. To our knowledge, no such combined numerical study has been conducted previously. Here results from visco-elasto-plastic simulations of ridges under varying tectono-magmatic conditions are presented. The here presented mechanical model provides a major advance for the coupling of lithosphere dynamics models with hydrothermal flow modelling. The final step marks the prediction of permeability from the obtained lithospheric deformation field, which can be used as input for hydrothermal convection models as in chapter 4 and 5.

7.2 Mechanical model

During the numerical simulations deforming rocks of the oceanic lithosphere are treated as a Maxwell visco-elasto-plastic continuous material. Fracturing in the upper brittle regime of the lithosphere is modelled applying a Mohr-Coulomb yield criterion (see e.g. Kaus, 2010 and section 6.2.2.3). Prior to yielding rocks are assumed to show a purely viscous or visco-elastic (Maxwell) behavior (see section 6.2.2.1 and 6.2.2.4). It is still not entirely clear which of the two rheologies shall be applied to non-yielded materials (see e.g. numerical results in Kaus, 2010). It seems to be confirmed that rocks behave elastically on small time-scales and at small strains (Ranalli, 1995 and section 6.2.2 above). If we are however interested in modeling brittle failure along fractures elastic deformation on short time scales might play a minor role and could be neglected. Moreover it has previously been shown that results obtained by visco-plastic or full visco-elasto-plastic codes differed little (Buiter et al., 2006; Kaus, 2010).

7.2.1 Governing equations

Volume changes in rocks are caused by changes in density, which are due to mineralogical phase transformations. On long time scales, that we are simulating, where viscous deformation is dominating, rocks are assumed to undergo relatively small density variations and compressibility is thus negligible. Therefore, in geodynamic models, rocks are often approximated by an incompressible fluid with constant density (e.g. Gerya, 2010), where the bulk strain rate equals zero:

$$\dot{\mathcal{E}}_{bulk} = \text{div}(\vec{v}) = 0 \quad (7.1)$$

In this case the deviatoric and total strain rates are equal (see Equ. 6.6) and the 3D law of viscous friction (Equ. 6.8) simplifies to:

$$\sigma_{ij}' = 2\eta\dot{\mathcal{E}}'_{ij} \quad (7.2)$$

and elastic deformation (Equ. 6.10) is expressed by:

$$\sigma_{ij}' = 2G\mathcal{E}'_{ij} \quad (7.3)$$

In a Maxwell material (section 6.2.2.3), different deformation modes are assumed to be active at the same time, such that strain rates are additive. The total deviatoric strain rate is thus composed out of the sum of the deviatoric viscous, elastic and plastic strain rate components:

$$\dot{\mathcal{E}}'_{total} = \dot{\mathcal{E}}'_{viscous} + \dot{\mathcal{E}}'_{elastic} + \dot{\mathcal{E}}'_{plastic} \quad (7.4)$$

The elastic deviatoric strain rate is expressed using equation 7.3 and a time derivative of deviatoric stress:

$$\dot{\mathcal{E}}'_{elastic} = \frac{1}{2G} \frac{\tilde{D}\sigma_{ij}'}{\tilde{D}t} \quad (7.5)$$

The time derivative is called *Jaumann stress rate* and includes a solid body rotation:

$$\frac{\check{D}\sigma'_{ij}}{\check{D}t} = \frac{\partial\sigma'_{ij}}{\partial t} + v_k \frac{\partial\sigma'_{ij}}{\partial xk} - W_{ik}\sigma'_{kj} + \sigma'_{ik}W_{kj}, \quad (7.6)$$

with: $W_{ij} = \frac{1}{2} \left(\frac{\partial v_i}{\partial x_j} - \frac{\partial v_j}{\partial x_i} \right)$ being the vorticity.

From equation 7.2 we get the viscous strain rate and can express the total deviatoric strain rate as:

$$\dot{\mathcal{E}}'_{total} = \frac{\sigma'_{ij}}{2\eta} + \frac{1}{2G} \frac{\check{D}\sigma'_{ij}}{\check{D}t} + \gamma \frac{\sigma Q}{\partial\sigma_{ij}}, \quad (7.7)$$

where γ is the plastic multiplier, which is a material parameter and Q the plastic flow potential (Equ. 6.11b).

The flow of a viscous fluid in response to applied forces is derived from balancing stresses on a control volume (conservation of momentum also called *Navier-Stokes equation*) and is a differential form of Newton's second law of motion (section 1.3.1):

$$\frac{\partial\sigma_{ij}}{\partial x_j} + \rho g_i = \rho \frac{Dv_i}{Dt}, \quad (7.8)$$

where g_i is the gravity vector and Dv_i/Dt the acceleration of an object.

The stress balance (equation 7.8) is rewritten in terms of deviatoric stress (Equ. 6.3) which introduces pressure into the equation. For slowly deforming, highly viscous fluids the inertial acceleration can be neglected ($Dv_i/Dt=0$, *Stokes flow*). The gravity term ρg_i acts only in the vertical direction. For the x- and y-direction respectively in 2D we obtain:

$$\begin{aligned}\frac{\partial \sigma_{xx}'}{\partial x} + \frac{\partial \sigma_{xy}'}{\partial y} - \frac{\partial P}{\partial x} &= 0 \\ \frac{\partial \sigma_{yy}'}{\partial y} + \frac{\partial \sigma_{yx}'}{\partial x} - \frac{\partial P}{\partial y} &= -\rho g\end{aligned}\tag{7.9}$$

7.2.2 Numerical formulation

Incompressibility: $\dot{\mathcal{E}}_{bulk} = \nabla \cdot \mathbf{v} = 0$ (section 7.2.1) during viscous deformation is numerically applied by dividing pressure P by a so called penalty factor λ , which is a very large constant such that the term becomes almost zero:

$$\nabla \cdot \mathbf{v} = \frac{P}{\lambda} \approx 0\tag{7.10}$$

In order to simulate the supply of magma to a Mid-Ocean ridge (Fig. 6.1), a dilation region is introduced in the vicinity of the ridge axis, which shall represent an area of incoming material, transported by sheeted dikes and pillow lavas. Since material is added the dilation region is compressible and the governing equation 7.10 above modifies to:

$$\nabla \cdot \mathbf{v} - \frac{P}{\lambda} = \psi\tag{7.11}$$

where ψ is the dilation term defined by:

$$\psi = v_s \frac{h_{crust}}{A_{dilation}}\tag{7.12}$$

where v_s is the spreading rate of the tectonic plate, h_{crust} the height of the oceanic crust and A_{dikes} the area (in 2D) of the dilation region. If the dilation term equals one, seafloor spreading is fully balanced by the amount of oceanic crust formed by the incoming magma, such that the crust is keeping its constant height. If less magma is supplied to the ridge axis ($\psi^* \xi$; $\xi < 1$), the crust experiences thinning and

brittle, tectonic deformation is becoming increasingly important (see section 6.2.2).

In order to solve equation 7.7 numerically the elastic time derivative (Equ. 7.6) is discretized:

$$\frac{\partial \sigma_{ij}'}{\partial t} = \frac{\sigma_{ij}'_{new} - \sigma_{ij}'_{old}}{\Delta t} \quad (7.13)$$

and equation 7.7 rewritten as:

$$\dot{\epsilon}'_{total} = \frac{1}{2\eta} \sigma_{ij}' + \frac{1}{2G} \frac{\sigma_{ij}'_{new} - \sigma_{ij}'_{old}}{\Delta t} + \dot{\epsilon}'_{plastic} \quad (7.14)$$

We can bring all unknown stress terms on one side:

$$\sigma_{ij}' = 2\mu_{ve}(\dot{\epsilon}'_{total} - \dot{\epsilon}'_{plastic}) + X\sigma_{ij}'_{old*} \quad (7.15)$$

is $\mu_{ve} = \frac{1}{\frac{1}{\eta} + \frac{1}{G\Delta t}}$ the visco-elastic viscosity and $X = \frac{1}{1 + \frac{\eta}{G\Delta t}}$

If the elastic shear modulus G is becoming very large $\mu_{ve} \rightarrow \eta$ and $X \rightarrow 0$ which is the case for purely viscous deformation. We are then back to the law of viscous friction for an incompressible fluid (Equ. 6.8): $\sigma_{ij}' = 2\eta\dot{\epsilon}'$

Since elastic deformation is reversible, deviatoric elastic stresses ($\sigma_{ij}'_{old*}$) are saved from each previous time step and drop out in case of purely viscous flow. Solid body rotation is applied to elastic stresses and we obtain following expression for the old stress from the previous time-step:

$$\sigma_{ij}'_{old*} = \sigma_{ij}'_{old} + \nu_{k_old} \frac{\partial \sigma_{ij}'_{old}}{\partial x_k} - W_{ik} \sigma_{kj}'_{old} + \sigma_{ik}'_{old} W_{kj} \quad (7.16)$$

Equ. 7.15 can be written in terms of invariants of the deviatoric stress and strain tensors: and $\sigma_{II}' = \sqrt{(0.5\sigma_{ij}')^2}$ $\dot{\epsilon}_{II}' = \sqrt{(0.5\dot{\epsilon}'_{ij})^2}$

(where ij implies a summation over all deviatoric components), which characterize

the local deviation of stresses from the hydrostatic stress state and the deformation caused by those, as. The full rheology includes an effective visco-elasto-plastic viscosity and the total strain rate includes all three deformation modes that can be active:

$$\sigma_{ij}' = 2\mu_{vep}\dot{\epsilon}_{II} + X\sigma_{IIold}^* \quad (7.17)$$

$$\mu_{vep} = \begin{cases} \frac{\sigma_{ij}' - X\sigma_{IIold}^*}{2\dot{\epsilon}_{II}} & \text{if } (F > 0) \\ \mu_{ve} & \text{if } (F < 0) \end{cases} \quad (7.18)$$

From the force balance equation (Equ. 7.9) in combination with the rheological expression for deviatoric stress (Equ. 7.17) and the basic definition of strain rate (Equ. 6.5), we obtain the final governing equation for 2D stokes flow:

$$\begin{aligned} \frac{\partial}{\partial x} \left(2\mu_{vep} \left(\frac{\partial v_x}{\partial x} \right) \right) + \frac{\partial}{\partial y} \left(\mu_{vep} \left(\frac{\partial v_y}{\partial x} + \frac{\partial v_x}{\partial y} \right) \right) - \frac{\partial P}{\partial x} = \\ -X \left(\frac{\partial \sigma_{xx}'_{old}}{\partial x} + \frac{\partial \sigma_{xy}'_{old}}{\partial y} \right) \rightarrow x\text{-direction} \\ \frac{\partial}{\partial y} \left(2\mu_{vep} \left(\frac{\partial v_y}{\partial y} \right) \right) + \frac{\partial}{\partial x} \left(\mu_{vep} \left(\frac{\partial v_y}{\partial x} + \frac{\partial v_x}{\partial y} \right) \right) - \frac{\partial P}{\partial y} = \\ -X \left(\frac{\partial \sigma_{yy}'_{old}}{\partial y} + \frac{\partial \sigma_{yx}'_{old}}{\partial x} \right) - \rho g \rightarrow y\text{-direction} \end{aligned} \quad (7.19)$$

Equation 7.19 leads to the matrix system of equations, which is solved in each numerical step:

$$\begin{aligned}
 & \begin{bmatrix} \frac{\partial}{\partial x} & 0 & \frac{\partial}{\partial y} \\ 0 & \frac{\partial}{\partial y} & \frac{\partial}{\partial x} \end{bmatrix} \begin{bmatrix} 2\mu_{vep} & 2\mu_{vep} & 0 \\ 2\mu_{vep} & 2\mu_{vep} & 0 \\ 0 & 0 & \mu_{vep} \end{bmatrix} \begin{bmatrix} \frac{\partial}{\partial x} & 0 \\ 0 & \frac{\partial}{\partial y} \\ \frac{\partial}{\partial y} & \frac{\partial}{\partial x} \end{bmatrix} \begin{bmatrix} v_x \\ v_y \end{bmatrix} - \begin{bmatrix} \frac{\partial P}{\partial x} \\ \frac{\partial P}{\partial y} \end{bmatrix} = \\
 & - \begin{bmatrix} \frac{\partial}{\partial x} & 0 & \frac{\partial}{\partial y} \\ 0 & \frac{\partial}{\partial y} & \frac{\partial}{\partial x} \end{bmatrix} \begin{bmatrix} X & 0 & 0 \\ 0 & X & 0 \\ 0 & 0 & X \end{bmatrix} \begin{bmatrix} \sigma_{xx'} \\ \sigma_{yy'} \\ \sigma_{xy'} \end{bmatrix}^{old} - \begin{bmatrix} 0 \\ \rho g \end{bmatrix}
 \end{aligned} \tag{7.20}$$

7.2.2.1 Numerical scheme

The governing equation 7.20 is solved in each numerical time-step to retrieve new crustal velocities (v_x and v_y) from which a new stress field and respective visco-elasto-plastic viscosities can be calculated. We use a 2D FEM approach (see section 1.3.3) with triangular elements that form an unstructured mesh, which is deformed by advecting nodal grid points with the respective velocities in each numerical step. Once the mesh becomes too strained (triangles become too deformed) a remesh is performed allowing to continue the calculation with the current geometry of the model domain on a new mesh. At the beginning of each time-step rheology is assumed to be visco-elastic and therefore the total strain rate does not include any strain caused by plastic deformation ($\dot{\mathcal{E}}'_{plastic} = 0$). Maximum shear stress τ^* is below the yield stress and the yield function is below zero ($F < 0$, Equ. 6.11 and Fig. 6.9). In the end of each numerical time step is checked where the shear stresses exceed the yield stress ($F > 0$), which implies that plastic deformation is active and the plastic strain rate non-zero ($\dot{\mathcal{E}}'_{plastic} \neq 0$). In areas where $F > 0$ stresses have to be brought back on the yield surface such that $F = 0$. This is done by computing the visco-elasto-plastic viscosity μ_{vep} (Equ. 7.18) for the regions where plastic failure is occurring. A change in local viscosity has an effect on the stress state of surrounding

points, which is why plasticity iterations have to be carried out until a viscosity distribution is reached where no stresses are exceeding the yield stress and correct plastic strain rates can be computed. In every iteration step i an error ep_i is computed as:

$$ep_i = \frac{|v_i - v_{i-1}|}{|v_i|}, \quad (7.21)$$

where v_i are nodal velocities. Iterations are typically terminated when $ep_i < 10^{-5}$ or more than 30 iteration steps have been performed (see also Kaus, 2010).

Some materials experience an increase or decrease in stress after the onset of deformation processes/strain. Strain softening e.g. is referred to when a material is more easily strained in areas where it has experienced previous deformation and stress is thus reduced faster. In modeling of geodynamic processes as e.g. the deformation of tectonic plates it is common to include strain softening, which leads to strain localization (Gueydan et al., 2014). We include strain softening by modifying cohesion c of the rocks in each time step according to:

$$c = c_0 + (c - c_0) \min\left(1, \frac{\gamma^{pl}}{\gamma_0}\right), \quad (7.22)$$

where c_0 is the initial cohesion, $\gamma_0 = 0.1$ a critical value and $\gamma^{pl} = \int \dot{\epsilon}_{II_plastic} dt$ the integrated plastic strain rate invariant over the current time step.

7.2.3 Model set up

Initially the oceanic crust is set to a depth of 8km and the oceanic lithospheric upper mantle below is modeled until a total depth of 10km. The ridge axis is assumed to be located in the center at 0km with initially 10km ridge extending to each side (see Fig. 7.1-7.3). We assume a low-viscosity lower lithosphere ($10^{20} \text{ kg m}^{-1} \text{ s}^{-1}$), which is behaving more ductile than brittle (Fig. 6.6) and the oceanic crust with an initially higher viscosity above ($10^{25} \text{ kg m}^{-1} \text{ s}^{-1}$) with a brittle behavior (Fig.

6.6). The seaﬂoor at the top of the model domain is modeled as a free surface, allowing for the development of seaﬂoor bathymetry, also the moho is free to move in any direction. We are primarily interested to study the deformation of the oceanic crust above a less viscous mantle. The lower edge of the model domain, which is an artiﬁcial cut of the lower lithosphere is thus not allowed to move in a vertical direction ($u_y=0$). Assigned rock properties and other model parameters applied can be seen in table 7.1. Seaﬂoor spreading is modelled by pulling with a constant velocity of 2.5 cm per year to each side of the ridge (Fig. 7.1-7.3) an average spreading rate for the MAR. Varying supply of magma to the ridge is simulated by a diking region, simulated by a dilation term multiplied with a factor ξ (between 0 and 1 (see section 7.2.2)). A factor ξ of 1 represents purely magmatic conditions. With $\xi=0$ no magma is supplied to the ridge axis and the extension of the ridge is occurring only via brittle tectonic deformation.

Parameter	Value	Unit
<u>Model domain</u>		
Width	20	km
Depth to moho	8	km
Height	10	km
Width dike	100-1200	m
Time step dt	30×10^3	years
Spreading velocity	2.5	cm/year
<u>Rock properties (mantle/crust/dike)</u>		
Density	3300	kg m^{-3}
Shear modulus G	5×10^{10}	Pa
Viscosity (μ_{ve})	$10^{20}/10^{25}/10^{20}$	$\text{kg s}^{-1} \text{m}^{-1}$
Dilation angle (ψ)	0/0/10	°
Friction angle (ϕ)	20/30/0	°
Cohesion (c_0/c_{weak})	$4 \times 10^7/0.2 \times 10^7$	Pa

Table 7.1: Applied parameters for the 2D visco-elasto-plastic mechanical model used to simulate seaﬂoor spreading under varying tectono-magmatic conditions. Dimensions of the model domain are initial values before the beginning of the simulation runs. Also viscosity and cohesion given are initial values, which can be modified during plasticity iterations.

7.3 Simulation results

Simulation results from fully 2D visco-elasto-plastic dynamic modeling of the deforming oceanic lithosphere at an oceanic ridge under varying tectono-magmatic conditions are shown in figure 7.1-7.3. During purely magmatic conditions ($\psi^*\xi$; $\xi=1$) the amount of newly forming oceanic crust is balancing the rate at which the tectonic plates are separating (Fig. 7.1a-7.1d). All deformation is concentrated to the neovolcanic zone (Fig. 7.1c) and no brittle fracturing is occurring. The stress state of the entire crust is rather homogenous (Fig. 7.1b) and no elements are above the yield stress (Fig. 7.2d) such that the visco-elastic viscosity and initial cohesion of the model domain is not modified. The rheology is thus visco-elastic, without a contribution from plasticity. When the extension of the tectonic plates, due to a lower supply of magma to the ridge ($\xi<1$), is not fully accommodated by newly formed crust at the axis, the oceanic crust experiences thinning (Fig. 7.1e - 7.3). When the magmatic activity is decreasing but still dominating ($\xi>0.5$) the stress inside the crust is elevated ($\xi=0.8$, Fig. 7.1f) but deformation continues to be focused to the axial region of diking (Fig. 7.1g). The crust still experiences no brittle fracturing, such that the visco-elastic viscosity is not modified (Fig. 7.1h). When the amount of tectonic and magmatic activity during seafloor spreading are balanced ($\xi=0.5$, Fig.7.2) the stress field of the oceanic crust is more heterogeneous (Fig. 7.2b) and is above the yield stress, which leads to a possibility of brittle fracturing (Fig. 7.2d). Crustal viscosity and cohesion are modified (Fig. 7.2e and f), however no distinct zones of brittle deformation are appearing and deformation is still focused on the axial zone (Fig. 7.2c). When tectonic processes are dominating ($\xi<0.5$, Fig. 7.3) shear bands of brittle deformation are forming, which are dipping in an angle ($\sim 45^\circ$) towards the ridge axis. They are showing elevated strain rates (Fig. 7.3d and g), decreased viscosity (Fig. 7.3e and h) and cohesion (Fig. 7.3f and i). Hence, with decreasing magmatic activity, deformation is not only focused to the ridge axis but shifts to zones of shear deformation in off-axis regions. Note how no deformation is occurring in the axial zone during purely tectonic extension ($\xi=0$, Fig. 7.3g).

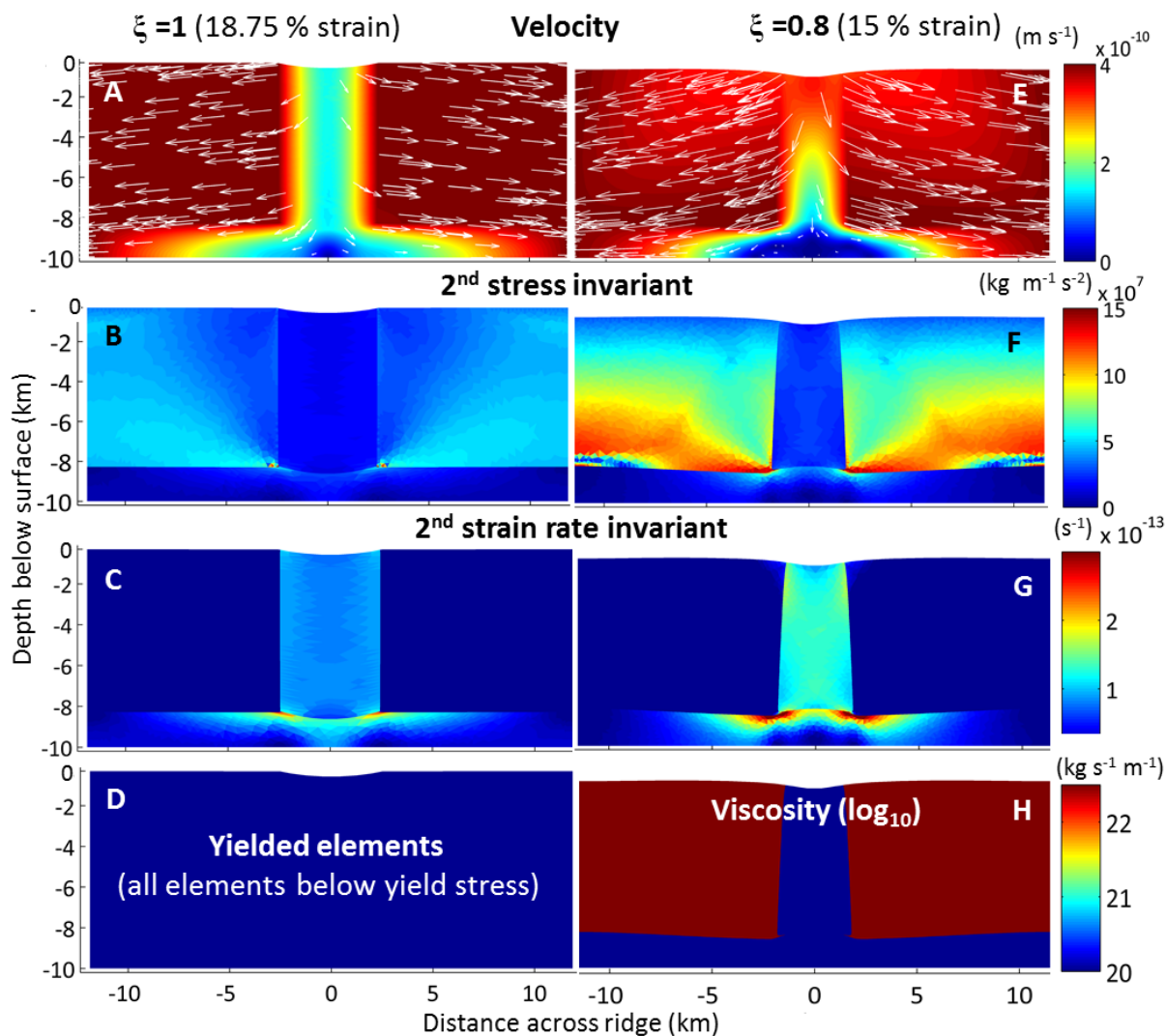


Figure 7.1: Crustal accretion during seafloor spreading at oceanic ridges with dominating magmatic activity ($\psi^*\xi$; $\xi=1$ and $\xi=0.8$ respectively). ψ is the dilation term, which simulates the supply of magma to a region of diking. The initial width of the diking region was set to 1.2km and 800m respectively, results are shown after 18.75% and 15% of total strain reached. Plate separation (A and E) is balanced by the rate of magma supply to the ridge axis. Hence strain rates (zones of deformation) are highest in the axial region and very low in off-axis region (C and G). The crustal stress field is relatively homogeneous during highly magmatic accretion (B) and stress increased and becomes more heterogeneous when magmatic activity is decreasing ($\xi=0.8$, F). In both scenarios the yield stress is not exceeded (D) and consequently viscosity is not modified (H).

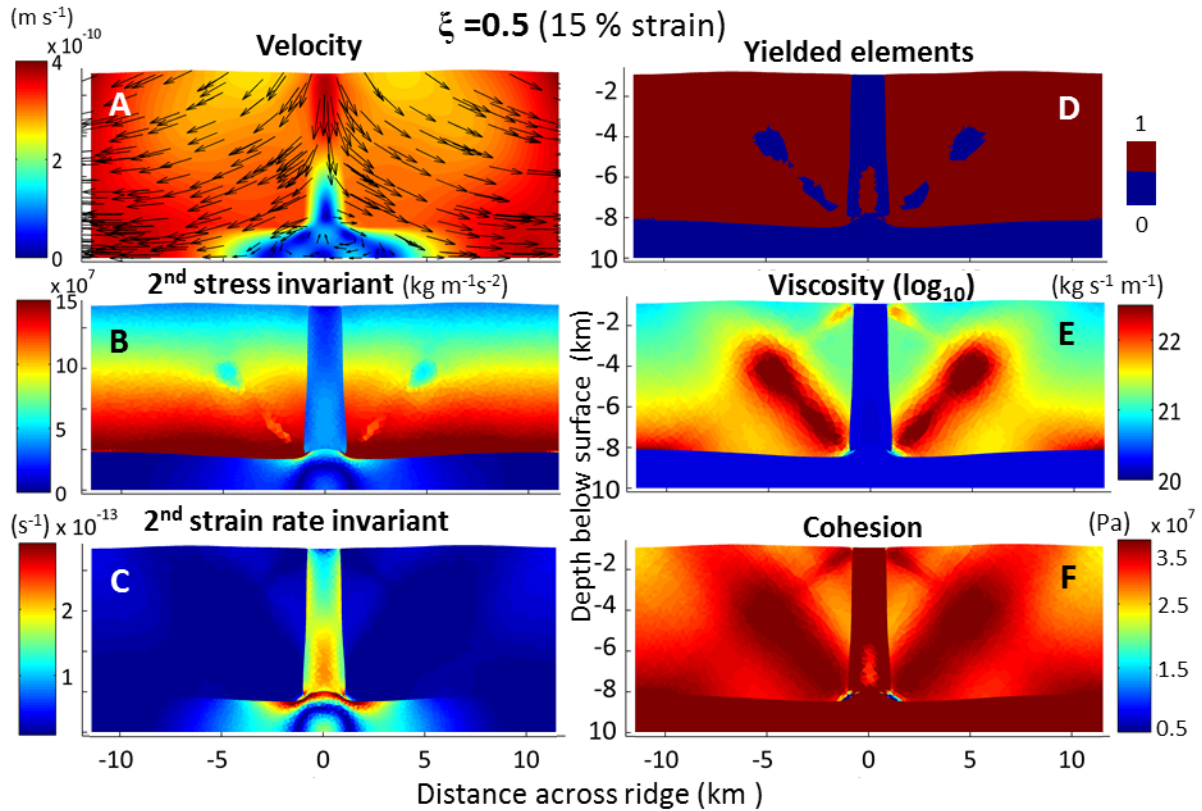


Figure 7.2: Crustal accretion during seafloor spreading (A) at oceanic ridges with balanced magmatic and tectonic activity ($\psi^*\xi$; $\xi=0.5$). ψ is the dilation term, which simulates the supply of magma to a region of diking. The initial width of the diking region was set to 250m, results are shown after 15% of total strain reached. The stress in the crust (B) is exceeding the yield strength of the rocks (D), such that brittle fracturing is potentially possible. Crustal viscosity (E) and cohesion (F) are modified accordingly. Nevertheless, strain rates (regions of deformation) remain highest in the axial region (C).

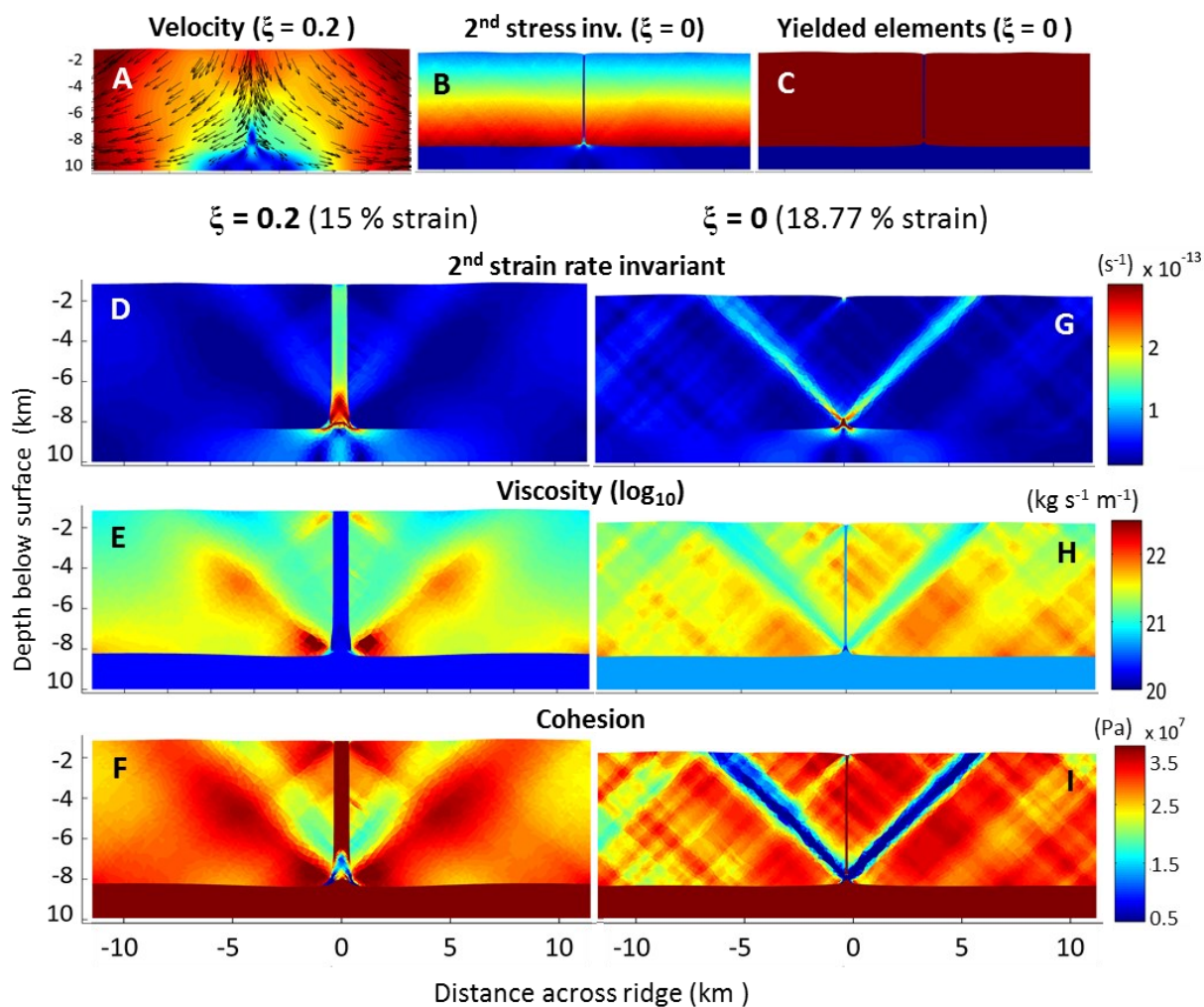


Figure 7.3: Seafloor spreading (A) at oceanic ridges with dominating tectonic extension ($\psi^*\xi$; $\xi=0.2$ and $\xi=0$ respectively). ψ is the dilation term, which simulates the supply of magma to a region of diking. The initial width of the diking region was in both scenarios set to 100m, results are shown after 15% and 18.77% of total strain reached. The stress in the crust (B) exceeds the yield strength of the rocks (C), such that those regions become brittle. Crustal viscosity (E and H) and cohesion (F and I) are decreased in comparison to their their initial values. Shear bands of brittle deformation, which are dipping towards the ridge axis are forming (D-I). Strain rates (regions of deformation) are highest in the off-axis regions during purely tectonic extension (G). Overall crustal thinning is increasing with increasing tectonic activity.

7.4 Discussion & Conclusions

The scenario of purely magmatic activity ($\xi=1$, Fig. 7.1a-d) might represent an (unnatural) endmember of an ultrafast-spreading Mid-ocean ridge segment or a magmatic ridge segments at slow-spreading ridges (section 1.1, Fig 1.1), where the amount of tectonic faulting is low due to the high supply magma to the ridge axis via dikes and extrusive pillow lava (see section 1.1). Deformation is focused to the axial region and no brittle fracturing occurs. The other (unnatural) extreme endmember of purely tectonic activity ($\xi=0$, Fig. 7.3b-c and g-i) might represent an ultraslow-spreading ridge segment or a slow-spreading ridge segment with dominating tectonic crustal accretion (section 1.1, Fig 1.1). There the shear bands might represent zones of brittle faulting in the oceanic crust, which terminate at the seafloor in a distance of up to several km to the ridge axis (e.g. Fig. 7.3d-i, see also LHF1, Chapter 4, Fig. 4.1).

If high strain rates are interpreted as regions of high deformation, such as tectonic fault zones, which have a higher permeability, the results from our mechanical model can be used as powerful tool to predict the permeability structure of the oceanic crust under varying tectono-magmatic conditions. It remains to be identified how exactly strain rates could be translated into values of permeability. The permeability field could be used as input for hydrothermal flow modeling (Chapter 4 and 5) and the combined results could help to better understand the interplay of tectonic deformation and hydrothermal circulation at mid-ocean ridges.

A crustal permeability with little heterogeneities and deformation focused to the axial zone would be the result of the high magma supply to fast-spreading ridges, like the EPR. Hydrothermal flow there is expected to be primarily controlled by the position of the driving heat source at depth. At fast spreading ridges hydrothermal convection is believed to be driven by a magma chamber below the ridge axis. There hydrothermal discharge in a close to homogenous permeable crust would thus occur vertically above the heat source in a narrow region close the ridge

axis. A faulted crust with a highly heterogeneous permeability structure and regions of off-axis deformation would be the result of the low magma supply during slow-spreading conditions, like at the Mid-Atlantic ridge. There the position of hydrothermal discharge would be controlled by high permeability pathways like faults and fractures in the seafloor (see Chapter 4). Tectonic faults in extensional settings have a normal faulting direction and are thus dipping towards the axis of mid-ocean ridges at depth. They are outcropping at the seafloor in a distance of up to several kilometers from the axis, which is consequently also a likely position of hydrothermal vent sites at slow-spreading ridges. The results from the mechanical modelling of seafloor spreading presented in this chapter can be combined with our results from hydrothermal flow simulations (Chapter 4 and 5). Together they point towards a general validity of the key hypothesis, which to prove was one aim of this thesis (section 1.2).

References Cited

- Behn, M. D., and Ito, G., 2008, Magmatic and tectonic extension at mid-ocean ridges: 1. Controls on fault characteristics: *Geochemistry Geophysics Geosystems*, v. 9.
- Buck, W. R., Lavier, L. L., and Poliakov, A. N. B., 2005, Modes of faulting at mid-ocean ridges: *Nature*, v. 434, no. 7034, p. 719-723.
- Buiter, S. J. H., Babeyko, A. Y., Ellis, S., Gerya, T. V., Kaus, B. J. P., Kellner, A., Schreurs, G., and Yamada, Y., 2006, The numerical sandbox: comparison of model results for a shortening and an extension experiment: *Geological Society, London, Special Publications*, v. 253, no. 1, p. 29-64.
- Cherkaoui, A. S. M., Wilcock, W. S. D., Dunn, R. A., and Toomey, D. R., 2003, A numerical model of hydrothermal cooling and crustal accretion at a fast spreading mid-ocean ridge: *Geochemistry Geophysics Geosystems*, v. 4, p. 19.
- Gerya, T., 2010, *Introduction to Numerical Geodynamic Modelling*, New York, Cambridge University Press.
- Gueydan, F., Précigout, J., and Montési, L. G. J., 2014, Strain weakening enables continental plate tectonics: *Tectonophysics*, v. 631, no. 0, p. 189-196.
- Ito, G., and Behn, M. D., 2008, Magmatic and tectonic extension at mid-ocean ridges: 2. Origin of axial morphology: *Geochemistry Geophysics Geosystems*, v. 9.
- Iyer, K., Rüpke, L. H., and Morgan, J. P., 2010, Feedbacks between mantle hydration and hydrothermal convection at ocean spreading centers: *Earth and Planetary Science Letters*, v. 296, no. 1-2, p. 34-44.
- Kaus, B. J. P., 2010, Factors that control the angle of shear bands in geodynamic numerical models of brittle deformation: *Tectonophysics*, v. 484, no. 1-4, p. 36-47.

-
- Olive, J.-A., Behn, M. D., and Tucholke, B. E., 2010, The structure of oceanic core complexes controlled by the depth distribution of magma emplacement: *Nature Geosci.*, v. 3, no. 7, p. 491-495.
- Phipps Morgan, J., and Chen, Y. J., 1993, The genesis of oceanic crust: magma injection, hydrothermal circulation, and crustal flow: *J. Geophys. Res.*, v. 98, p. 6283-6297.
- Quick, J. E., and Denlinger, R. P., 1993, Ductile deformation and the origin of layered gabbro in ophiolites: *J. Geophys. Res.*, v. 98, p. 14015-14027.
- Ranalli, G., 1995, *Rheology of the earth*, Chapman & Hall, 413 p.:
- Sleep, N. H., 1975, Formation of oceanic crust: Some thermal constraints: *Journal of Geophysical Research*, v. 80, no. 29, p. 4037-4042.
- Theissen-Krah, S., Iyer, K., Rupke, L. H., and Morgan, J. P., 2011, Coupled mechanical and hydrothermal modeling of crustal accretion at intermediate to fast spreading ridges: *Earth and Planetary Science Letters*, v. 311, no. 3-4, p. 275-286.
- Tucholke, B. E., Behn, M. D., Buck, W. R., and Lin, J., 2008, Role of melt supply in oceanic detachment faulting and formation of megamullions: *Geology*, v. 36, no. 6, p. 455-458.

8 Discussion & Implications

There is a large discrepancy between maximum measured vent temperatures of approximately 400°C (see also chapter 5) and magmatic temperatures of 1200°C driving hydrothermal convection, which was already pointed out by Lowell (1991). Jupp and Schultz (2000) provided a first explanation for hydrothermal plume temperatures derived from numerical modeling which points to strong feedbacks between transport processes and the thermodynamic properties of water. They analysed the properties of pure water, since the required parameters are not known for salt water over the studied range of temperature. However, first order behavior is expected to be comparable between pure water and hydrothermal fluids with a low salinity similar to seawater of around (~3.2 weight % NaCl). Jupp and Schultz (2000) introduced the concept of “fluxibility”, which implies a dominant temperature of rising hydrothermal plumes. Assuming that enough heat is provided to drive the hydrothermal convection cell, maximum fluxibility is reached at ~400°C, which is the temperature where buoyancy-driven energy transport is maximized due to the inherent fluid properties of water (Fig. 3.2). After the initial formation of a rising hydrothermal plume, the results from this work in chapter 4 and 5 show that hydrothermal fluid temperatures are significantly controlled by heterogeneities in crustal permeability. The critical role of crustal permeability for hydrothermal circulation has already been discussed by Lowell (1991). Permeability values for seafloor basalts attained through direct and indirect investigation methods (borehole logging, geophysics and numerical modeling) show a large uncertainty with a range from 10^{-9} to 10^{-22} m² (Fisher, 1998). Fisher and Becker (2000) reported bulk permeability values derived from a model for lateral fluid flow in oceanic crust between a highest value of 10^{-10} m² in youngest rocks close to the ridge axis and a lowest value of 10^{-14} m² in aged crust in off-axis regions. However, due to the presence of faults and fractures, especially at slow-spreading ridges (section 1.1 and

6.1) the permeability of the oceanic crust is highly heterogeneous and is thus likely to vary significantly from the values above on more local scales. The importance of fault zones for hydrothermal fluid flow (McCaig et al., 2007; McCaig and Harris, 2012) and their complex permeability structure has been pointed out (Caine et al., 1996). Also Ingebritsen et al. (2010) state how the perception of permeability e.g. in the context of simulations for hydrothermal fluid flow has become much more complex. Several numerical modeling studies have addressed the interplay of permeability and hydrothermal fluid flow in recent years (Driesner, 2010; Theissen-Krah et al., 2011; Weis and Driesner, 2013; Weis, 2015). The results from this work have contributed a new aspect on the discussion of crustal permeabilities during hydrothermal circulation, highlighting the control of heterogeneous permeability fields with e.g. fault zones on fluid flow patterns and vent temperatures at the seafloor (Chapter 4 and 5). We have shown that not only absolute values of permeability have to be considered (Driesner, 2010) but that permeability contrasts are equally important. Permeability contrasts are particularly important at slow-spreading ridges, which show a faulted, highly heterogeneous crustal permeability.

It has previously been pointed out that the velocity of seafloor-spreading has a major influence on the style of hydrothermal activity at oceanic ridges (section 2.2). Submarine hydrothermal activity is intimately related to the formation of hydrothermal mineral deposits. Submarine Massive Sulphide (SMS) deposits are a potential future ore resource (Rona, 2008; Hannington et al., 2011). Hydrothermal fluid temperature and flow pattern, which both have been studied in detail in this work, are significantly controlling size and character of SMS deposits. Fluid temperature is a key factor that controls the possible amount and type of dissolved minerals carried in hydrothermal fluids. Only if hydrothermal fluids have a temperature higher than 300°C they can efficiently transport metals from the crust to the seafloor (Hannington et al., 2011). The contact of hot hydrothermal fluids with cold seawater causes dissolved metals to precipitate sulfide minerals around the vent chimneys. It has been suggested that mineral deposits at slow-spreading ridges

are of greater volume than at fast-spreading ones (Hannington et al., 2005). In slow-spreading settings, deposits are exposed to fault-controlled hydrothermal convection under a longer period than at faster ones (Fornari and Embley, 1995; Jamieson et al., 2014). This can result in mineralizations with a larger volume at slow-spreading ridges.

Due to the heterogeneous permeability at slow-spreading ridges like the MAR, the results of this work (Chapter 4 and 5) imply that in such settings, a large part of the hydrothermal circulation in the oceanic lithosphere is occurring at lower than black smoker temperatures of 400°C. Other MAR fault-controlled systems than the LHF1 (300-350°C) system, which has been investigated here, are the Rainbow hydrothermal field (365°C), TAG (up to 369°C) and Nibelungen (372°C), which show similar vent temperatures (Edmonds et al., 1996; Douville et al., 2002; Schmidt et al., 2011). In all systems fluids are ascending along fault zones and may face the same fluid dynamical processes as at LHF1. Further supporting our findings is the fact that, if the young ocean floor was predominantly cooled by high-temperature fluid flow up to the seafloor, the amount of copper deposited at the seafloor in the neovolcanic zone should be much larger than observed (Cathles, 2011; Hannington, 2013). The most probable explanation for this discrepancy is thus, that a large fraction of the hydrothermal fluids vent at temperatures below 300°C — too low for the reduced fluids to carry copper. Such vent fields, which possible are fault controlled and thus would be located in a distance to the ridge axis, might be more difficult to detect than high-temperature, on axis systems.

German and Lin (2004) had pointed out that there is a contradiction to a previous hypothesis by Baker et al. (1996) about the relation of available magmatic heat flux and thus spreading rate and the abundance of hydrothermal venting on oceanic ridge crests. Baker et al. (1996) predicted that the amount of venting should directly scale with spreading rate, with consequently the largest amount of hydrothermal venting along fast-spreading ridges. What appears to contradict or at least modify this hypothesis is, as German and Lin (2004) stated, the discovery of

hydrothermal activity along some ultraslow-spreading ridges like the SW Indian Ridge (German et al., 1998; Bach et al., 2002) and the Gakkel Ridge in the Arctic Ocean (Edmonds et al., 2003). The results of this work imply that, while the total energy discharged at hydrothermal vent sites might be lower than at fast-spreading ridges, the number of vent sites at slow-spreading ridges does not necessarily need to be lower, as hydrothermal venting might occur at lower temperatures and thus a lower energy output.

First order processes in hydrothermal systems can excellently be studied with pure water, single-phase convection as shown by e.g. (Driesner, 2010). For more complex processes however, it has become increasingly clear that there is a need for multi-phase codes, which can distinguish between a liquid and a vapor phase (e.g. Geiger et al., 2006; Driesner and Geiger, 2007a; Driesner and Heinrich, 2007; Coumou et al., 2009b; Lewis and Lowell, 2009). Moreover the transport of saline fluids is important if ore forming processes during e.g. SMS formation shall be investigated. Supercritical and subcritical phase transitions control physical and chemical properties of hydrothermal fluids (e.g. solubility, metal concentration) (Bischoff and Rosenbauer, 1988).

References Cited

- Bach, W., Banerjee, N. R., Dick, H. J. B., and Baker, E. T., 2002, Discovery of ancient and active hydrothermal systems along the ultra-slow spreading Southwest Indian Ridge 10°–16°E: *Geochemistry, Geophysics, Geosystems*, v. 3, no. 7, p. 1-14.
- Baker, E. T., Chen, Y. J., and Morgan, J. P., 1996, The relationship between near-axis hydrothermal cooling and the spreading rate of mid-ocean ridges: *Earth and Planetary Science Letters*, v. 142, no. 1-2, p. 137-145.
- Bischoff, J. L., and Rosenbauer, R. J., 1988, Liquid-vapor relations in the critical region of the system NaCl-H₂O from 380 to 415°C: A refined determination of the critical point and two-phase boundary of seawater: *Geochimica et Cosmochimica Acta*, v. 52, no. 8, p. 2121-2126.
- Caine, J. S., Evans, J. P., and Forster, C. B., 1996, Fault zone architecture and permeability structure: *Geology*, v. 24, no. 11, p. 1025-1028.
- Cathles, L., 2011, What processes at mid-ocean ridges tell us about volcanogenic massive sulfide deposits: *Mineralium Deposita*, v. 46, no. 5, p. 639-657.

- Coumou, D., Driesner, T., Weis, P., and Heinrich, C. A., 2009b, Phase separation, brine formation, and salinity variation at Black Smoker hydrothermal systems: *Journal of Geophysical Research-Solid Earth*, v. 114, p. 16.
- Douville, E., Charlou, J. L., Oelkers, E. H., Bienuvenu, P., Jove Colon, C. F., Donval, J. P., Fouquet, Y., Prieur, D., and Appriou, P., 2002, The rainbow vent fluids (36°14'N, MAR): the influence of ultramafic rocks and phase separation on trace metal content in Mid-Atlantic Ridge hydrothermal fluids: *Chemical Geology*, v. 184, no. 1-2, p. 37-48.
- Driesner, T., 2010, The interplay of permeability and fluid properties as a first order control of heat transport, venting temperatures and venting salinities at mid-ocean ridge hydrothermal systems: *Geofluids*, v. 10, no. 1-2, p. 132-141.
- Driesner, T., and Geiger, S., 2007a, Numerical Simulation of Multiphase Fluid Flow in Hydrothermal Systems: *Reviews in Mineralogy and Geochemistry*, v. 65, no. 1, p. 187-212.
- Driesner, T., and Heinrich, C. A., 2007, The system H₂O-NaCl. Part I: Correlation formulae for phase relations in temperature-pressure-composition space from 0 to 1000 degrees C, 0 to 5000 bar, and 0 to 1 X-NaCl: *Geochimica et Cosmochimica Acta*, v. 71, no. 20, p. 4880-4901.
- Edmonds, H. N., German, C. R., Green, D. R. H., Huh, Y., Gamo, T., and Edmond, J. M., 1996, Continuation of the hydrothermal fluid chemistry time series at TAG, and the effects of ODP drilling: *Geophysical Research Letters*, v. 23, no. 23, p. 3487-3489.
- Edmonds, H. N., Michael, P. J., Baker, E. T., Connelly, D. P., Snow, J. E., Langmuir, C. H., Dick, H. J. B., Muhe, R., German, C. R., and Graham, D. W., 2003, Discovery of abundant hydrothermal venting on the ultraslow-spreading Gakkel ridge in the Arctic Ocean: *Nature*, v. 421, no. 6920, p. 252-256.
- Fisher, A. T., 1998, Permeability within basaltic oceanic crust: *Reviews of Geophysics*, v. 36, no. 2, p. 143-182.
- Fisher, A. T., and Becker, K., 2000, Channelized fluid flow in oceanic crust reconciles heat-flow and permeability data: *Nature*, v. 403, no. 6765, p. 71-74.
- Fornari, D. J., and Embley, R. W., 1995, Tectonic and Volcanic Controls on Hydrothermal Processes at the Mid-Ocean Ridge: an overview based on near-bottom and submersible studies, *in* Humphris, S. E., Zierenberg, R. A., Mullineaux, L. S., and Thomson, R. E., eds., *Seafloor Hydrothermal Systems - Physical, chemical, biological and geological interactions*, Volume 91: Washington DC, American Geophysical Union, p. 1-466.
- Geiger, S., Driesner, T., Heinrich, C., and Matthäi, S., 2006, Multiphase Thermohaline Convection in the Earth's Crust: I. A New Finite Element – Finite Volume Solution Technique Combined With a New Equation of State for NaCl-H₂O: *Transport in Porous Media*, v. 63, no. 3, p. 399-434.
- German, C. R., Baker, E. T., Mevel, C., Tamaki, K., and the F. S. T., 1998, Hydrothermal activity along the southwest Indian ridge: *Nature*, v. 395, no. 6701, p. 490-493.
- German, C. R., and Lin, J., 2004, The Thermal Structure of the Oceanic Crust, Ridge-Spreading and Hydrothermal Circulation: How Well Do We Understand Their Inter-Connections?, *Mid-Ocean Ridges: Hydrothermal Interactions Between the Lithosphere and Oceans*, Volume Geophysical Monograph 148, AGU.
- Hannington, M., Jamieson, J., Monecke, T., Petersen, S., and Beaulieu, S., 2011, The abundance of seafloor massive sulfide deposits: *Geology*, v. 39, no. 12, p. 1155-1158.

- Hannington, M. D., 2013, The role of black smokers in the Cu mass balance of the oceanic crust: *Earth and Planetary Science Letters*, v. 374, p. 215-226.
- Hannington, M. D., De Ronde, C. E. J., and Petersen, S., 2005, Sea-Floor Tectonics and Submarine Hydrothermal Systems, *in* Hedenquist, J. W., Thompson, J. F. H., Goldfarb, R. J., and Richards, J. P., eds., *Economic Geology: One Hundredth Anniversary Volume, Volume 1*: Littleton, Colorado, Economic Geology, p. 111-141.
- Ingebritsen, S. E., Geiger, S., Hurwitz, S., and Driesner, T., 2010, Numerical simulation of magmatic hydrothermal systems: *Reviews of Geophysics*, v. 47.
- Jamieson, J. W., Clague, D. A., and Hannington, M. D., 2014, Hydrothermal sulfide accumulation along the Endeavour Segment, Juan de Fuca Ridge: *Earth and Planetary Science Letters*, v. 395, p. 136-148.
- Jupp, T., and Schultz, A., 2000, A thermodynamic explanation for black smoker temperatures: *Nature*, v. 403, no. 6772, p. 880-883.
- Lewis, K. C., and Lowell, R. P., 2009, Numerical modeling of two-phase flow in the NaCl-H₂O system: 2. Examples: *Journal of Geophysical Research-Solid Earth*, v. 114, p. 16.
- Lowell, R. P., 1991, Modeling continental and submarine hydrothermal systems: *Reviews of Geophysics*, v. 29, no. 3, p. 457-476.
- McCaig, A. M., Cliff, R. A., Escartin, J., Fallick, A. E., and MacLeod, C. J., 2007, Oceanic detachment faults focus very large volumes of black smoker fluids: *Geology*, v. 35, no. 10, p. 935-938.
- McCaig, A. M., and Harris, M., 2012, Hydrothermal circulation and the dike-gabbro transition in the detachment mode of slow seafloor spreading: *Geology*, v. 40, no. 4, p. 367-370.
- Rona, P. A., 2008, The changing vision of marine minerals: *Ore Geology Reviews*, v. 33, no. 3-4, p. 618-666.
- Schmidt, K., Garbe-Schönberg, D., Koschinsky, A., Strauss, H., Jost, C. L., Klevenz, V., and Königer, P., 2011, Fluid elemental and stable isotope composition of the Nibelungen hydrothermal field (8°18'S, Mid-Atlantic Ridge): Constraints on fluid-rock interaction in heterogeneous lithosphere: *Chemical Geology*, v. 280, no. 1-2, p. 1-18.
- Theissen-Krah, S., Iyer, K., Rupke, L. H., and Morgan, J. P., 2011, Coupled mechanical and hydrothermal modeling of crustal accretion at intermediate to fast spreading ridges: *Earth and Planetary Science Letters*, v. 311, no. 3-4, p. 275-286.
- Weis, P., 2015, The dynamic interplay between saline fluid flow and rock permeability in magmatic-hydrothermal systems: *Geofluids*, v. 15, no. 1-2, p. 350-371.
- Weis, P., and Driesner, T., 2013, The Interplay of Non-static Permeability and Fluid Flow as a Possible Pre-requisite for Supercritical Geothermal Resources: *Energy Procedia*, v. 40, no. 0, p. 102-106.

9 Conclusions & Outlook

The combined results of this work mark a key step forward in understanding the interplay of magma supply, tectonic faulting and hydrothermal processes at oceanic ridges under varying tectono-magmatic conditions. While the dominant temperature in a hydrothermal fluid at the initial formation of a rising hydrothermal plume is controlled by the inherent thermodynamic properties of water (maximum fluxibility, Jupp & Schulz, 2000), the results presented in this work (Chapter 4 and 5) confirm how permeability of the lithosphere controls fluid temperatures during the ascent of hydrothermal fluids until venting at the seafloor (Driesner, 2010). Additionally, the findings of this work highlight the importance of permeability contrasts in the oceanic lithosphere in controlling submarine hydrothermal vent temperatures. The results are especially significant for hydrothermal systems at slow-spreading ridges, which frequently are controlled by permeable fault zones. High-temperature hydrothermal fluids can only efficiently flow along permeable fault zones that are not too permeable or wide, otherwise a distinct temperature drop as the result of mixing with entraining cold seawater occurs. Since slow-spreading ridges typically have a complex, heterogeneous permeability structure, which includes numerous faults and fractures, the results of this work imply that the amount of low-temperature hydrothermal circulation is expected to be considerably higher than at fast-spreading ridges. This implication is potentially important for the global distribution of SMS deposits at oceanic ridges, which most effectively form if hydrothermal fluid temperatures are higher than 300° C. The results from dynamic modeling of seafloor spreading under varying tectono-magmatic conditions (Chapter 7) show how crustal thinning and brittle faulting is increasing with decreasing supply of magma to the ridge axis.

It had recently been shown that ridge segments of the slow-spreading Mid-Atlantic Ridge experience shifting episodes of tectonic and magmatic phases

(Escartin et al., 2008, section 1.1). The initial hypothesis of this work (see section 1.1 and 1.2), about the control of the tectono-magmatic state of slow-spreading ridge segment on the position of hydrothermal vent sites, was amongst others based on these findings. The Logatchev 1 hydrothermal field, which is an off-axis MAR vent field that shows stable vent temperatures of 300-350°C and which is associated with an active tectonic fault zone outcropping in a distance of 8 km from the ridge axis, has been studied as part of this work. Some MAR segments appear to have a higher supply of magma and are showing characteristics more similar to fast-spreading ridges. The MAR vent field 5°S is such a high-temperature (~400°C) hydrothermal field located in the vicinity of the ridge axis (section 1.1).

The combined results from hydrothermal flow modelling and lithosphere-scale mechanical model of oceanic ridges indicate how vent site location is controlled by different styles of seafloor spreading (Chapter 7), which confirms the above hypothesis. The results of the Logatchev study (Chapter 4) clearly show how hydrothermal flow is deviated and controlled by permeable fault zones and chapter 5 shows that hydrothermal discharge without an inclined fault zone is constantly occurring at the seafloor vertically above a driving heat source. At slow-spreading ridge segments tectonic faults are typically dipping towards the ridge axis at depth and are outcropping at the seafloor in a distance of up to several kilometers from the axis (e.g. Chapter 4). The off-axis fault termination is thus a likely position for fault controlled hydrothermal venting, typically occurring at slow-spreading ridge segments in a tectonic phase (Chapter 4 and 7). Hydrothermal circulation at fast-spreading ridges, which typically show a high magma supply and a more homogenous permeability (Chapter 7), appears to be primarily controlled by the position of the driving heat source at depth below the ridge axis. This scenario that favors hydrothermal venting in the axial region vertically above the heat source, also applies to magmatic segments at slow-spreading ridges.

Outlook

It would be interesting to fully couple the porous flow model of hydrothermal circulation with the mechanical model for visco-elasto-plastic deformation of the lithosphere during seafloor spreading. Such a mechanical model has been developed for fast-spreading ridges, which accounts for visco-elastic deformation (Theissen-Krah et al., 2011). Such simulations remain however challenging since hydrothermal circulation and seafloor spreading occur on very different time-scales of thousands and millions of years respectively. The additional stress iterations, which have to be conducted during plastic failure of brittle rocks at slow-spreading ridges requires even more computation time. Further hydrothermal flow simulations could be conducted, which use the actual permeability field, resulting from the mechanical model runs. For this strain rates have to be translated into values of permeability in an adequate way.

Moreover it would be interesting to study additional field data of submarine hydrothermal systems that are associated with permeable fault zones with respect to their vent temperatures, their distance from the ridge axis and properties of the tectonic fault zone. Valuable data on permeability and temperatures might also exist from land-based geothermal systems. Furthermore the hydrothermal flow model in this work could be modified to solve for chemical reactions and thus include the formation of anhydrite or quartz during hydrothermal convection. This might be an important process to reduce permeability or width of fault zones, a crucial parameter in controlling hydrothermal vent temperatures as shown in this work. Some chemical reactions during hydrothermal circulation require that the model can solve for the convection of saltwater (NaCl-system) and also that the code is able to distinguish between a liquid and vapor phases (2-phase flow). Moreover crustal permeability could be coupled to temperature, which is assumed to decrease during heating. At temperatures higher than $\sim 600^{\circ}\text{C}$ no earthquakes are recorded in rocks, which are then assumed to behave ductile without brittle fracturing. In the absence of open voids like fractures or pores permeability is presumably very low.

Also viscosity could be coupled to temperature. Viscosity is crucial for the mechanical visco-elasto-plastic modelling of seafloor spreading and decreases in materials that get heated.

Complete reference list

- Allen, D. E., and Seyfried Jr, W. E., 2004, Serpentinization and heat generation: constraints from Lost City and Rainbow hydrothermal systems: *Geochimica et Cosmochimica Acta*, v. 68, no. 6, p. 1347-1354.
- Alt, J. C., 1995, Subseafloor Processes in Mid-Ocean Ridge Hydrothermal Systems, *in* Humphris, S. E., Zierenberg, R. A., Mullineaux, L. S., and Thomson, R. E., eds., *Seafloor Hydrothermal systems - physical, chemical, biological and geological interactions*, Volume 91: Washington DC, American Geophysical Union, p. 1-466.
- Andersen, C., Rüpke, L., Hasenclever, J., Grevemeyer, I., and Petersen, S., 2015, Fault geometry and permeability contrast control vent temperatures at the Logatchev 1 hydrothermal field, *Mid-Atlantic Ridge: Geology*, v. 43, no. 1, p. 51-54.
- Bach, W., Banerjee, N. R., Dick, H. J. B., and Baker, E. T., 2002, Discovery of ancient and active spreading systems along the ultra-slow spreading Southwest Indian Ridge 10°–16°E: *Geochemistry, Geophysics, Geosystems*, v. 3, no. 7, p. 1-14.
- Baker, E. T., Chen, Y. J., and Morgan, J. P., 1996, The relationship between near-axis hydrothermal cooling and the spreading rate of mid-ocean ridges: *Earth and Planetary Science Letters*, v. 142, no. 1-2, p. 137-145.
- Baker, E. T., and German, C. R., 2004, On the global distribution of hydrothermal vent fields, *in* German, C. R., Lin, J., and Parson, M., eds., *Mid-Ocean Ridges: Hydrothermal Interactions Between the Lithosphere and Oceans*, Volume Geophysical Monograph Series: Washington, DC, American Geophysical Union, p. 245 - 266.
- Baker, E. T., Massoth, G. J., Walker, S. L., and Embley, R. W., 1993, A method for quantitatively estimating diffuse and discrete hydrothermal discharge: *Earth and Planetary Science Letters*, v. 118, no. 1-4, p. 235-249.
- Bani-Hassan, N., Iyer, K., Rüpke, L. H., and Borgia, A., 2012, Controls of bathymetric relief on hydrothermal fluid flow at mid-ocean ridges: *Geochemistry Geophysics Geosystems*, v. 13.
- Bauer, O., 1998, *Prost 4.1 PROperties of water and STeam*: TU Hamburg Harburg.
- Bear, J., 1988, *Dynamics of Fluids in Porous Media*, Courier Corporation, 764 p.:
- Beaulieu, S. E., Baker, E. T., German, C. R., and Maffei, A., 2013, An authoritative global database for active submarine hydrothermal vent fields: *Geochemistry, Geophysics, Geosystems*, v. 14, no. 11, p. 4892-4905.
- Becker, K., and Fisher, A. T., 2000, Permeability of upper oceanic basement on the eastern flank of the Juan de Fuca Ridge determined with drill-string packer experiments: *J. Geophys. Res.*, v. 105, no. B1, p. 897-912.
- Behn, M. D., and Ito, G., 2008, Magmatic and tectonic extension at mid-ocean ridges: 1. Controls on fault characteristics: *Geochemistry Geophysics Geosystems*, v. 9.
- Bird, R. B., Stewart, W. E., and Lightfoot, E. N., 2007, *Transport Phenomena*, John Wiley & Sons.

- Bischoff, J. L., and Rosenbauer, R. J., 1984, The critical point and two-phase boundary of seawater, 200-500°C: *Earth and Planetary Science Letters*, v. 68, no. 1, p. 172-180.
- , 1988, Liquid-vapor relations in the critical region of the system NaCl-H₂O from 380 to 415°C: A refined determination of the critical point and two-phase boundary of seawater: *Geochimica et Cosmochimica Acta*, v. 52, no. 8, p. 2121-2126.
- Buck, W. R., Lavier, L. L., and Poliakov, A. N. B., 2005, Modes of faulting at mid-ocean ridges: *Nature*, v. 434, no. 7034, p. 719-723.
- Buck, W. R., and Poliakov, A. N. B., 1998, Abyssal hills formed by stretching oceanic lithosphere: *Nature*, v. 392, no. 6673, p. 272-275.
- Buiter, S. J. H., Babeyko, A. Y., Ellis, S., Gerya, T. V., Kaus, B. J. P., Kellner, A., Schreurs, G., and Yamada, Y., 2006, The numerical sandbox: comparison of model results for a shortening and an extension experiment: *Geological Society, London, Special Publications*, v. 253, no. 1, p. 29-64.
- Caine, J. S., Evans, J. P., and Forster, C. B., 1996, Fault zone architecture and permeability structure: *Geology*, v. 24, no. 11, p. 1025-1028.
- Canales, J. P., Sohn, R. A., and Demartin, B. J., 2007, Crustal structure of the Trans-Atlantic Geotraverse (TAG) segment (Mid-Atlantic Ridge, 26 degrees 10-Minutes-N): Implications for the nature of hydrothermal circulation and detachment faulting at slow spreading ridges: *Geochemistry Geophysics Geosystems*, v. 8, p. 18.
- Cathles, L., 2011, What processes at mid-ocean ridges tell us about volcanogenic massive sulfide deposits: *Mineralium Deposita*, v. 46, no. 5, p. 639-657.
- Charlou, J. L., Donval, J. P., Douville, E., Jean-Baptiste, P., Radford-Knoery, J., Fouquet, Y., Dapoigny, A., and Stievenard, M., 2000, Compared geochemical signatures and the evolution of Menez Gwen (37°50'N) and Lucky Strike (37°17'N) hydrothermal fluids, south of the Azores Triple Junction on the Mid-Atlantic Ridge: *Chemical Geology*, v. 171, no. 1-2, p. 49-75.
- Cherkaoui, A. S. M., Wilcock, W. S. D., Dunn, R. A., and Toomey, D. R., 2003, A numerical model of hydrothermal cooling and crustal accretion at a fast spreading mid-ocean ridge: *Geochemistry Geophysics Geosystems*, v. 4, p. 19.
- Connelly, D. P., Copley, J. T., Murton, B. J., Stansfield, K., Tyler, P. A., German, C. R., Van Dover, C. L., Amon, D., Furlong, M., Grindlay, N., Hayman, N., Huhnerbach, V., Judge, M., Le Bas, T., McPhail, S., Meier, A., Nakamura, K.-i., Nye, V., Pebody, M., Pedersen, R. B., Plouviez, S., Sands, C., Searle, R. C., Stevenson, P., Taws, S., and Wilcox, S., 2012, Hydrothermal vent fields and chemosynthetic biota on the world's deepest seafloor spreading centre: *Nat Commun*, v. 3, p. 620.
- Corliss, J. B., Dymond, J., Gordon, L. I., Edmond, J. M., Herzen, R. P. V., Ballard, R. D., Green, K., Williams, D., Bainbridge, A., Crane, K., and Vanandel, T. H., 1979, Submarine thermal springs on the Galapagos Rift: *Science*, v. 203, no. 4385, p. 1073-1083.
- Coumou, D., Driesner, T., Geiger, S., Heinrich, C. A., and Matthai, S., 2006, The dynamics of mid-ocean ridge hydrothermal systems: Splitting plumes and fluctuating vent temperatures: *Earth and Planetary Science Letters*, v. 245, no. 1-2, p. 218-231.
- Coumou, D., Driesner, T., Geiger, S., Paluszny, A., and Heinrich, C. A., 2009a, High-resolution three-dimensional simulations of mid-ocean ridge hydrothermal systems: *Journal of Geophysical Research-Solid Earth*, v. 114.
- Coumou, D., Driesner, T., and Heinrich, C. A., 2008, The structure and dynamics of mid-ocean ridge hydrothermal systems: *Science*, v. 321, no. 5897, p. 1825-1828.

- Coumou, D., Driesner, T., Weis, P., and Heinrich, C. A., 2009b, Phase separation, brine formation, and salinity variation at Black Smoker hydrothermal systems: *Journal of Geophysical Research-Solid Earth*, v. 114, p. 16.
- Cowan, J., and Cann, J., 1988, Supercritical two-phase separation of hydrothermal fluids in the Troodos ophiolite: *Nature*, v. 333, no. 6170, p. 259-261.
- Dabrowski, M., Krotkiewski, M., and Schmid, D. W., 2008, MILAMIN: MATLAB-based finite element method solver for large problems: *Geochemistry Geophysics Geosystems*, v. 9.
- Davis, R. O., and Selvadurai, A. P. S., 2005, *Plasticity and Geomechanics*, Cambridge University Press, 287 p.
- Davis, T. A., and Hager, W. W., 2009, Dynamic Supernodes in Sparse Cholesky Update/Downdate and Triangular Solves: *Acm Transactions on Mathematical Software*, v. 35, no. 4.
- Deacon, G. E. R., 1960, The Indian Ocean Expedition: *Nature*, v. 187, p. 561-562.
- , 1964, International Indian Ocean Expedition: *Nature*, v. 201, p. 561-562.
- deMartin, B. J., Canales, R. A. R., Canales, J. P., and Humphris, S. E., 2007, Kinematics and geometry of active detachment faulting beneath the Trans-Atlantic Geotraverse (TAG) hydrothermal field on the Mid-Atlantic Ridge: *Geology*, v. 35, no. 8, p. 711-714.
- Detrick, R. S., Mutter, J. C., Buhl, P., and Kim, I. I., 1990, No evidence from multichannel reflection data for a crustal magma chamber in the MARK area on the Mid-Atlantic Ridge: *Nature*, v. 347, no. 6288, p. 61-64.
- Donaldson, I. G., 1962, Temperature gradients in the upper layers of the Earth's crust due to convective water flows: *Journal of Geophysical Research*, v. 67, no. 9, p. 3449-3459.
- Douville, E., Charlou, J. L., Oelkers, E. H., Bienvenu, P., Jove Colon, C. F., Donval, J. P., Fouquet, Y., Prieur, D., and Appriou, P., 2002, The rainbow vent fluids (36°14'N, MAR): the influence of ultramafic rocks and phase separation on trace metal content in Mid-Atlantic Ridge hydrothermal fluids: *Chemical Geology*, v. 184, no. 1-2, p. 37-48.
- Driesner, T., 2007, The system H₂O-NaCl. Part II: Correlations for molar volume, enthalpy, and isobaric heat capacity from 0 to 1000 degrees C, 1 to 5000 bar, and 0 to 1 X-NaCl: *Geochimica et Cosmochimica Acta*, v. 71, no. 20, p. 4902-4919.
- , 2010, The interplay of permeability and fluid properties as a first order control of heat transport, venting temperatures and venting salinities at mid-ocean ridge hydrothermal systems: *Geofluids*, v. 10, no. 1-2, p. 132-141.
- Driesner, T., and Geiger, S., 2007a, Numerical Simulation of Multiphase Fluid Flow in Hydrothermal Systems: *Reviews in Mineralogy and Geochemistry*, v. 65, no. 1, p. 187-212.
- Driesner, T., and Geiger, S., 2007b, Numerical simulation of multiphase fluid flow in hydrothermal systems, *in* Liebscher, A., and Heinrich, C. A., eds., *Fluid-Fluid Interactions*, Volume 65, p. 187-212.
- Driesner, T., and Heinrich, C. A., 2007, The system H₂O-NaCl. Part I: Correlation formulae for phase relations in temperature-pressure-composition space from 0 to 1000 degrees C, 0 to 5000 bar, and 0 to 1 X-NaCl: *Geochimica et Cosmochimica Acta*, v. 71, no. 20, p. 4880-4901.
- Dusunur, D., Escartin, J., Combier, V., Seher, T., Crawford, W., Cannat, M., Singh, S. C., Matias, L. M., and Miranda, J. M., 2009, Seismological constraints on the thermal structure along the Lucky Strike segment (Mid-Atlantic Ridge) and interaction of tectonic and magmatic processes around the magma chamber: *Marine Geophysical Researches*, v. 30, no. 2, p. 105-120.

- Edmonds, H. N., German, C. R., Green, D. R. H., Huh, Y., Gamo, T., and Edmond, J. M., 1996, Continuation of the hydrothermal fluid chemistry time series at TAG, and the effects of ODP drilling: *Geophysical Research Letters*, v. 23, no. 23, p. 3487-3489.
- Edmonds, H. N., Michael, P. J., Baker, E. T., Connelly, D. P., Snow, J. E., Langmuir, C. H., Dick, H. J. B., Muhe, R., German, C. R., and Graham, D. W., 2003, Discovery of abundant hydrothermal venting on the ultraslow-spreading Gakkel ridge in the Arctic Ocean: *Nature*, v. 421, no. 6920, p. 252-256.
- Escartin, J., Smith, D. K., Cann, J., Schouten, H., Langmuir, C. H., and Escrig, S., 2008, Central role of detachment faults in accretion of slow-spreading oceanic lithosphere: *Nature*, v. 455, no. 7214, p. 790-U795.
- Faust, C. R., and Mercer, J. W., 1979a, Geothermal reservoir simulation 1: Mathematical models for liquid-dominated and vapor-dominated hydrothermal systems: *Water Resources Research*, v. 15, no. 1, p. 23-30.
- , 1979b, Geothermal reservoir simulation 2: Numerical solution techniques for liquid-dominated and vapor-dominated hydrothermal systems: *Water Resources Research*, v. 15, no. 1, p. 31-46.
- , 1979c, A review of numerical simulation of hydrothermal systems: *Hydrological Sciences-Bulletin-des Sciences Hydrologiques*, v. 24, no. 3, p. 335-343.
- Fisher, A. T., 1998, Permeability within basaltic oceanic crust: *Reviews of Geophysics*, v. 36, no. 2, p. 143-182.
- Fisher, A. T., and Becker, K., 2000, Channelized fluid flow in oceanic crust reconciles heat-flow and permeability data: *Nature*, v. 403, no. 6765, p. 71-74.
- Fornari, D. J., and Embley, R. W., 1995, Tectonic and Volcanic Controls on Hydrothermal Processes at the Mid-Ocean Ridge: an overview based on near-bottom and submersible studies, *in* Humphris, S. E., Zierenberg, R. A., Mullineaux, L. S., and Thomson, R. E., eds., *Seafloor Hydrothermal Systems - Physical, chemical, biological and geological interactions*, Volume 91: Washington DC, American Geophysical Union, p. 1-466.
- Fouquet, Y., 1997, Where are the large hydrothermal sulphide deposits in the oceans?: *Philosophical Transactions of the Royal Society of London. Series A: Mathematical, Physical and Engineering Sciences*, v. 355, no. 1723, p. 427-441.
- Geiger, S., Driesner, T., Heinrich, C., and Matthäi, S., 2006, Multiphase Thermohaline Convection in the Earth's Crust: I. A New Finite Element – Finite Volume Solution Technique Combined With a New Equation of State for NaCl–H₂O: *Transport in Porous Media*, v. 63, no. 3, p. 399-434.
- Geiger, S., Driesner, T., Heinrich, C. A., and Matthai, S. K., 2005, On the dynamics of NaCl-H₂O fluid convection in the Earth's crust: *Journal of Geophysical Research-Solid Earth*, v. 110, no. B7.
- Geiger, S., Robert, S., Matthai, S. K., Zoppou, C., and Burri, A., 2004, Combining finite element and finite volume methods for efficient multiphase flow simulations in highly heterogeneous and structurally complex geologic media: *Geofluids*, v. 4, no. 4, p. 284-299.
- German, C. R., Baker, E. T., Mevel, C., Tamaki, K., and the, F. S. T., 1998, Hydrothermal activity along the southwest Indian ridge: *Nature*, v. 395, no. 6701, p. 490-493.
- German, C. R., and Lin, J., 2004, The Thermal Structure of the Oceanic Crust, Ridge-Spreading and Hydrothermal Circulation: How Well Do We Understand Their Inter-Connections?, *Mid-Ocean Ridges: Hydrothermal Interactions Between the Lithosphere and Oceans*, Volume Geophysical Monograph 148, AGU.

- German, C. R., and Seyfried Jr, W. E., 2014, Hydrothermal Processes, *in* Turekian, H. D. H. K., ed., *Treatise on Geochemistry (Second Edition), Volume 8*: Oxford, Elsevier, p. 191-233.
- Gerya, T., 2010, *Introduction to Numerical Geodynamic Modelling*, New York, Cambridge University Press.
- Gomez Barreiro, J., Martinez Catalan, J. R., Prior, D., Wenk, H.-R., Vogel, S., Diaz Garcia, F., Arenas, R., Sanchez Martinez, S., and Lonardelli, I., 2010, Fabric Development in a Middle Devonian Intraoceanic Subduction Regime: The Careo' n Ophiolite (Northwest Spain): *The Journal of Geology*, v. 118, no. 163-186.
- Grassle, J. F., 1985, Hydrothermal Vent Animals: Distribution and Biology: *Science*, v. 229, no. 4715, p. 713-717.
- Grevemeyer, I., Reston, T. J., and Moeller, S., 2013, Micro-seismicity of the Mid-Atlantic Ridge at 7°S to 8°15'S and at the Logatchev Massif oceanic core complex at 14°40'N to 14°50'N: *Geochemistry, Geophysics, Geosystems*.
- Gueydan, F., Précigout, J., and Montési, L. G. J., 2014, Strain weakening enables continental plate tectonics: *Tectonophysics*, v. 631, no. 0, p. 189-196.
- Haase, K. M., Petersen, S., Koschinsky, A., Seifert, R., Devey, C. W., Keir, R., Lackschewitz, K. S., Melchert, B., Perner, M., Schmale, O., Süling, J., Dubilier, N., Zielinski, F., Fretzdorff, S., Garbe-Schönberg, D., Westernströer, U., German, C. R., Shank, T. M., Yoerger, D., Giere, O., Kuever, J., Marbler, H., Mawick, J., Mertens, C., Stöber, U., Walter, M., Ostertag-Henning, C., Paulick, H., Peters, M., Strauss, H., Sander, S., Stecher, J., Warmuth, M., and Weber, S., 2007, Young volcanism and related hydrothermal activity at 5°S on the slow-spreading southern Mid-Atlantic Ridge: *Geochemistry Geophysics Geosystems*, v. 8, no. 11, p. Q11002.
- Hamza, V. M., Cardoso, R. R., and Neto, C. F. P., 2008, Spherical harmonic analysis of earth's conductive heat flow: *International Journal of Earth Sciences*, v. 97, no. 2, p. 205-226.
- Hannington, M., Jamieson, J., Monecke, T., Petersen, S., and Beaulieu, S., 2011, The abundance of seafloor massive sulfide deposits: *Geology*, v. 39, no. 12, p. 1155-1158.
- Hannington, M. D., 2013, The role of black smokers in the Cu mass balance of the oceanic crust: *Earth and Planetary Science Letters*, v. 374, p. 215-226.
- , 2014, Volcanogenic Massive Sulfide Deposits, *in* Turekian, H. D. H. K., ed., *Treatise on Geochemistry (Second Edition), Volume 13*: Oxford, Elsevier, p. 463-488.
- Hannington, M. D., De Ronde, C. E. J., and Petersen, S., 2005, Sea-Floor Tectonics and Submarine Hydrothermal Systems, *in* Hedenquist, J. W., Thompson, J. F. H., Goldfarb, R. J., and Richards, J. P., eds., *Economic Geology: One Hundredth Anniversary Volume, Volume 1*: Littleton, Colorado, Economic Geology, p. 111-141.
- Hannington, M. D., Jonasson, I. R., Herzig, P. M., and Petersen, S., 1995, Physical and Chemical Processes of Seafloor Mineralization at Mid-Ocean Ridges, *in* Humphris, S. E., Zierenberg, R. A., Mullineaux, L. S., and Thomson, R. E., eds., *Seafloor Hydrothermal Systems - Physical, chemical, biological and geological interactions, Volume 91*: Washington DC, American Geophysical Union, p. 1-466.
- Hasenclever, J., Theissen-Krah, S., Rupke, L. H., Morgan, J. P., Iyer, K., Petersen, S., and Devey, C. W., 2014, Hybrid shallow on-axis and deep off-axis hydrothermal circulation at fast-spreading ridges: *Nature*, v. 508, no. 7497, p. 508-512.
- Herzig, P. M., 1999, Economic potential of sea-floor massive sulphide deposits: ancient and modern: *Philosophical Transactions of the Royal Society a-Mathematical Physical and Engineering Sciences*, v. 357, no. 1753, p. 861-873.

- Hess, H., 1962, History of ocean basins, *in* Engel, A. E. J., James, L. J., and Leonard, B. F., eds., Volume Petrologic studies: a volume in honor of A. F. Buddington: Boulder, Geological Society of America.
- Huber, R., and Helmig, R., 1999, Multiphase flow in heterogeneous porous media: A classical finite element method versus an implicit pressure explicit saturation-based mixed finite element finite volume approach: *International Journal for Numerical Methods in Fluids*, v. 29, no. 8, p. 899-920.
- Hughes, T. J. R., 2000, *The Finite Element Method: Linear Static and Dynamic Finite Element Analysis*, Dover Publications, Dover Civil and Mechanical Engineering.
- Humphris, S. E., Tivey, M. K., and Tivey, M. A., 2015, The Trans-Atlantic Geotraverse hydrothermal field: A hydrothermal system on an active detachment fault: *Deep Sea Research Part II: Topical Studies in Oceanography*, no. Topical Studies in Oceanography.
- Hutnak, M., Fisher, A. T., Harris, R., Stein, C., Wang, K., Spinelli, G., Schindler, M., Villinger, H., and Silver, E., 2008, Large heat and fluid fluxes driven through mid-plate outcrops on ocean crust: *Nature Geoscience*, v. 1, no. 9, p. 611-614.
- Ingebritsen, S. E., Geiger, S., Hurwitz, S., and Driesner, T., 2010, Numerical simulation of magmatic hydrothermal systems: *Reviews of Geophysics*, v. 47.
- Ismail-Zadeh, A., and Tackley, P. J., 2010, *Computational Methods for Geodynamics*, Cambridge, Cambridge University Press.
- Ito, G., and Behn, M. D., 2008, Magmatic and tectonic extension at mid-ocean ridges: 2. Origin of axial morphology: *Geochemistry Geophysics Geosystems*, v. 9.
- Iyer, K., Rüpke, L. H., and Morgan, J. P., 2010, Feedbacks between mantle hydration and hydrothermal convection at ocean spreading centers: *Earth and Planetary Science Letters*, v. 296, no. 1-2, p. 34-44.
- Jaeger, J. C., Cook, N. G. W., and Zimmerman, R. W., 2007, *Fundamentals of rock mechanics*, Blackwell Publishing, 475 p.:
- James, R. H., Elderfield, H., and Palmer, M. R., 1995, The chemistry of hydrothermal fluids from the Broken Spur site, 29°N Mid-Atlantic ridge: *Geochimica et Cosmochimica Acta*, v. 59, no. 4, p. 651-659.
- Jamieson, J. W., Clague, D. A., and Hannington, M. D., 2014, Hydrothermal sulfide accumulation along the Endeavour Segment, Juan de Fuca Ridge: *Earth and Planetary Science Letters*, v. 395, p. 136-148.
- Johnson, H. P., Tivey, M. A., Bjorklund, T. A., and Salmi, M. S., 2010, Hydrothermal circulation within the Endeavour Segment, Juan de Fuca Ridge: *Geochemistry Geophysics Geosystems*, v. 11, no. 5, p. Q05002.
- Jupp, T., and Schultz, A., 2000, A thermodynamic explanation for black smoker temperatures: *Nature*, v. 403, no. 6772, p. 880-883.
- Jupp, T. E., and Schultz, A., 2004, Physical balances in subseafloor hydrothermal convection cells: *Journal of Geophysical Research-Solid Earth*, v. 109, no. B5.
- Karson, J. A., and Brown, J. R., 1988, Geologic setting of the Snake Pit hydrothermal site: An active vent field on the Mid-Atlantic Ridge: *Marine Geophysical Researches*, v. 10, no. 1-2, p. 91-107.
- Kaus, B. J. P., 2010, Factors that control the angle of shear bands in geodynamic numerical models of brittle deformation: *Tectonophysics*, v. 484, no. 1-4, p. 36-47.
- Kelley, D. S., Delaney, J. R., and Yoerger, D. R., 2001, Geology and venting characteristics of the Mothra hydrothermal field, Endeavour segment, Juan de Fuca Ridge: *Geology*, v. 29, no. 10, p. 959-962.

- Kohlstedt, D. L., Evans, B., and Mackwell, S. J., 1995, Strength of the lithosphere - constraints imposed by laboratory experiments: *Journal of Geophysical Research-Solid Earth*, v. 100, no. B9, p. 17587-17602.
- Koschinsky, A., Garbe-Schonberg, D., Sander, S., Schmidt, K., Gennerich, H. H., and Strauss, H., 2008, Hydrothermal venting at pressure-temperature conditions above the critical point of seawater, 5 degrees S on the Mid-Atlantic Ridge: *Geology*, v. 36, no. 8, p. 615-618.
- Kuehn, M., 2004, *Reactive Flow Modeling of Hydrothermal Systems*, Berlin Heidelberg, Springer-Verlag, 261 p.
- Langmuir, C., Humphris, S., Fornari, D., Van Dover, C., Von Damm, K., Tivey, M. K., Colodner, D., Charlou, J. L., Desonie, D., Wilson, C., Fouquet, Y., Klinkhammer, G., and Bougault, H., 1997, Hydrothermal vents near a mantle hot spot: the Lucky Strike vent field at 37°N on the Mid-Atlantic Ridge: *Earth and Planetary Science Letters*, v. 148, no. 1-2, p. 69-91.
- Larson, R. L., and Spiess, F. N., 1968, East Pacific Rise Crest: A Near-Bottom Geophysical Profile: *Science*, v. 163, no. 68-71.
- Lewis, K. C., and Lowell, R. P., 2009, Numerical modeling of two-phase flow in the NaCl-H₂O system: 2. Examples: *Journal of Geophysical Research-Solid Earth*, v. 114, p. 16.
- Lister, C. R. B., 1972, On the thermal balance of a Mid-ocean ridge: *Geophysical Journal of the Royal Astronomical Society*, v. 26, no. 5, p. 515-&.
- Lowell, R. P., 1991, Modeling continental and submarine hydrothermal systems: *Reviews of Geophysics*, v. 29, no. 3, p. 457-476.
- Lowell, R. P., Rona, P. A., and Vonherzen, R. P., 1995, Sea-floor hydrothermal systems: *Journal of Geophysical Research-Solid Earth*, v. 100, no. B1, p. 327-352.
- Lowell, R. P., and Yao, Y., 2002, Anhydrite precipitation and the extent of hydrothermal recharge zones at ocean ridge crests: *Journal of Geophysical Research: Solid Earth*, v. 107, no. B9, p. 2183.
- Lupton, J. E., Weiss, R. F., and Craig, H., 1977, Mantle Helium in hydrothermal plumes in Galapagos Rift: *Nature*, v. 267, no. 5612, p. 603-604.
- Macdonald, K. C., 1982, Mid-Ocean Ridges - fine scale tectonic, volcanic and hydrothermal processes within the plate boundary zone: *Annual Review of Earth and Planetary Sciences*, v. 10, p. 155-190.
- Macdonald, K. C., 1998, Linkages Between Faulting, Volcanism, Hydrothermal Activity and Segmentation on Fast Spreading Centers, Faulting and Magmatism at Mid-Ocean Ridges, *American Geophysical Union*, p. 27-58.
- Macdonald, K. C., 2001, Mid-Ocean Ridge Tectonics, Volcanism, and Geomorphology, *Encyclopedia of Ocean Sciences*, p. 852-866.
- Macdonald, K. C., Becker, K., Spiess, F. N., and Ballard, R. D., 1980, Hydrothermal heat flux of the "black smoker" vents on the East Pacific Rise: *Earth and Planetary Science Letters*, v. 48, no. 1, p. 1-7.
- MacLeod, C. J., Searle, R. C., Murton, B. J., Casey, J. F., Mallows, C., Unsworth, S. C., Achenbach, K. L., and Harris, M., 2009, Life cycle of oceanic core complexes: *Earth and Planetary Science Letters*, v. 287, no. 3-4, p. 333-344.
- Magyari, E., Rees, D. A. S., and Keller, B., 2005, Effect of viscous dissipation on the flow in fluid saturated porous media, *in* Vafai, K., ed., *Handbook of porous media*: Boca Raton, Taylor & Francis Group, p. 374-406.
- Martin, W., Baross, J., Kelley, D., and Russell, M., 2008, Hydrothermal vents and the origin of life: *Nat Rev Micro*, v. 6, no. 11, p. 805-814.

- McCaig, A. M., Cliff, R. A., Escartin, J., Fallick, A. E., and MacLeod, C. J., 2007, Oceanic detachment faults focus very large volumes of black smoker fluids: *Geology*, v. 35, no. 10, p. 935-938.
- McCaig, A. M., and Harris, M., 2012, Hydrothermal circulation and the dike-gabbro transition in the detachment mode of slow seafloor spreading: *Geology*, v. 40, no. 4, p. 367-370.
- Menard, H. W., 1967, Sea Floor Spreading, Topography, and the Second Layer: *Science*, v. 157, no. 3791, p. 923-924.
- Morgan, J. P., and Chen, Y. J., 1993a, Dependence of ridge-axis morphology on magma supply and spreading rate: *Nature*, v. 364, no. 6439, p. 706-708.
- Morgan, J. P., and Chen, Y. J., 1993b, The Genesis of Oceanic Crust: Magma Injection, Hydrothermal Circulation, and Crustal Flow: *J. Geophys. Res.*, v. 98, no. B4, p. 6283-6297.
- Olive, J.-A., Behn, M. D., and Tucholke, B. E., 2010, The structure of oceanic core complexes controlled by the depth distribution of magma emplacement: *Nature Geosci.*, v. 3, no. 7, p. 491-495.
- Ondréas, H., Cannat, M., Fouquet, Y., Normand, A., Sarradin, P. M., and Sarrazin, J., 2009, Recent volcanic events and the distribution of hydrothermal venting at the Lucky Strike hydrothermal field, Mid-Atlantic Ridge: *Geochemistry, Geophysics, Geosystems*, v. 10, no. 2, p. n/a-n/a.
- Perfit, M. R., and Chadwick, W. W., 1998, Magmatism at Mid-Ocean Ridges: Constraints from Volcanological and Geochemical Investigations, *Faulting and Magmatism at Mid-Ocean Ridges*, American Geophysical Union, p. 59-115.
- Petersen, S., Kuhn, K., Kuhn, T., Augustin, N., Hekinian, R., Franz, L., and Borowski, C., 2009, The geological setting of the ultramafic-hosted Logatchev hydrothermal field (14 degrees 45 ' N, Mid-Atlantic Ridge) and its influence on massive sulfide formation: *Lithos*, v. 112, no. 1-2, p. 40-56.
- Pettersson, H., 1948, The Swedish Deep-Sea Expedition: *Pacific Science*, v. 2, p. 231-238.
- Phipps Morgan, J., and Chen, Y. J., 1993, The genesis of oceanic crust: magma injection, hydrothermal circulation, and crustal flow: *J. Geophys. Res.*, v. 98, p. 6283-6297.
- Pirajno, F., 1992, *Hydrothermal Mineral Deposits - Principles and fundamental concepts for the exploration geologist*, Berlin Heidelberg, Springer-Verlag.
- Pollack, H. N., and Chapman, D. S., 2008, Comment on "Spherical harmonic analysis of earth's conductive heat flow" by V. M. Hamza, R. R. Cardoso and C. F. Ponte Neto: *International Journal of Earth Sciences*, v. 97, no. 2, p. 227-231.
- Quick, J. E., and Denlinger, R. P., 1993, Ductile deformation and the origin of layered gabbro in ophiolites: *J. Geophys. Res.*, v. 98, p. 14015-14027.
- Ranalli, G., 1995, *Rheology of the earth*, Chapman & Hall, 413 p.:
- Rona, P. A., 1978, Near bottom water temperature anomalies: Mid-Atlantic Ridge crest at latitude 26°N: *Geophysical Research Letters*, v. 5, no. 12, p. 993-996.
- , 2008, The changing vision of marine minerals: *Ore Geology Reviews*, v. 33, no. 3-4, p. 618-666.
- Rona, P. A., McGregor, B. A., Betzer, P. R., Bolger, G. W., and Krause, D. C., 1975, Anomalous water temperatures over Mid-Atlantic Ridge crest at 26° North latitude: *Deep Sea Research and Oceanographic Abstracts*, v. 22, no. 9, p. 611-618.
- Ryan, W. B. F., Carbotte, S. M., Coplan, J. O., O'Hara, S., Melkonian, A., Arko, R., Weissel, R. A., Ferrini, V., Goodwillie, A., Nitsche, F., Bonczkowski, J., and Zemsky, R., 2009, Global Multi-Resolution Topography synthesis: *Geochemistry, Geophysics, Geosystems*, v. 10, no. 3, p.

- Schardt, C., and Large, R. R., 2009, New insights into the genesis of volcanic-hosted massive sulfide deposits on the seafloor from numerical modeling studies: *Ore Geology Reviews*, v. 35, no. 3-4, p. 333-351.
- Schmidt, K., Garbe-Schönberg, D., Koschinsky, A., Strauss, H., Jost, C. L., Klevenz, V., and Königer, P., 2011, Fluid elemental and stable isotope composition of the Nibelungen hydrothermal field (8°18'S, Mid-Atlantic Ridge): Constraints on fluid-rock interaction in heterogeneous lithosphere: *Chemical Geology*, v. 280, no. 1-2, p. 1-18.
- Schmidt, K., Koschinsky, A., Garbe-Schönberg, D., de Carvalho, L. M., and Seifert, R., 2007, Geochemistry of hydrothermal fluids from the ultramafic-hosted Logatchev hydrothermal field, 15 degrees N on the Mid-Atlantic Ridge: Temporal and spatial investigation: *Chemical Geology*, v. 242, no. 1-2, p. 1-21.
- Slater, J. G., Anderson, R. N., and Lee Bell, M., 1971, Elavation of Ridges and Evolution of the Central Eastern Pacific: *Journal of Geophysical Research*, v. 76, no. 32, p. 7888-7915.
- Seyfried, W. E., and Bischoff, J. L., 1981, Experimental seawater-basalt interaction at 300°C, 500 bars, chemical exchange, secondary mineral formation and implications for the transport of heavy metals: *Geochimica et Cosmochimica Acta*, v. 45, no. 2, p. 135-147.
- Shilov, V. V., Bel'tenev, V. E., Ivanov, V. N., Cherkashev, G. A., Rozhdestvenskaya, I. I., Gablina, I. F., Dobretsova, I. G., Narkevskii, E. V., Gustaitis, A. N., and Kuznetsov, V. Y., 2012, New hydrothermal ore fields in the Mid-Atlantic Ridge: Zenith-Victoria (20° 08' N) and Petersburg (19° 52' N): *Doklady Earth Sciences*, v. 442, no. 1, p. 63-69.
- Sigurdsson, H., and Houghton, B. F., 2000, *Encyclopedia of Volcanoes*, Academic Press.
- Singh, S. C., Crawford, W. C., Carton, H., Seher, T., Combier, V., Cannat, M., Pablo Canales, J., Dusunur, D., Escartin, J., and Miguel Miranda, J., 2006, Discovery of a magma chamber and faults beneath a Mid-Atlantic Ridge hydrothermal field: *Nature*, v. 442, no. 7106, p. 1029-1032.
- Sinha, M. C., and Evans, R. L., 2004, Gephysical constraints upon the thermal regime of the ocean crust, *Mid-Ocean Ridges: Hydrothermal Interactions Between the Lithosphere and Oceans*, Volume 148: Washington, DC, AGU, p. 19-62.
- Sinha, M. C., Evans, R. L., German, C., Lin, J., and Parson, L., 2004, *Mid-Ocean Ridges: Hydrothermal Interactions Between the Lithosphere and Oceans*, p. 19-62.
- Sinton, J. M., and Detrick, R. S., 1992, Mid-ocean ridge magma chambers: *Journal of Geophysical Research: Solid Earth*, v. 97, no. B1, p. 197-216.
- Sleep, N. H., 1975, Formation of oceanic crust: Some thermal constraints: *Journal of Geophysical Research*, v. 80, no. 29, p. 4037-4042.
- Small, C., 1998, *Global Systematics of Mid-Ocean Ridge Morphology, Faulting and Magmatism at Mid-Ocean Ridges*, American Geophysical Union, p. 1-25.
- Spiess, F. N., Macdonald, K. C., Atwater, T., Ballard, R., Carranza, A., Cordoba, D., Cox, C., Diazgarcia, V. M., Francheteau, J., Guerrero, J., Hawkins, J., Haymon, R., Hessler, R., Juteau, T., Kastner, M., Larson, R., Luyendyk, B., Macdougall, J. D., Miller, S., Normark, W., Orcutt, J., and Rangin, C., 1980, East Pacific Rise - Hot springs and geophysical experiments: *Science*, v. 207, no. 4438, p. 1421-1433.
- Talwani, M., Windisch, C. C., and Langseth Jr., M. G., 1971, Reykjanes ridge crest a detailed geophysical study: *Journal of Geophysical Research*, v. 76, no. 2, p. 473-517.
- Theissen-Krah, S., Iyer, K., Rupke, L. H., and Morgan, J. P., 2011, Coupled mechanical and hydrothermal modeling of crustal accretion at intermediate to fast spreading ridges: *Earth and Planetary Science Letters*, v. 311, no. 3-4, p. 275-286.

- Tivey, M. A., 1995, Modeling Chimney Growth and Associated Fluid Flow at Seafloor Hydrothermal Vent Sites, *Seafloor Hydrothermal Systems: Physical, Chemical, Biological, and Geological Interactions*, American Geophysical Union, p. 158-177.
- Tucholke, B. E., Behn, M. D., Buck, W. R., and Lin, J., 2008, Role of melt supply in oceanic detachment faulting and formation of megamullions: *Geology*, v. 36, no. 6, p. 455-458.
- Turcotte, D. L., and Schubert, G., 2002, *Geodynamics* New York, Cambridge University Press, 456 p.
- Van der Pluijm, B. A., and Marshak, S., 2003, *Earth Structure: An Introduction to Structural Geology and Tectonics*, Norton and Company, 672 p.:
- Vine, F. J., 1966, Spreading of the Ocean Floor: New Evidence: *Science*, v. 154, no. 3755, p. 1405-1415.
- Vine, F. J., and Matthews, D. H., 1963, Magnetic Anomalies Over Oceanic Ridges: *Nature*, v. 199, no. 4897, p. 947-949.
- Von Damm, K. L., Lilley, M. D., Shanks Iii, W. C., Brockington, M., Bray, A. M., O'Grady, K. M., Olson, E., Graham, A., and Proskurowski, G., 2003, Extraordinary phase separation and segregation in vent fluids from the southern East Pacific Rise: *Earth and Planetary Science Letters*, v. 206, no. 3-4, p. 365-378.
- Weis, P., 2015, The dynamic interplay between saline fluid flow and rock permeability in magmatic-hydrothermal systems: *Geofluids*, v. 15, no. 1-2, p. 350-371.
- Weis, P., and Driesner, T., 2013, The Interplay of Non-static Permeability and Fluid Flow as a Possible Pre-requisite for Supercritical Geothermal Resources: *Energy Procedia*, v. 40, no. 0, p. 102-106.
- Weis, P., Driesner, T., Coumou, D., and Geiger, S., 2014, Hydrothermal, Multi-phase Convection of H₂O-NaCl Fluids from Ambient to Magmatic Temperatures: A new Numerical Scheme and Benchmarks for Code Comparison: *Geofluids*, p. n/a-n/a.
- Weiss, R. F., Lonsdale, P., Lupton, J. E., Bainbridge, A. E., and Craig, H., 1977, Hydrothermal plumes in Galapagos Rift: *Nature*, v. 267, no. 5612, p. 600-603.
- Whiting, R. L., and Ramey, H. J., Jr., 1969, Application of Material and Energy Balances to Geothermal Steam Production: *Journal of Petroleum Technology*, v. 21, no. 7.
- Wilcock, W. S. D., and McNabb, A., 1996, Estimates of crustal permeability on the endeavour segment of the Juan de Fuca mid-ocean ridge: *Earth and Planetary Science Letters*, v. 138, no. 1-4, p. 83-91.
- Wooding, R. A., 1957, Steady state free thermal convection of liquid in a saturated permeable medium: *Journal of Fluid Mechanics*, v. 2, p. 273-285.
- Zienkiewicz, O. C., and Taylor, R. L., 2000, *The Finite Element Method - The Basis*, Elsevier Science, Finite Element Method Series.

Glossary, mathematical symbols and abbreviations used

Symbol	explanation	units
General		
	Kilogram	kg
	Meter or mass (in kg)	m
	Second	s
	Pascal	Pa
	Kelvin	K
	Degrees Celsius	°C
	Joule	J
t/dt	time/timestep	s
x, y	spatial coordinates	m
n	numerical timestep $n = 1, 2, 3...$	—
N	shape function-weighting function for Galerkin FEM	—
δ	weighting symbol (FE notation)	—
P	pressure	bar, Pa or $\text{kg m}^{-1}\text{s}^{-2}$
T	temperature	°C
g/a	gravitational/acceleration	m s^{-2}
Hydrothermal flow model		
ρ	density	kg m^{-3}
cp	specific heat capacity	J (kg K)^{-1}
μ	viscosity	Pa s^{-1} or kg (m s)^{-1}
α	thermal expansivity	$^{\circ}\text{C}^{-1}$
β	compressibility	Pa^{-1}

Symbol	explanation	units
h	specific fluid enthalpy	J kg^{-1}
J	thermal energy ($\rho^*c_p^*T$)	$\text{kg m}^2 \text{s}^{-2}$
κ	thermal conductivity	W (m K)^{-1}
K_{diff}	thermal diffusivity	$\text{m}^2 \text{s}^{-1}$
k	permeability	m^2
c	permeability contrast	—
φ	porosity	%
v	darcy velocity	m s^{-1}
u	pore velocity of fluid inside the pores (v/φ)	m s^{-1}
q_{mass}	mass flux (ρ^*u)	$\text{kg s}^{-1}\text{m}^{-2}$
m_f	integrated fluid mass flux	$\text{kg (s m}^{-1}\text{)}$
q_{heat}	conductive heat flux	W m^{-2}
H_f	integrated heat flux into model domain (LHF1)	kW/m ridge axis
Q_{in}	total magmatic heat input	W/m

Mechanical model

f	force	kg m s^{-2}
A	area	m^2
σ	stress (force per unit area)	$\text{kg m}^{-1}\text{s}^{-2}$
σ_n	normal stress — acting perpendicular to a given plane	
τ	shear stress — acting parallel to a given plane	
σ'	deviatoric stress — stress component after removal of the mean stress/pressure	
σ_{II}	2nd invariant of stress	

Symbol	explanation	units
ε	strain—measure of deformation (by distortion or dilation)	—
$\dot{\varepsilon}$	strain rate	s^{-1}
$\dot{\varepsilon}'$	deviatoric strain rate (after subtraction of normal strain rates)	s^{-1}
ε_{II}	2nd invariant of strain	s^{-1}
G	elastic shear modulus (rigidity)	Pa
η	viscosity	$kg (m s)^{-1}$ or $Pa s^{-1}$
μ_{vep}	effective visco-elasto-plastic viscosity	$kg (m s)^{-1}$ or $Pa s^{-1}$
ψ	dilation angle	$^{\circ}$
φ	friction angle	$^{\circ}$
c	cohesion	Pa
Q	plastic flow potential	
F	yield function	
ψ	dilation term	$kg m^{-1}s^{-2}$
λ	penalty factor (for incompressibility)	—
e_p	error during plasticity iterations	—
γ_{pl}	plastic multiplier	—

Abbreviations

MOR	Mid Ocean Ridge
MAR	Mid Atlantic Ridge
EPR	East Pacific Rise
FD/FV	Finite Differences/Finite Volumes
FEM	Finite Element Method
SMS	Submarine Massive Sulphides
EOS	Equation Of State (of water)
R/LHS	Right/Left hand side (of an equation)

Curriculum Vitae

Christine Sophie Andersen

born 16.09.1984 in Kiel

Nationality german

since 2011 Scientist at GEOMAR, Kiel

2009-2010 M.Sc. (Geoscience), Lund University, Sweden/
GEOMAR, Helmholtz Centre for Ocean Research Kiel

2008 University of Auckland, New Zealand: Exchange
Scholarship (Geosciences, Numerical Modelling)

2005-2007 B.Sc. Geosciences (Major) & Mathematics (Minor),
Lund University, Sweden

2004 Abitur at Freie Waldorfschule Kiel, Germany